AD_____

Award Number: W81XWH-05-1-0617

TITLE: Closed-loop Noninvasive Ultrasound Glucose Sensing and Insulin Delivery

PRINCIPAL INVESTIGATOR: Nadine Smith, Ph.D.
Michael Pishko, Ph.D.
Robert Gabbay, M.D., Ph.D.
Jacob Werner, D.V.M.

CONTRACTING ORGANIZATION: Pennsylvania State University
University Park, PA 16802

REPORT DATE: September 2006

TYPE OF REPORT: Annual

PREPARED FOR: U.S. Army Medical Research and Materiel Command
Fort Detrick, Maryland 21702-5012

REPORT DOCUMENTATION PAGE

Form Approved
OMB No. 0704-0188

1. REPORT DATE	2. REPORT TYPE	3. DATES COVERED
01-09-2006	Annual	19 Sep 2005 – 18 Sep 2006

4. TITLE AND SUBTITLE

Closed-loop Noninvasive Ultrasound Glucose Sensing and Insulin Delivery

5a. CONTRACT NUMBER

5b. GRANT NUMBER
W81XWH-05-1-0617

5c. PROGRAM ELEMENT NUMBER

6. AUTHOR(S)
Nadine Smith, Ph.D.
Michael Pishko, Ph.D.
Robert Gabbay, M.D., Ph.D.
Jacob Werner, D.V.M.

5d. PROJECT NUMBER

5e. TASK NUMBER

5f. WORK UNIT NUMBER

7. PERFORMING ORGANIZATION NAME(S) AND ADDRESS(ES)

Pennsylvania State University
University Park, PA 16802

8. PERFORMING ORGANIZATION REPORT NUMBER

9. SPONSORING / MONITORING AGENCY NAME(S) AND ADDRESS(ES)
U.S. Army Medical Research and Materiel Command
Fort Detrick, Maryland 21702-5012

10. SPONSOR/MONITOR'S ACRONYM(S)

11. SPONSOR/MONITOR'S REPORT NUMBER(S)

12. DISTRIBUTION / AVAILABILITY STATEMENT
Approved for Public Release; Distribution Unlimited

13. SUPPLEMENTARY NOTES
Original contains colored plates: ALL DTIC reproductions will be in black and white.

14. ABSTRACT

Numerous studies have shown that ultrasound can successfully be used for noninvasive blood glucose monitoring and transdermal insulin delivery. To facilitate the ability of a diabetic patient to avoid repeated needle sticks to monitor blood glucose level and painful daily injections of insulin, this basic research proposal will study the feasibility of safe and portable ultrasonic system to do both. Specifically using the low profile and light weight "cymbal" transducer, a potentially portable ultrasound array of will be designed. Moreover the feasibility of a "smart" diabetes management system will be developed to control both the glucose monitoring and insulin delivery system. The report herein describes the year one progress for this award and there are no deviations from the original research plan and this research is progressing on schedule.

15. SUBJECT TERMS
ultrasound, transdermal, diabetes, insulin, glucose, noninvasive

16. SECURITY CLASSIFICATION OF:				18. NUMBER OF PAGES	19a. NAME OF RESPONSIBLE PERSON
					USAMRMC
a. REPORT	b. ABSTRACT	c. THIS PAGE			19b. TELEPHONE NUMBER *(include area code)*
U	U	U	UU	230	

Table of Contents

I. INTRODUCTION

Recent studies have shown that ultrasound mediated transdermal insulin delivery offers promising potential for noninvasive drug administration [1-4] . Additionally, the transdermal extraction of interstitial fluid by low-frequency ultrasound offers a potential minimally invasive method of obtaining a fluid sample for at-home blood glucose monitoring [5]. However, researchers who have successfully used acoustic energy for glucose monitoring and insulin delivery have used commercial sonicators or commercially constructed transducers. These large industrial devices are impractical for a compact and transportable diabetes management device. The goal of this research is to develop a practicable ultrasound device to noninvasively determine blood glucose levels and transport insulin across the skin. To accomplish this task, this research will explore the use of novel, low profile and light weight transducers. This developmental technology research proposal will study the feasibility of a safe and portable ultrasonic system to allow diabetic patients to avoid the repeated needle sticks traditionally used to monitor blood glucose level and painful daily injections of insulin. With a built-in real-time electronic feedback loop (i.e. "smart") between the glucose monitoring and insulin delivery functions, control of blood sugar can be made automatic and continuous. Specifically, using the low profile and light weight "cymbal" transducers [6-9], a potentially portable ultrasound array will be designed. Moreover, a "smart" diabetes management system will be developed to control the glucose monitoring and insulin delivery system.

II. BODY

The long-term goal of this research is to develop a practicable (i.e. safe, portable, low-cost, efficient) ultrasound device to noninvasively transport insulin across the skin. To accomplish this task, this research will explore the use of novel, low profile transducers for drug delivery in addition to determining the optimal frequency and exposure conditions. Based on initial prototype designs, acoustic field characteristics of the transducers and arrays will be further optimized based on experimental results and complementary simulations. Once several prototypes are constructed, the acoustic field will be evaluated using exposimetry and dosimetry techniques along with quantifying cavitation events and thermal effects. The efficacy for transdermal delivery will be accessed by determining the permeability of insulin with *in vitro* skin. *In vivo* evaluation of the ultrasound devices will test insulin delivery using a diabetic animal model by monitoring the blood glucose levels with the cymbal. Mechanism for enhanced permeability due to ultrasound will be determined also be studied. Damage to the *in vitro / in vivo* skin along with underlying tissue from the ultrasound will be evaluated from histological microscopy studies. Using a cymbal glucose sensor system, the feasibility of controlled insulin delivery will be tested. Summarizing from the original grant application, the overall specific tasks for this project are:

Task 1. Ergonomic cymbal transducer design for glucose monitoring and insulin delivery (Mo. 1-12)
Task 2. Accurate characterization of the acoustic field (Months 1-24)
Task 3. Closed-loop, feedback controlled for a "synthetic pancreas" (Months 1-12)
Task 4. In vivo evaluation using a diabetic pig models (Months 12-24)
Task 5. Dissemination of Results (Months 6-24)

For the first year, plus or minus a few months, our group focused on Tasks 1, 2, 3 and 5. Since this report allows "that publications and/or presentations may be substituted for detailed descriptions of methodology but must be referenced in the body of the report" we would like to utilize the appendix for details and summarize the accomplishments of the tasks in the following subsections.

IIa. Task 1 Transducer design for insulin delivery and Task 2. Accurate characterization of the acoustic field [10;11]

The use of sonicators for transdermal drug delivery has led to the development of advanced light-weight cymbal arrays for use in a portable device. These cymbals are Class V flextensional transducers consisting of a piezoelectric disk sandwiched between two metal end caps. Arrays consisting of these transducers have proven effective in delivering therapeutic levels of insulin in rats and rabbits. To improve the system, rectangular cymbals are used in a 3x1 array. Rectangular cymbals maximize packing density, giving up to a 70% greater radiating area for a similar array size. A rectangular geometry also allows the flexural cap resonance and the ceramic length mode resonance frequencies to be designed closer in frequency. The new rectangular cymbal transducer is analyzed both theoretically and using the finite element software ATILA. The transducers were built and near field exposimetry and far field water tank measurements were taken for single element and 3x1 arrays. It is determined that bringing the cap and ceramic resonances closer together increases the transmitting power and improves the efficiency by nearly an order of magnitude. In addition, by using higher order modes excited in the

cap while operating at the first ceramic resonance frequency, the intensity spatial average at a distance of 1 mm is increased, effectively sonicating more of the skin and nearly doubling the insulin delivery rate over the period of one 90 minute rabbit experiment. It is concluded that using rectangular cymbal arrays will improve the portable insulin delivery system by decreasing the total power consumed as well as increasing the insulin delivery rate. This research was performed by a Graduate Student (Mr. J Luis) under the guidance and in the laboratory of the Principal Investigator (Dr. NB Smith) of this research. The methodology and other details of these results are in:

Appendix I: Luis J. "Rectangular cymbal arrays for ultrasonic transdermal insulin delivery", 2005. Masters of Science Thesis in the Acoustics Program, The Pennsylvania State University.

Appendix II: Luis J, Smith NB, Meyer RJ. "Rectangular cymbal arrays for ultrasonic transdermal insulin delivery. Journal of the Acoustical Society of America" (submitted) 2006;

IIb. Task 3. Closed-loop, feedback controlled[12]

For controlled feedback of insulin delivery and glucose sensing this research takes advantage of the fact that dermal interstitial fluid glucose concentration is highly correlated with the plasma glucose concentration. Thus, transdermal extraction of interstitial fluid offers a noninvasive method of obtaining a sample for blood glucose measurement. Combining the above two systems into a “smart” feedback control system using a controller will provide a continuous glucose measurement and insulin delivery system, to prevent hypoglycemia and hyperglycemia states in a diabetic person. Recent studies have shown that a low profile two by two ultrasound array based on the cymbal transducer when integrated with a π-type impedance matching network produces ultrasound at 20 kHz of 100 mW/cm2 intensity that can be used to conduct experiments to demonstrate ultrasound mediated noninvasive transdermal insulin delivery in hyperglycemic rabbits. Experiments conducted by previous researchers using the cymbal array have demonstrated that the blood glucose level decreased by 208.1± 29 mg/dL for 60 minutes of ultrasound exposure of 100 mW/cm^2 and of duty cycle 20% in hyperglycemic rabbits. For this research, enzyme based glucose biosensors were used with the cymbal array to enhance skin permeability and conduct continuous glucose monitoring. Hyperglycemic rats were exposed to ultrasound for 60 minutes and the glucose sensor was placed on the exposed skin and current was measured using a potentiostat. The concentration of the glucose was measured using a calibration curve and compared with the reading obtained using an ACCU-CHEK™ blood glucose monitoring system to check for consistency. Finally the feedback controller to integrate the insulin delivery and glucose monitoring system was developed based on the proportional integral derivative (PID) algorithm. The simulation model controls the glucose concentration level within the desired level of 70-170 mg/dL with an error of ± 5%. Again, this research was performed by a Graduate Student (Mr. V. Nayak) under the direct guidance and in the laboratory of the Principal Investigator (Dr. NB Smith) of this research. The methodology and other details of these results are in:

Appendix III: Nayak V. A "smart" noninvasive ultrasound glucose monitoring and insulin delivery system. 2005. Masters of Science Thesis in the Department of Electrical Engineering, The Pennsylvania State University,

IIc. Task 5. Dissemination of results (Months 6-24)

From this research we have submitted the following two manuscripts for peer-reviewed publication.

Appendix II: Luis J, Smith NB, Meyer RJ. "Rectangular cymbal arrays for ultrasonic transdermal insulin delivery. Journal of the Acoustical Society of America" (submitted) 2006;

Appendix IV: Smith NB. Perspectives on Transdermal Ultrasound Mediated Drug Delivery. International Journal of Nanomedicine (invited submission) 2006;

III. KEY RESEARCH ACCOMPLISHMENTS:

- Using ATILA® transducer computation software, considering biological compatible materials (e.g. waterproof silicones, soft epoxies) design a flexible cymbal array system for human use.
- Animal trials of cymbal design with improved rectangular array
- Biosafety (dosimetry and exposimetry) evaluation of the ultrasound devices according to Food and Drug Administration ultrasound intensity guidelines.
- Determined spatial intensity versus insulin delivery dose relationship.
- Computer simulations of feedback system using Simulink® in MATLAB® and freeware diabetes educational simulator (www.2aida.org) program.
- Comprehensive review of transdermal drug delivery literature through International Journal of Nanomedicine invited submission. Strong critique of previous literature due to the improper exposimetry (ultrasound safety) methods.

IV. REPORTABLE OUTCOMES

Appendix II: Luis J, Smith NB, Meyer RJ. "Rectangular cymbal arrays for ultrasonic transdermal insulin delivery. Journal of the Acoustical Society of America" (submitted) 2006;

Appendix IV: Smith NB. Perspectives on Transdermal Ultrasound Mediated Drug Delivery. International Journal of Nanomedicine (invited submission) 2006;

Table 1. Student research supported by this award

Student Name	Department	Obtained
Vivekanand Nayak	Electrical Engineering	MS, 2005
Joseph Luis	Acoustics	MS, 2005
EJ Park	Bioengineering	PhD 2007 (pending, comprehensive exam passed)

V. CONCLUSION

This developmental technology research will lead to a safe and portable noninvasive ultrasonic system to allow diabetic patients to avoid the repeated needle sticks traditionally used to monitor blood glucose level and painful daily injections of insulin. With a built-in real-time electronic feedback loop (i.e. "smart") between the glucose monitoring and insulin delivery functions, control of blood sugar can be made automatic and continuous (this work in progress). Already we have demonstrated that a larger spatial acoustic field is proportional to a larger delivered dose (or faster decrease in blood glucose) using the improved rectangular cymbals over the circular cymbals. Our future goal would be to develop a mathematical relationship between intensity (spatial average, temporal average) and delivered dose. Overall, using the low profile and light weight "cymbal" transducers [7-9], a portable ultrasound array will be is under construction. Moreover, a "smart" diabetes management system will be developed to control the glucose monitoring and insulin delivery system and possible lead the way to the dream of an "artificial pancreas".

VI. REFERENCES

[1] K. Tachibana, "Transdermal delivery of insulin to alloxan-diabetic rabbits by ultrasound exposure," Pharm. Res., vol. 9, no. 7, pp. 952-954, July1992.

[2] S. Mitragotri, D. Blankschtein, and R. Langer, "Ultrasound-mediated transdermal protein delivery," Science, vol. 269, no. 5225, pp. 850-853, 1995.

[3] I. Zhang, K. K. Shung, and D. A. Edwards, "Hydrogels with enhanced mass transfer for transdermal drug delivery," J. Pharm. Sci., vol. 85, no. 12, pp. 1312-1316, Dec.1996.

[4] A. Boucaud, M. A. Garrigue, L. Machet, L. Vaillant, and F. Patat, "Effect of sonication parameters on transdermal delivery of insulin to hairless rats," J Control Release, vol. 81, no. 1-2, pp. 113-119, May2002.

[5] J. Kost, S. Mitragotri, R. A. Gabbay, M. Pishko, and R. Langer, "Transdermal monitoring of glucose and other analytes using ultrasound," Nat. Med., vol. 6, no. 3, pp. 347-350, Mar.2000.

[6] R. E. Newnham, Q. C. Xu, and S. Yoshikawa, "Metal-electroactive ceramic composite actuators,"5,276,657, Jan.4, 1994.

[7] A. Dogan, K. Uchino, and R. E. Newnham, "Composite piezoelectric transducer with truncated conical endcaps "cymbal"," IEEE Trans. Ultrason. , Ferroelect. , Freq. Contr., vol. 44, no. 3, pp. 597-605, 1997.

[8] R. E. Newnham and A. Dogan, "Metal-electroactive ceramic composite transducer,"5,729,077, Mar.17, 1998.

[9] J. F. Tressler, W. Cao, K. Uchino, and R. E. Newnham, "Finite element analysis of the cymbal-type flextensional transducer," IEEE Trans. Ultrason. , Ferroelect. , Freq. Contr., vol. 45, no. 5, pp. 1363-1369, 1998.

[10] Luis J. "Rectangular cymbal arrays for ultrasonic transdermal insulin delivery", 2005. Masters of Science Thesis in the Acoustics Program, The Pennsylvania State University.

[11] Luis J, Smith NB, Meyer RJ. "Rectangular cymbal arrays for ultrasonic transdermal insulin delivery. Journal of the Acoustical Society of America" (submitted) 2006;
[12] V Nayak V. A "smart" noninvasive ultrasound glucose monitoring and insulin delivery system. 2005. Masters of Science Thesis in the Department of Electrical Engineering, The Pennsylvania State University,

VII. APPENDICES

Appendix I: Luis J. "Rectangular cymbal arrays for ultrasonic transdermal insulin delivery", 2005. Masters of Science Thesis in the Acoustics Program, The Pennsylvania State University.

Appendix II: Luis J, Smith NB, Meyer RJ. "Rectangular cymbal arrays for ultrasonic transdermal insulin delivery. Journal of the Acoustical Society of America" (submitted) 2006;

Appendix III: Nayak V. A "smart" noninvasive ultrasound glucose monitoring and insulin delivery system. 2005. Masters of Science Thesis in the Department of Electrical Engineering, The Pennsylvania State University

Appendix IV: Smith NB. Perspectives on Transdermal Ultrasound Mediated Drug Delivery. International Journal of Nanomedicine (invited submission) 2006;

The Pennsylvania State University

The Graduate School

Graduate Program in Acoustics

RECTANGULAR CYMBAL ARRAYS FOR ULTRASONIC TRANSDERMAL INSULIN DELIVERY

A Thesis in

Acoustics

by

Joseph Luis

Submitted in Partial Fulfillment
of the Requirements
for the Degree of

Master of Science

August 2005

I grant The Pennsylvania State University the nonexclusive right to use this work for the University's own purposes and to make single copies of the work available to the public on a not-for-profit basis if copies are not otherwise available.

_____

Joseph Luis

We approve the thesis of Joseph Luis.

Date of Signature

Nadine B. Smith
Associate Professor of Bioengineering and Acoustics
Thesis Adviser

Richard J. Meyer
Associate Professor of Materials Science and Engineering

Robert E. Newnham
Professor Emeritus of Materials Science and Engineering

Anthony A. Atchley
Professor of Acoustics
Head of the Graduate Program in Acoustics

The thesis of Joseph Luis was reviewed and approved* by the following:

Nadine B. Smith
Associate Professor of Bioengineering and Acoustics
Thesis Adviser

Richard J. Meyer
Associate Professor of Materials Science and Engineering

Robert E. Newnham
Professor Emeritus of Materials Science and Engineering

Anthony A. Atchley
Professor of Acoustics
Head of the Graduate Program in Acoustics

*Signatures are on file in the Graduate School.

Abstract

The use of sonicators for transdermal drug delivery has led to the development of lightweight cymbal arrays for use in a portable device. These cymbals are Class V flextensional transducers consisting of a piezoelectric disk sandwiched between two metal end caps. Arrays consisting of these transducers have proven effective in delivering therapeutic levels of insulin in rats and rabbits. To improve the system, rectangular cymbals are used in a 3x1 array. Rectangular cymbals maximize packing density, giving up to a 70% greater radiating area for a similar array size. A rectangular geometry also allows the flexural cap resonance and the ceramic length mode resonance frequencies to be designed closer in frequency. The new rectangular cymbal transducer is analyzed both theoretically and using the finite element software ATILA. The transducers were built and near field exposimetry and far field water tank measurements were taken for single element and 3x1 arrays. It is determined that bringing the cap and ceramic resonances closer together increases the transmitting power and improves the efficiency by nearly an order of magnitude. In addition, by using higher order modes excited in the cap while operating at the first ceramic resonance frequency, the intensity spatial average at a distance of 1 mm is increased, effectively sonicating more of the skin and nearly doubling the insulin delivery rate over the period of one 90 minute rabbit experiment. It is concluded that using rectangular cymbal arrays will improve the portable insulin delivery system by decreasing the total power consumed as well as increasing the insulin delivery rate.

Table of Contents

List of Figures

List of Tables

Acknowledgements

I would first like to thank my committee, Dr. Nadine Smith, Dr. Richard Meyer, and Dr. Robert Newnham. Their insight and guidance made for a rewarding project experience. I would also like to thank the Applied Research Laboratory (ARL) for funding my studies.

My thanks goes out to many people for their help in understanding various technologies along the way. Doug Markley for his help with transducer fabrication and finite element analysis, Greg Granville for his underwater far field measurement work, EJ Park for her animal experiment knowledge, and Gene Gerber for nearly every other fabrication question I had.

I would also like to acknowledge Kim Love and Shelby Fidler, two undergraduates in the lab who always asked plenty of challenging questions about their projects and gave me a valuable teaching experience.

Finally, I would like to thank my parents who have always been there for me. They have always supported me in my education and I owe my success to them. Esta sequnda tesis es para ustedes y gracias por siempre creer en mi.

Chapter 1

Introduction

In the US, an estimated 16 million people are diagnosed with diabetes [1]. Type 1 diabetics as well as almost one third of Type 2 diabetics require the use of insulin doses to regulate stable blood glucose levels. Daily injections and needle pricks are currently the method used for insulin doses and testing blood glucose levels. The use of insulin pumps and more advanced glucose sensing methods have lessened the painful experience. However, these methods remain painful and inconvenient, especially for children. For this reason it is beneficial to pursue non-invasive methods of insulin delivery and glucose monitoring.

Work at the Pennsylvania State University has led to the use of cymbal transducer arrays to create a low profile and minimal weight patch which could serve as both a glucose monitor and insulin medicator [2]. Animal tests have shown that the cymbal arrays are capable of delivering insulin to small mammals at therapeutic levels [3]. It is the goal of the researchers to develop a closed loop feedback glucose monitoring and insulin delivery system using non-invasive ultrasonic treatments. By optimizing the novel transducer design and using principles of low frequency sonophoresis, such a system can be realized.

1.1 Sonophoresis

Sonophoresis, or using ultrasound to make the skin more permeable, was first studied in the 1950's. High frequency treatments (MHz) were used as an alternative method to hydrocortisone injections for bursitis [4]. Other drugs such as methyl and ethyl nicotinate, benzyl nicotinate, mannitol, and physostigmine were also successfully transmitted through the skin via ultrasound treatments. When a frequency dependance on drug delivery was studied, it

was found that lower frequencies in the 20 to 100 kHz range were more effective at increasing stratum corneum permeability [4]. This led to the development of various studies in low frequency sonophoresis and for this reason this study will remain in the low frequency range. Mechanisms of sonophoresis remain uncertain although there are hypotheses and these will be discussed in Section 2.2

As a transdermal drug transport system, sonophoresis is a promising method. The elimination of injections and needle pricks is an obvious gain but with a complete glucose sensing and insulin delivery system, patients will no longer have to strictly monitor their own status. When compared to oral delivery methods, transdermal drug delivery is advantageous since gastrointestinal metabolism is avoided [5]. Furthermore, although other methods such as iontophoresis, electroporation, and chemical enhancers have been used, sonophoresis appears to be most promising [5].

1.2 Previous Work

1.2.1 The Cymbal Array

In order to achieve a low profile design, a flextensional transducer termed the "cymbal" was used in a 2x2 array configuration. The cymbal is a Class V flextensional transducer consisting of a lead zirconate titanate (PZT) disk sandwiched between two titanium end caps. The radial displacement of the ceramic is translated into flexing motion of the caps, producing acoustic radiation. Arrays are potted in a 2x2 or 3x3 configuration in a ployurethane with a similar characteristic acoustic impedance to water. Total thickness of the potted array is 7 mm. An analysis of the circular cymbal transducer is given in Section 2.3.3.

Although the cymbal transducer allows for a thin device, its circular geometry is not optimal if we are to obtain a minimal surface area array. In addition, the frequency of operation excites only the first flexural mode of the caps. The first radial mode of the ceramic is closer to 100 kHz, out of our frequency band of interest. It would be beneficial to have a device that minimizes non-radiating area on the array and that brings the flexural cap mode and

ceramic modes closer together to obtain a more efficient system. This efficiency will become important once the portable electronics of the system are considered.

1.2.2 Animal Testing

Various animal tests using rats and rabbits have been done to show the effectiveness of the 2x2 and 3x3 arrays in transdermal insulin delivery systems [6, 7]. In rat experiments, the 2x2 array was used to deliver a 60 minute ultrasound treatment operating at $I_{sptp} = 100\ mW/cm^2$. The frequency of operation was 20 kHz and the ultrasound was pulsed with a 20% duty cycle and a 200 ms pulse duration [6]. Xylazine was used as a general anesthetic as well as to cause temporary (12 hr) hyperglycemia. Results in rats show a glucose level drop up to 276.5±61.9 mg/dL after the 60 minute ultrasound exposure [6]. Glucose levels continued to drop after the ultrasound treatment and 90 minutes after the initial ultrasound exposure there was a drop of 297.7±52.8 mg/dL [6].

Because therapeutic levels of insulin would need to be delivered to larger animals, a 3x3 array configuration was built. Animal tests on rabbits were performed under the same intensity and pulse conditions using the new array and a drop in glucose level in rabbits averaged 94.1±32.3 mg/dL at the end of the 60 minute treatment, and 136.1±26.1 mg/dL measured 90 minutes after the beginning of ultrasound treatment [7].

Animal testing on rats and rabbits have shown that the 2x2 and 3x3 circular arrays can be effective in making the skin more permeable to allow insulin to be delivered at therapeutic levels. The next step would be a larger animal, such as a large pig, to determine the possible effectiveness on humans.

1.3 Thesis Scope

The goal of this research is to further optimize the cymbal transducer to achieve a more efficient and effective insulin delivery system. Radiating area optimization is achieved through

the use of a rectangular cymbal geometry, thus minimizing the non-radiating area in the array. This change in geometry also closes the gap between the first flexural cap resonance and the ceramic length mode resonance. Near field exposimetry is performed and is compared to previous 2x2 and 3x3 designs. In addition, far field measurements to determine TVR and efficiency of the new device are presented. It is shown that the new 3x1 rectangular array is optimal in geometrical configuration and is nearly an order of magnitude more efficient than the previous 3x3 design. Animal tests on rabbits and pigs confirm the effectiveness of the rectangular array.

1.4 Thesis Organization

A theoretical background of skin physiology, sonophoresis, and of piezoelectric transducers is presented in the following chapter. The rectangular cymbal is discussed and analyzed in Chapter 3 and the performance of the device is presented in Chapter 4. Conclusions and suggestions for future work follow in Chapter 5.

Chapter 2

Theoretical Background

In order to develop an ultrasonic system for transdermal insulin delivery we must become familiar with various concepts. First, an understanding of skin physiology is needed in order to know what aspects of the skin's construction we must overcome to deliver larger molecule drugs transdermally. By knowing the biology of the skin we can hypothesize certain mechanisms of sonophoresis. Finally, the system in this research will use flextensional piezoelectric transducers. These three areas are discussed in depth here.

2.1 Skin Physiology

The skin can be separated into two layers, the epidermis and the dermis. The epidermis consists of five strata, or layers. In order from deep to superficial the layers are stratum basale, stratum spinosum, stratum granulosum, stratum lucidum, and stratum corneum. Thin skin, which covers the entire body except the palms, fingertips, and soles of the feet, lack the stratum lucidum and the other four layers are thinner [8]. Figure 2.1 shows the layers of the epidermis and the dermis.

Of the five layers, the stratum corneum is most important in transdermal drug delivery. This outermost layer of skin is made of tightly packed keratinocytes in a structure 20 to 30 cells thick [8]. In the stratum corneum, these keratinocytes are essentially dead cells composed mostly of keratin, a protein that gives the skin its protective properties. These dead cells rub off every day and are replaced by live keratinocytes undergoing continous mitosis in the stratum basale. Because this layer is a non-vascularized dead cell layer, it is important that any transdermal drug delivery method be able to overcome the protective

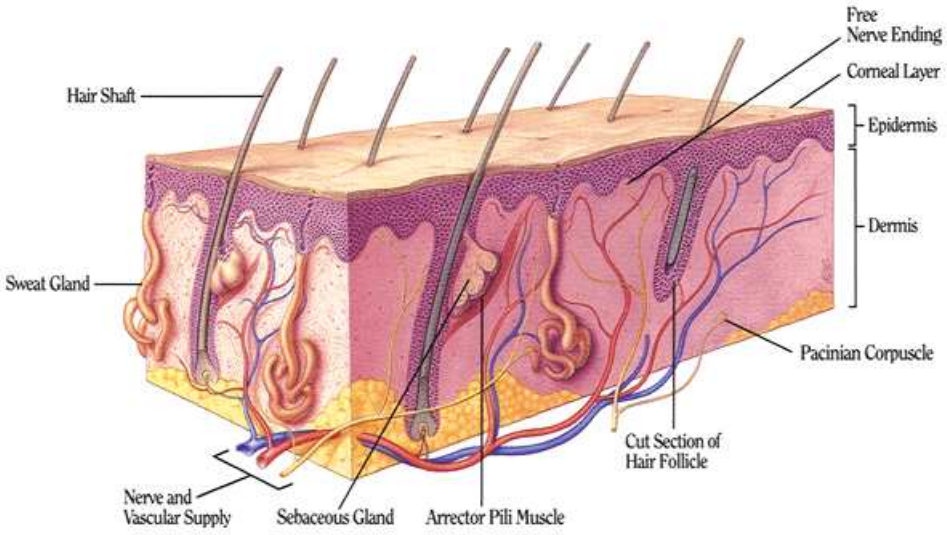

Figure 2.1: Human thick skin illustrating the layers of the epidermis and dermis

properties of the stratum corneum without causing any real damage to the tissue.

The second layer of skin, the dermis, is made of two layers and is a highly vascularized region containing nerve endings, hair follicles, and oil and sweat glands. It is this layer of the skin that we would like to reach. Once past the stratum corneum there is little in the way for insulin or any other drug to reach the dermis and be absorbed into the blood stream.

2.2 Mechanisms of Sonophoresis

The mechanisms of sonophoresis are not fully understood. However, there are theories as to what could be the cause of the increase in skin permeability seen during ultrasonic treatments. Among the theories, cavitation is the most popular but other possible mechanisms have not completely been ruled out. In fact, a combination of the following mechanisms is possible depending on the ultrasound conditions.

2.2.1 Cavitation

Acoustic cavitation is the generation and excitation of bubbles caused by large pressure rarefactions in an aqueous solution. Gaseous bubbles already existing in solution can be excited by acoustic waves. In addition, large rarefactions caused by acoustic waves that overcome the tensile strength of the solution can create bubbles, leading to either stable or transient cavitation [9].

Stable cavitation includes the excitation of bubbles and in general does not include their violent collapse. The intensity and frequency of oscillation are not great enough to induce collapse of the bubble. However, microstreaming can occur during stable cavitation. Microstreaming occurs mainly near boundaries and is the result of the medium absorbing acoustic energy and translating this energy into a flow [9]. In tissue, the stratum corneum is a rigid boundary and this streaming may cause shear forces large enough to disrupt the cell structure and increase permeability.

Transient caviation includes the growth and violent collapsing of bubbles. Near boundaries this can cause microjets able to penetrate the surface [4]. Transient cavitation occurs under higher acoustic pressure amplitudes [9]. Higher acoustic pressures apply a larger initial tension during the rarefaction period. On the compression phase, the bubble is large enough that collapse does not occur before the next rarefaction phase, creating an even larger bubble. When the bubble finally does collapse, a large portion of the energy is transferred to the collapse and not to dissipation, allowing the formation of high energy jet streams.

As a mechanism for sonophoresis, there are two possibilities. The first is the excitation of existing gas pockets in the stratum corneum between and within keratinocytes. Figure 2.2 shows a schematic of this stable cavitation occurring near the karatinocytes. Similar acoustic excitation of gas pockets in hair follicles and sweat glands near the stratum corneum also leads to stable cavitation. It is theorized that the acoustic excitation of these gas pockets disrupts the brick-like structure of the stratum corneum enough to allow larger molecule drugs through. Some have theorized that the disordering caused in the lipid layers creates

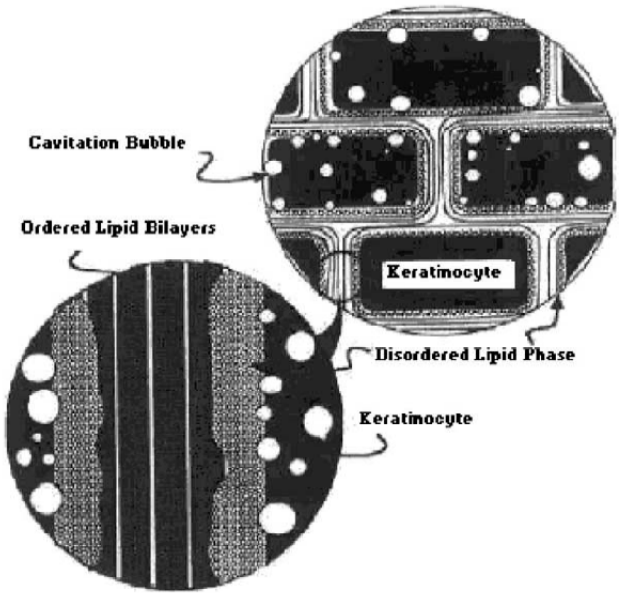

Figure 2.2: Schematic of stable cavitation occurring in and between layered karatinocytes [10]

aqueous channels that make the skin more permeable [11].

Increased skin permeability during ultrasound treatments has also been attributed to transient cavitation. Microjets, shown schematically in Figure 2.3, can form during bubble collapse, with the strongest jets penetrating the surface of the stratum corneum [4]. As mentioned earlier, transient cavitation occurs at higher acoustic pressures and there are known intensity thresholds above which it occurs. In addition, there is a frequency dependance, with higher intensities needed at higher frequencies to induce transient cavitation. In effect, at higher frequencies, the rarefaction phase is too short to create a large enough bubble and a larger amplitude is required to induce rapid growth and violent collapse of bubbles [9].

Finally, because of the possible destructive effects of transient cavitation, bioeffects of cavitation must be considered. Penetration of the stratum corneum may be acceptable but further penetration would begin to reach layers of the skin containing nerve endings, inducing pain and undersired skin damage.

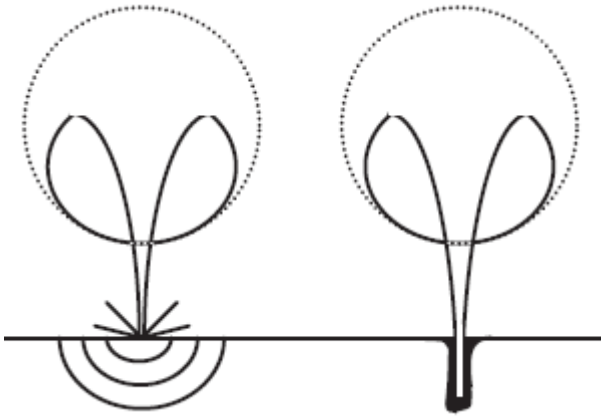

Figure 2.3: Schematic of microjet formation at the stratum corneum during volient bubble collapse as a result of transient cavitation [4]

2.2.2 Thermal Effects

Increased permeability of the skin has also been seen under increased temperature conditions. An increase in temperature, in general, increases diffusion across a membrane. If a temperature increase is seen at the dermis layer, blood vessels will dilate, increasing the intake of a drug transdermally delivered.

During ultrasound exposure, energy from acoustic waves are absorbed by the skin. The amount of energy absorbed is proportional to the frequency and intensity of sound. This energy absorption by tissue has been used for tissue ablation devices for cancer treatments where a localized temperature rise in tissue due to ultrasound exposure is able to damage cancerous tissue. In a drug delivery system, such a large increase in temperature is undesirable. However, depending on the intensity and frequency conditions, a rise in temperature will occur. It has been shown that producing a temperature profile similar to that created by sonophoresis devices it is possible to obtain increased diffusion through the skin [12]. However, a temperature increase due to ultrasound exposure gives far better results, indicating the existence of additional mechanisms [12].

2.3 Piezoelectric Transducers

In its most simplest definition, the word transducer refers to a device that converts energy from one form to another. In specific, we will be looking at electroacoustic transducers, devices that convert electric energy into acoustic energy. These types of devices are seen in loudspeakers as well as in sonar systems. In 1880, the Curie brothers discovered what is known as the direct piezoelectric effect, inducing strain in a material through the use of an applied electric field [13].

2.3.1 The Piezoelectric Effect

In piezoelectric materials there exists a polarization under zero electric field conditions. Under non-zero electric field conditions, the polarization charge varies and for this reason it can sometimes be more convenient to analyze the materiel in terms of the electric displacement field. This also allows for the expression of Gauss' law in terms of only the free charge in the system and not the changing polarization charge. The electric displacement in free space is given by Equation 2.1.

$$D = \epsilon_o E \tag{2.1}$$

When a polarization P exists, the electric displacement is given by

$$D = \epsilon_o E + P \tag{2.2}$$

In addition, we can express the polarization in terms of a dielectric susceptibility χ as shown in Equation 2.3

$$P = \chi \epsilon_o E \tag{2.3}$$

This allows us to simplify Equation 2.2 and write the electric displacement as

$$D = \epsilon E \tag{2.4}$$

where ϵ is the total dielectric permittivity of the material which includes the effects of the polarization P.

The piezoelectric material is also governed by Hooke's Law in linear systems. Thus, an induced stress will cause an induced strain determined by the material's elastic properties. For piezoelectric materials we write this experssion as

$$S = sT \tag{2.5}$$

where S is the unitless strain, T is the stress in $[N/m^2]$, and s is the compliance of the material in $[m^2/N]$.

Mathematical derivation of the piezoelectric effect can be derived using thermodynamic potential functions [13]. This analysis is beyond the scope of this thesis and will be omitted. The resulting expressions for the strain and the electric displacement including effects from both mechanical and electrical properties are

$$\begin{aligned} S &= s^E T + d^t E \\ D &= dT + \epsilon^T E \end{aligned} \tag{2.6}$$

where s^E is the compliance under zero electric field in $[m^2/N]$, ϵ^T is the permittivity under zero stress, d is the piezoelectric strain constant in $[C/N]$, and the superscript t represents a transpose of the matrix. Tensor representation is necessary due to the possibility of anisotropic conditions as well as the need to represent displacement and shear strains in any direction of the material.

There are a variety of piezoelectric materials that have been used, all with varying piezoelectric constants governing their operation. Some examples include quartz, barium titanate ($BaTiO_3$), and lead zirconate titanate ($PbZrTiO_3$). This particular work uses lead zirconate titanate (PZT) and further analysis will limit itself to the properties of PZT. The matrix forms of s, d, and ϵ for a typical piezoelectric ceramic are given in Equation 2.7.

$$\begin{aligned} s^E &= \begin{bmatrix} s_{11} & s_{12} & s_{13} & 0 & 0 & 0 \\ s_{12} & s_{11} & s_{13} & 0 & 0 & 0 \\ s_{13} & s_{13} & s_{33} & 0 & 0 & 0 \\ 0 & 0 & 0 & s_{44} & 0 & 0 \\ 0 & 0 & 0 & 0 & s_{44} & 0 \\ 0 & 0 & 0 & 0 & 0 & 2(s_{11} - s_{12}) \end{bmatrix} \\ d &= \begin{bmatrix} 0 & 0 & 0 & 0 & d_{15} & 0 \\ 0 & 0 & 0 & d_{15} & 0 & 0 \\ d_{31} & d_{31} & d_{33} & 0 & 0 & 0 \end{bmatrix} \\ \epsilon^T &= \begin{bmatrix} \epsilon_1 & 0 & 0 \\ 0 & \epsilon_2 & 0 \\ 0 & 0 & \epsilon_3 \end{bmatrix} \end{aligned} \tag{2.7}$$

Expanding the tensor notation into nine equations using Equation 2.6 we obtain

$$\begin{aligned}
S_1 &= s_{11}^E T_1 + s_{12}^E T_2 + s_{13}^E T_3 + d_{31} E_3 \\
S_2 &= s_{12}^E T_1 + s_{11}^E T_2 + s_{13}^E T_3 + d_{31} E_3 \\
S_3 &= s_{13}^E T_1 + s_{13}^E T_2 + s_{33}^E T_3 + d_{33} E_3 \\
S_4 &= s_{44}^E T_4 + d_{15} E_2 \\
S_5 &= s_{44}^E T_5 + d_{15} E_1 \\
S_6 &= s_{66}^E T_6 \\
D_1 &= \epsilon_1^T E_1 + d_{15} T_5 \\
D_2 &= \epsilon_1^T E_2 + d_{15} T_4 \\
D_3 &= \epsilon_3^T E_3 + d_{31}(T_1 + T_2) + d_{33} T_3
\end{aligned} \tag{2.8}$$

Notice there are six strain equations, with S_4 through S_6 corresponding to shear strain of the material. In general, the 3 direction is the direction parallel to the direction of polarization with the 1 and 2 directions corresponding to directions perpendicular to the polarization vector. Thus, as an example, the constant d_{33} gives the piezoelectric strain constant for an electric field applied parallel to the polarization, and strain induced in the 3 direction. The constant d_{31} relates electric field applied parallel to the polarization and resulting strain in the 1 direction, perpendicular to the polarization.

2.3.2 PZT 3-1 Bar Analysis

Section 2.3.1 described the equations necessary to determine the strain and electric displacement of a PZT ceramic. For this research, a rectangular ceramic is used in the 3-1 mode, electric field applied parallel to the direction of polarization and motion of interest perpendicular to the direction of polarization. An analysis to determine the expressions for displacement, strain, and other important characteristics follows.

2.3.2.1 Characteristic 3-1 Equations

Consider the ceramic long bar shown in Figure 2.4. By applying a voltage to the faces of

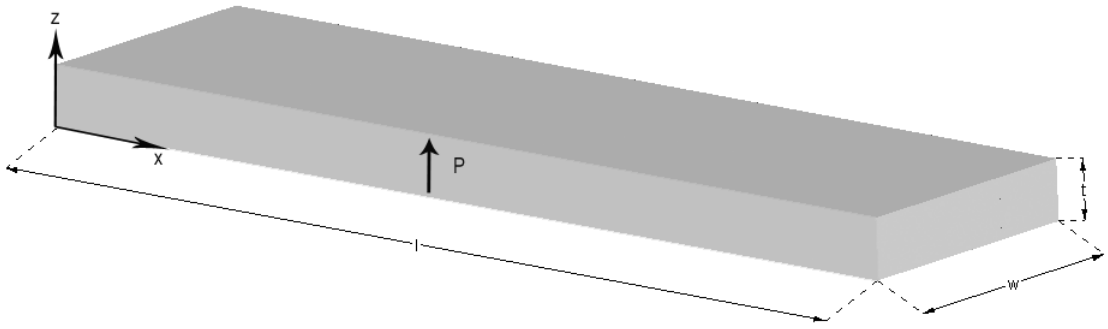

Figure 2.4: 3-1 PZT bar polarized in the z direction with motion of interest in the x direction

the ceramic at $z = 0$ and $z = t$ and neglecting fringing fields, E_1 and E_2 are zero. We can also assume that S_2 and S_3 are negligibly small. Under these conditions, Equation 2.6 reduces to

$$\begin{aligned} S_1 &= s_{11}^E T_1 + d_{31} E_3 \\ D_3 &= d_{31} T_1 + \epsilon_{33}^T T_3 \end{aligned} \tag{2.9}$$

Assuming harmonic motion in the x direction we can express the displacement of the ceramic as

$$\xi(x) = (A \sin(kx) + B \cos(kx)) \tag{2.10}$$

where $k = \omega/c_b^E$, c_b^E is the sound speed of waves in the long bar (subscript b) under zero electric field conditions, and A and B are constants to be determined. The sound speed can also be expressed as $c_b^E = 1/\sqrt{\rho s_{11}^E}$ where ρ is the density of the material.

We have free boundary conditions at the bar ends, so $T_1(x = 0) = T_1(x = \ell) = 0$. The strain along the bar is calculated to be

$$S_1(x) = k(A\cos(kx) - B\sin(kx)) \tag{2.11}$$

Combining the two conditions allows us to solve for A and B, giving an expression for the displacement shown in Equation 2.12.

$$\xi(x) = \frac{d_{31}E_o}{k}[\sin(kx) - \tan(\frac{k\ell}{2})\cos(kx)] \tag{2.12}$$

Solving for the strain along the bar then becomes straight forward and we obtain

$$S_1(x) = d_{31}E_o[\cos(kx) + \tan(\frac{k\ell}{2})\sin(kx)] \tag{2.13}$$

Using the expression for S_1 from Equation 2.9 we can solve for $T_1(x)$ to find the stress along the bar as given in Equation 2.14.

$$T_1(x) = \frac{d_{31}E_o}{s_{11}^E}[\cos(kx) + \tan(\frac{k\ell}{2})\sin(kx)] \tag{2.14}$$

In addition to mechanical parameters, it is also useful to determine the electrical characteristics of the device. The electrical properties are often used to characterize the transducer and knowledge of the voltage applied and current through the ceramic can be used to determine input power. We can begin with the expression from Equation 2.9 for D_3. Making the necessary substitutions for T_1 and E_3 the solution to D_3 becomes

$$D_3(x) = \left\{ \frac{d_{31}^2}{s_{11}^E}[\cos(kx) + \tan(\frac{k\ell}{2})\sin(kx)] + [\epsilon_{33}^T - \frac{d_{31}^2}{s_{11}^E}] \right\} E_o \tag{2.15}$$

By Ampere's law we can solve for the current through the ceramic by integrating the time rate of change of the electric displacement over the surface area of the device using Equation 2.16.

$$I = \int_0^w \int_0^\ell \frac{\partial D_3}{\partial t} dxdy \tag{2.16}$$

After integrating and including harmonic time dependence, $I(t)$ becomes

$$I(t) = \left\{ \frac{d_{31}^2}{s_{11}^E k}\sin(k\ell)[1 + \tan^2(\frac{k\ell}{2})] + \ell[\epsilon_{33}^T - \frac{d_{31}^2}{s_{11}^E}] \right\} j\omega w E_o e^{j\omega t} \tag{2.17}$$

In order to solve for the admittance we need to know the voltage applied and this can be solved by knowing that the potential difference between the two electrodes is

$$V = \int_0^t E_3 dt \tag{2.18}$$

Dividing the current by the voltage we can find the admittance to be

$$Y = \frac{j\omega w d_{31}^2}{s_{11}^E kt} \sin(k\ell)[1 + \tan^2(\frac{k\ell}{2})] + \frac{j\omega w\ell}{t}[\epsilon_{33}^T - \frac{d_{31}^2}{s_{11}^E}] \tag{2.19}$$

From the admittance expression we can see that the resonance condition arises when $k\ell = (2n-1)\pi$. Under this condition, the first length mode resonance frequency of the rectangular ceramic can be expressed as

$$f_r = \frac{c_b^E}{2\ell} = \frac{1}{2\ell\sqrt{\rho s_{11}^E}} \tag{2.20}$$

As an example, Figure 2.5 shows the analytical admittance magnitude and phase of a rectangular ceramic with a length of 60 mm and 3 mm thickness. Notice that at the first and second resonance frequencies the admittance magnitude tends to infinity. This occurs because losses in the device are not accounted for. A MATLAB program with a user interface has been written to show the displacement of the bar at any frequency given the PZT constants. The full code is given in Appendix A.

If we take a closer look at the expression for the admittance we can see two terms, the left most term appears to be the result of the mechanical properties of the material and sets the mechanical resonance conditions while the rightmost term is the electrical component that essentially looks like a capacitor with an equivalent permittivity. We can see this capacitive property by letting $k\ell \ll 1$. Equation 2.19 reduces to

$$Y_{lowfreq} = j\omega\frac{w\ell}{t}\epsilon_{33}^T \tag{2.21}$$

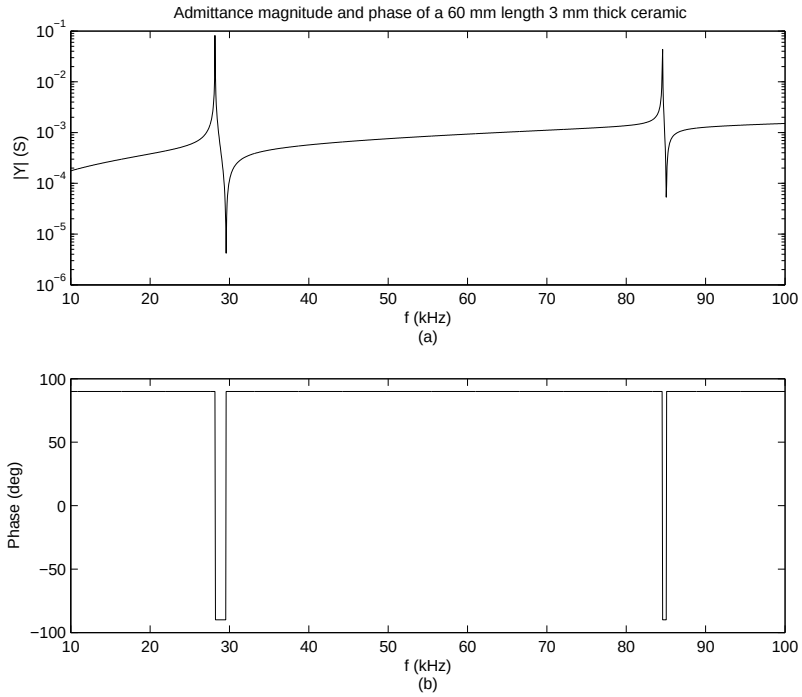

Figure 2.5: Admittance (a)magnitude and (b)phase of a rectangular 3-1 mode bar with a length of 60 mm and 3 mm thickness

This is the expression for the admittance of a capacitor with capacitance $w\ell\epsilon_{33}^T/t$. If necessary, we can determine ϵ_{33}^T for the rectangular ceramic by measuring the capacitance at the low frequency limit. At higher frequencies, the permittivity has a "correction" factor given by d_{31}^2/s_{11}^E.

2.3.2.2 3-1 Bar Equivalent Circuit

It is often easier to analyze transducer characteristics by modeling the entire system as an electrical circuit. Mechanical and acoustic properties can be modeled as circuit elements making analysis simpler. We would like to model the rectangular ceramic from the voltage applied to the force produced at the ends of the bar. This can be done using the generalized circuit diagram shown in Figure 2.6. The transformer accounts for the transduction of electrical energy to mechanical energy while the voltage and current in the mechanical domain

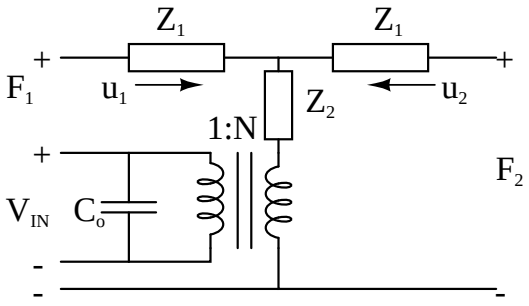

Figure 2.6: Generalized circuit used to model a 3-1 mode rectangular bar transducer

are represented by the force and velocity respectively. Z_1 and Z_2 represent impedances to be determined and C_o is the clamped capacitance.

In order to find expressions for the velocity and force of the bar, we must begin with the time harmonic expression for the displacement given in Equation 2.10. Taking the derivative of Equation 2.10 with respect to time we derive an expression for the velocity along the bar to be

$$u(x) = j\omega(A\sin(kx) + B\cos(kx)) \tag{2.22}$$

Defining $u_1 = u(0)$ and $u_2 = u(\ell)$ we can solve for the velocity in terms of the two end bar velocities, giving the solution

$$u(x) = \left[\frac{u_2 - u_1\cos(k\ell)}{\sin(k\ell)}\right]\sin(kx) + u_1\cos(kx) \tag{2.23}$$

Substituting the A and B constants into $\xi(x)$ and simplifying we find that the displacement varies along the bar in terms of the end velocities as shown in Equation 2.24.

$$\xi(x) = \frac{1}{j\omega \sin(k\ell)}[u_1 \sin(kx - k\ell) + u_2 \sin(kx)] \tag{2.24}$$

Solving for the force requires solving for the stress as described in Section 2.3.2.1 and dividing by the cross sectional area of the end of the bar. The expression for the force is obtained as

$$F(x) = \frac{wt\rho c_b^E}{j \sin(k\ell)}[u_1 \cos(kx - k\ell) + u_2 \cos(kx)] - \frac{d_{31}w}{s_{11}^E}V_{IN} \tag{2.25}$$

Defining $Z_o = \rho wtc_b^E$ and solving Equation 2.25 at $F_1 = F(x = 0)$ we find that the force on one end of the bar given the input voltage V_{IN} is

$$F_1 = F(x = 0) = \frac{Z_o}{j \sin(k\ell)}u_1 \cos(k\ell) + \frac{Z_o}{j \sin(k\ell)}u_2 - \frac{d_{31}w}{s_{11}^E}V_{IN} \tag{2.26}$$

By Kirchoff's voltage law we can also solve for the voltage loop that includes the voltage drop F_1 as

$$F_1 = (Z_1 + Z_2)u_1 + Z_2u_2 + NV_{IN} \tag{2.27}$$

Solving for like terms from Equations 2.26 and 2.27 we can solve for the individual circuit components. A similar analysis using the boundary at $x = \ell$ gives the same solution for the impedances. The final circuit is shown in Figure 2.7 and the circuit component expressions are given in Equation 2.28.

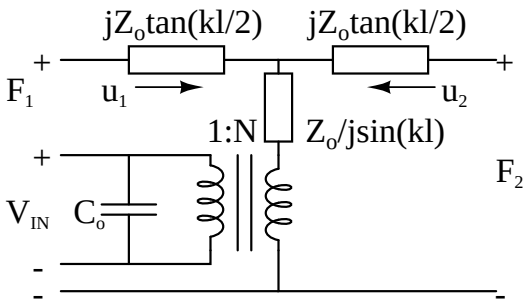

Figure 2.7: Rectangular 3-1 mode bar equivalent circuit

$$\begin{aligned} Z_o &= \rho w t c_b^E \\ N &= \frac{w d_{31}}{s_{11}^E} \\ C_o &= \frac{wl}{t}[\epsilon_{33}^T - \frac{d_{31}^2}{s_{11}^E}] \\ k &= \frac{\omega}{c_b^E} \\ c_b^E &= \frac{1}{\sqrt{\rho s_{11}^E}} \end{aligned} \tag{2.28}$$

While this model works at all frequencies, it often useful to have a simpler model when working around resonance. For transducers in this work, the circuit model in Figure 2.8 is used, where R_e is the dielectric loss, C_o is the clamped capacitance, C_m is the motional capacitance, L_m is the motional inductance, R_m is the mechanical loss term, R_r the radiation resistance, and X_r is the radiation reactance. Note that although all values are in electrical units, the mechanical and acoustical terms were scaled by the square of a transduction factor ϕ in order to obtain the correct units. This transduction factor depends on the design of the transducer.

In cases where the transducer operates like a piston and meets the $ka \ll 1$ condition, the radiation reactance can be modeled as an inductance. In this case the transducer appears to be mass loaded by a cylindrical volume of fluid with mass $m = \pi a^2 \rho(8a/3\pi)$ where a is

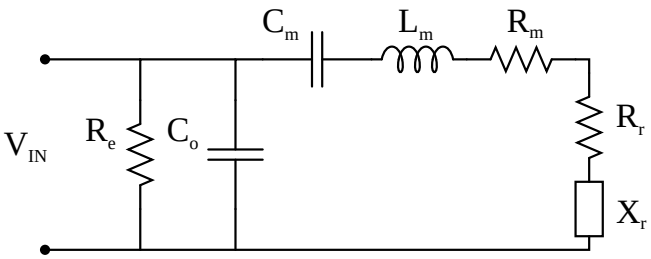

Figure 2.8: Equivalent circuit for an underwater transducer operating at or near resonance

the radius of the radiating surface. For small transducers this can become a large factor and can affect system efficiency.

2.3.3 Flextensional Transducers: The Cymbal

A flextensional transducer is a sound projector or receiver that uses the flexural motion of a shell covered ceramic as a mechanical transformer for force and displacement. To date, there are seven such types of transducers with their basic geometries shown in Figure 2.9

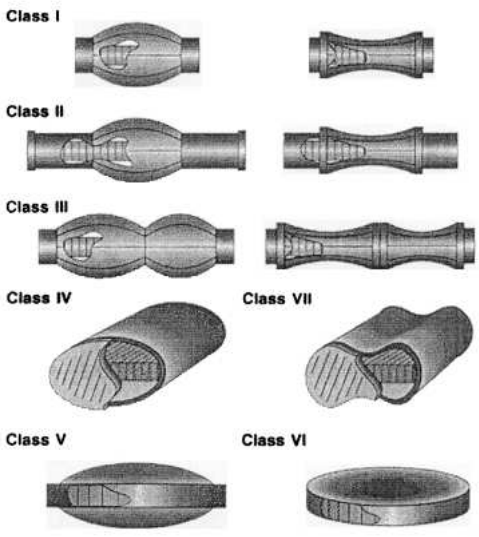

Figure 2.9: Schematics of the classifications of the seven types of flextensional transducers

The cymbal transducer is a Class V flextensional transducer, with a PZT ceramic sandwiched between two metal end caps. A cutaway schematic of the cymbal is shown in Figure 2.10. As seen in diagram, small displacements of the ceramic are converted into large

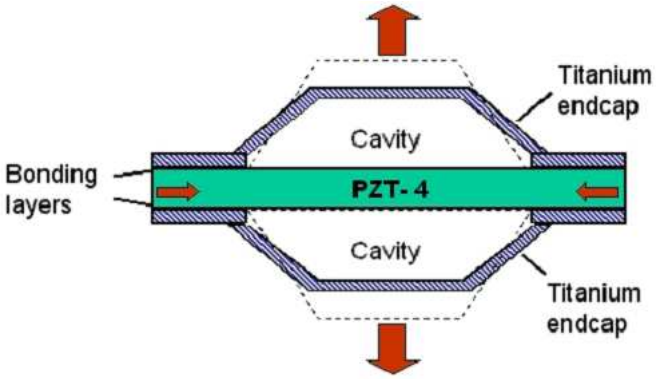

Figure 2.10: Schematic of a cymbal transducer indicating ceramic and cap displacement

displacements of the end caps. In this way, high acoustic intensities can be achieved.

As a first approximation of the displacement of the circular cap used in previous studies, we can approximate the cap as a thin shell. This approximation allows us to express the axial motion of the cap as

$$\frac{\partial^2 y}{\partial t^2} = \frac{-\kappa^2 E}{\rho(1-\sigma^2)}\nabla^2(\nabla^2 y) \tag{2.29}$$

where y is the displacement, ρ is the volume density, σ is Poisson's ratio, E is Young's modulus, and κ is the radius of gyration. For a circular plate, $\kappa = d/\sqrt{12}$ where d is the plate thickness. Letting $y = \Psi e^{j\omega t}$ we obtain the equation

$$\begin{aligned} \nabla^2(\nabla^2\Psi) - g^4\Psi &= 0 \\ g^4 &= \frac{\omega^2\rho(1-\sigma^2)}{\kappa^2 E} \end{aligned} \tag{2.30}$$

The bounded solution to Equation 2.30 is

$$\Psi = AJ_0(gr) + BI_0(gr) \tag{2.31}$$

where $J_n(gr)$ and $I_n(gr)$ are the Bessel function of the first kind and the modified Bessel function of order n respectively. Applying the clamped boundary condition at $r = a$ we can find the transcendental expression for the allowed values of g to be

$$\frac{J_0(ga)}{J_1(ga)} = -\frac{I_0(ga)}{I_1(ga)} \tag{2.32}$$

Solutions to the transcendental equation give the expression for the first resonant frequency of the flexural motion of the cap to be

$$f = \frac{g_1^2 d}{2\pi a^2\sqrt{12}}\left[\frac{E}{\rho(1-\sigma^2)}\right]^{1/2} \tag{2.33}$$

We can see that the first resonance frequency of the flexural motion of the cap is proportional to the square root of the ratio of the Young's modulus and the density of the cap material.

Continuing our analysis, we can follow an approximation for the equation of motion for a shallow shell of radius a on a flextensional transducer [14]. Equation 2.31 becomes

$$\Psi(r) = C_1 J_0(\gamma r) + C_2 I_0(\gamma r) + C_3 \tag{2.34}$$

where C_1, C_2, and C_3 are constants to be determined, γ is defined by Equation 2.35, and R is the radius of curvature of the shell.

$$\gamma = \frac{\rho d\omega}{D} - \frac{dE}{DR^2} \qquad D = \frac{Ed}{12(1-\sigma^2)} \tag{2.35}$$

Imposing the same clamped boundary conditions we can obtain a new solution to the equation of motion of the cap to be

$$\Psi(r) = C_1\Big\{([J_0(\gamma r) - J_0(\gamma a)] + [I_0(\gamma r) - I_0(\gamma a)]\frac{J_1(\gamma a)}{I_1(\gamma a)}\Big\} \tag{2.36}$$

The constant C_1 remains unknown. However, we can still obtain a proportionality expression between the first resonant frequency of the shell and the material properties [14]. For the thin shell with radius a and cavity diameter ϕ_c the proportionality expression is

$$f \propto \left\{\frac{E}{\rho}\Big[\frac{1}{\phi_c^2(1-\sigma^2)} + \frac{1}{R^2}\Big]\right\}^{1/2} \tag{2.37}$$

As in Equation 2.33, we see the same proportionality to the ratio of the Young's modulus and density of the material. In addition, we can see that increases in either the cavity diameter or the radius of curvature will result in a decrease in the first resonance frequency. For the cymbal transducer, the caps are not perfectly curved shells but this analysis gives us a good physical intuition for what effect a change in cap material or geometry will have on the device.

2.4 Acoustic Measurements

To determine transducer performance it is necessary to obtain various acoustic measurements. Far field measurements report transducer directivity, efficiency, and source level at various frequencies. In addition, we are interested in near field intensity measurements given that the device in this work will be used in close proximity to the skin. For near field measurements, an exposimetry system is used to determine an intensity profile on a given plane. Principles of these measurements are described in this section. Some expressions described are not used in this research but are included for completeness. Before a description of measurements, some background in simple acoustic relations is given.

2.4.1 Acoustic Relations

Acoustic waves are the result of pressure disturbances in a medium that oscillate molecules back and forth in the direction of propagation, creating a longitudinal wave. In any medium, acoustic propagation is governed by a wave equation, derived from the equation of state, the equation of continuity, and Euler's equation. The linearized form of these equations are listed in Equation 2.38 and a full derivation can be found in the literature [15].

$$\begin{aligned} p &= Bs \\ \frac{\partial s}{\partial t} + \nabla \cdot \vec{u} &= 0 \\ \rho_o \frac{\partial \vec{u}}{\partial t} &= -\nabla p \end{aligned} \tag{2.38}$$

As given in Equation 2.38, p is the acoustic pressure, B is the bulk modulus, s is the condensation, $\vec{u}$ is the particle velocity, and ρ_o is the equilibrium density of the medium. By combining the three equations we can obtain the linearized wave equation to be

$$\nabla^2 p = \frac{1}{c^2}\frac{\partial^2 p}{\partial t^2} \tag{2.39}$$

where c is the speed of sound given by $\sqrt{B/\rho_o}$. A similar wave equation can be found using the particle velocity.

Solutions to the wave equation take the form

$$p(\vec{r}, t) = f(\omega t \pm \vec{k} \cdot \vec{r}) \tag{2.40}$$

where the relationship $|\vec{k}| = \omega/c$ holds and $\vec{r}$ is the three dimensional space variable that can be specified in any coordinate system. If we limit ourselves to one dimension in cartesian coordinates the solution to the pressure can be expressed as

$$p(x, t) = Ae^{j(\omega t - kx)} + Be^{j(j\omega + kx)} \tag{2.41}$$

where A and B are complex constants that can be determined by boundary conditions. The particle velocity $\vec{u}$ can then be determined using Euler's equation.

The acoustic intensity is defined as the time average flow of energy through a unit area per unit time normal to the direction of propagation. The instantaneous intensity can be found by calculating the product pu and the time average is expressed as

$$I =< pu >_t = \frac{1}{T}\int_0^T pudt \tag{2.42}$$

For plane waves the expression for the intensity simplifies to

$$I = \frac{p^2}{2\rho c} \tag{2.43}$$

where p is the peak pressure.

For acoustic waves we can describe the medium and the longitudinal waves by impedances. The specific acoustic impedance is expressed as

$$Z = \frac{p}{u} \tag{2.44}$$

where Z is not necessarily a real quantity since p and u can be complex. For a plane wave the specific acoustic impedance is $\pm\rho c$, depending on the direction of wave propagation. In addition, we can describe the acoustic properties of the material by using its characteristic acoustic impedance, or the product of the material density and the speed of sound in the material. We can see that for plane waves, the magnitude of the specific and characteristic acoustic impedances are equal. The characteristic acoustic impedance is useful in acoustic transmission and reflection problems. In particular, the reflected and transmitted power at a boundary is governed by the differences in the characteristic acoustic impedances of the media. Of relevance to this research are the characteristic acoustic impedances of various tissues. Table 2.1 lists different tissues along with their characteristic acoustic impedances.

Finally, it is common to express sound pressures and intensities in terms of levels on a logarithmic scale. This decibel scale can make analysis of relative intensities and pressures easier. On the logarithmic scale, the intensity level is defined as

Table 2.1: Characteristic acoustic impedances of various tissues of interest in medical ultrasound [16]

Medium	$\rho(kg/m^3)$	c (m/s)	$\rho c(kg/[m^2 s])$
Air	1.2	333	0.4×10^3
Blood	1.06×10^3	1566	1.66×10^6
Bone	$1.38 - 1.81 \times 10^3$	2070-5350	$3.75 - 7.38 \times 10^6$
Brain	1.03×10^3	1505-1612	$1.55 - 1.66 \times 10^6$
Fat	0.92×10^3	1446	1.33×10^6
Kidney	1.04×10^3	1567	1.62×10^6
Lung	0.4×10^3	650	0.26×10^6
Liver	1.06×10^3	1566	1.66×10^6
Muscle	1.07×10^3	1542-1626	$1.65 - 1.74 \times 10^6$
Spleen	1.06×10^3	1566	1.66×10^6
Distilled water	1.00×10^3	1480	1.48×10^6

$$IL = 10 \log \left(\frac{I}{I_{ref}} \right) \tag{2.45}$$

where I is the sound intensity, I_{ref} is a defined reference intensity, and log is the base 10 logarithm. Intensity levels are expressed in terms of their reference intensity. Thus, an intensity level would be expressed in dB $re\ I_{ref}$.

A sound pressure level (SPL) can also be found given that for plane and spherical waves the intensity is expressed by Equation 2.43. Substituting for the intensities in Equation 2.45 we obtain

$$SPL = 20 \log \left(\frac{P}{P_{ref}} \right) \tag{2.46}$$

Typical references for water measurements are $I_{ref} = 6.76 \times 10^{-9}\ W/m^2$ and P_{ref} =1 μPa [15].

2.4.2 Far Field Measurements

Acoustic fields near a sound projector are often difficult to determine and thus a transducer is typically characterized by its performance in the far field. Differentiation between the near and far field varies depending on the wavelength and radiating area of the transducer but in general the far field begins at a distance near D^2/λ, where D is the transducer diameter and λ is the wavelength.

In many cases, transducers are not omnidirectional radiators. Therefore, in order to accurately specify the far field performance of the device, measurement of a beam pattern is necessary and can be expressed mathematically as

$$b(\theta,\phi) = 10\log\left[\frac{I(r,\theta,\phi)}{I_{ax}(r)}\right] = 20\log[H(\theta,\phi)] \tag{2.47}$$

where $I_{ax}(r)$ is the intensity on the acoustic axis and $H(\theta,\phi)$ is a directional factor that can be derived from expressing the acoustic pressure amplitude in the far field as

$$P(r,\theta,\phi) = P_{ax}(r)H(\theta,\phi) \tag{2.48}$$

In addition, we can specify a directivity factor which is essentially the ratio of the acoustic intensity on the acoustic axis to the intensity which would be measured if the same power were radiated omnidirectionally. This can be expressed as

$$D = \frac{4\pi}{\int_{4\pi} H^2(\theta,\phi)d\Omega} \tag{2.49}$$

We can see that the expression for D is inversely proportional to the average of $H^2(\theta, \phi)$ over solid angle. We can also specify a directivity index as

$$DI = 10 \log(D) \tag{2.50}$$

This directivity index gives a quick indication of how the transducer radiates power. As an example, the directivity of an omnidirectional radiator is unity, giving a zero DI. If a simple source is by a rigid baffle, the directivity becomes two and the DI changes accordingly.

A good measure of the strength of an acoustic radiator is its source level (SL). Acoustic pressure can be measured on the acoustic axis in the far field where it is assumed the pressure varies as $1/r$ (spherical spreading). The pressure is then extrapolated to a distance of 1 m from the transducer and the source level is given by

$$SL(re\ P_{ref}) = 20 \log \left[\frac{P_e(1)}{P_{ref}} \right] \qquad P_e(1) = \frac{P_{ax}(1)}{\sqrt{2}} \tag{2.51}$$

When a directivity index is known or measured, the source level in water becomes

$$SL(re\ 1\ \mu Pa) = 10 \log(W) + DI + 170.9 \tag{2.52}$$

where W is the total acoustic power radiated by the source.

Two other important transducer measurements are the transmitting voltage response (TVR) and the transmitting current response (TCR). Both measurements are a ratio of the sound pressure at a distance of 1 m in a specified direction to the current or voltage applied. The

reference voltage and current are 1 V and 1 A for TVR and TCR respectively. They are expressed in dB re 1 $Pa \cdot m/V$ and dB re 1 $Pa \cdot m/A$. The relationship between TCR and TVR is

$$TCR = TVR + 20 \log |Z| \tag{2.53}$$

where $|Z|$ is the electrical impedance magnitude of the transducer.

Finally, we would like to know how efficient a transducer is. Ideally we would like to convert all electrical power delivered to the transducer into acoustic power out. However, in our particular system, the transducer behaves like a capacitor and the conversion of electrical to acoustic energy is far from ideal. In a typical system, an electrical signal is sent to the transducer via a power amplifier. Power amplifiers are typically specified in terms of electrical power units, or Watts (W). For this reason it is convenient to use an efficiency ratio known as the volt-amp per watt ratio (VA/W). Applied voltage and current are measured at the transducer and the product is divided by the total acoustic power output measured. An ideal ratio would equal one. For the cymbal transducers used in arrays a typical value of VA/W is on the order of 100.

2.4.3 Near Field Exposimetry

Of interest to this research is what the intensity profile looks like close to the transducer. The transducer face will be approximately 1 mm away from the skin when in use and at that distance, we would like to know how the acoustic intensity is distributed spatially. A method of measuring this profile is to use an exposimetry system. In such a system, the transducer is stationary and a hydrophone on a motor controlled system makes user specified steps and measures the pressure in a plane in front of the transducer. A simplified exposimetry system diagram is shown in Figure 2.11 and the specific system used in this work is described in Chapter 4. The hydrophone's movement is computer and motor controlled and a plane of

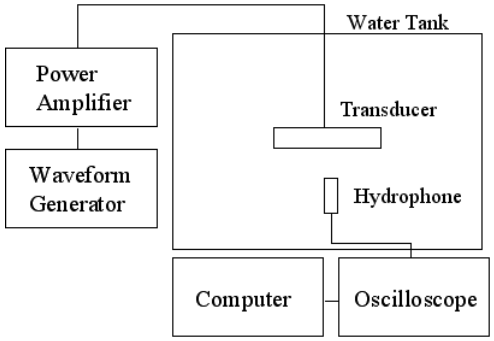

Figure 2.11: Diagram of exposimetry setup

pressure measurements can be made. As an example, Figure C.12 shows an exposimetry measurement made for a 3x3 circular cymbal array. The intensity is normalized to the maximum intensity and is shown in dB.

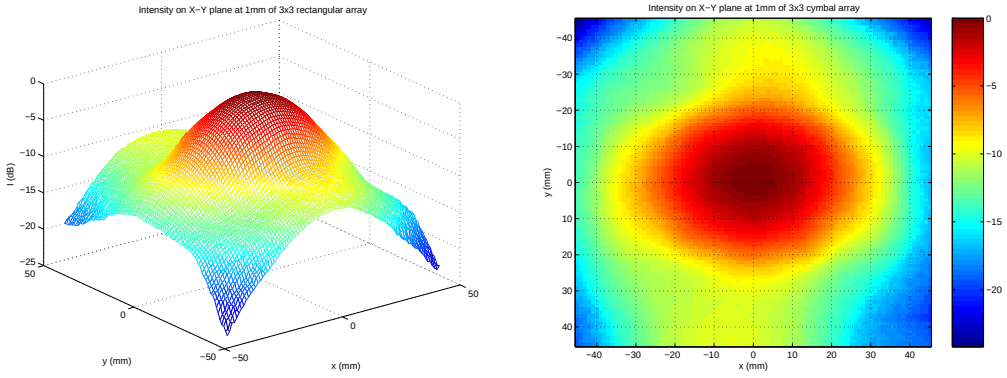

Figure 2.12: Exposimetry example of a 3x3 circular cymbal transducer array 1 mm from the transducer face

Exposimetry measurements are helpful in determining where the maximum intensity is and how the power is distributed in a plane near the transducer face. Measurements of this intensity are expressed in various ways in the medical ultrasound field. The time average acoustic intensity was described in Section 2.4 but sometimes ultrasound exposures are pulsed and a temporal or spatial peak or average better describes the intensity. For an instantaneous intensity $I_i(r,t)$, the field can be specified by its temporal and spatial peak (I_{sptp}). This is the intensity specification that will typically be used in this research.

Additionally, the intensity can be characterized by its temporal average as

$$I_{spta} = \frac{1}{T}\int_0^T I_i(r_{max}, t)dt \tag{2.54}$$

where T is the pulse period and r_{max} refers to the point in space of maximum intensity. We can also express the intensity in terms of its spatial peak and pulse average (I_{sppa}). The spatial peak pulse average intensity is defined as the mean intensity over the pulse duration at r_{max} and can be calculated as

$$I_{sppa} = \frac{\int p^2(t)dt}{\rho c PD} \tag{2.55}$$

where PD is the pulse duration. As defined by the American Institute of Ultrasound in Medicine (AIUM), PD is defined as 1.25 times the time interval between the 10% and 90% points of the pulse intensity.

A spatial and temporal average can also be found (I_{sata}), which is the average of the intensity over space and time. Finally, the spatial average pulse average intensity can be found (I_{sapa}) by calculating the average intensity over the area and over the pulse duration.

Chapter 3

The Rectangular Cymbal

To improve the portable ultrasound treatment system, a new cymbal transducer was used with a rectangular geometry. A more efficient transducer would benefit both insulin delivery and glucose sensing systems. The new rectangular transducer is described in this chapter along with construction methods and finally its electrical characteristics and a method of impedance matching the device to the signal source.

3.1 Rectangular Advantages

Before computer analysis or efficiency measurements, we can obtain a general understanding of how a rectangular cymbal geometry will improve the array. An improved packing geometry within the array and closer resonance frequencies of the flexural motion of the cap and displacement of the ceramic show that moving to a rectangular geometry is a good approach.

3.1.1 Geometry

In the previous circular arrays, an $n \times n$ array was used. Specifically, 2x2 and 3x3 arrays have been constructed and tested as described in Section 1.2.2. Consider the 3x3 array geometry shown in Figure 3.1. The array area is d^2 and the transducer area is $\frac{\pi}{4}d^2$. In general, for any $n \times n$ array, the transducer area for a circular geometry will be lower by a factor of $\frac{\pi}{4}$. Using a rectangular geometry allows us to have the freedom to use all of the array area to radiate acoustic energy.

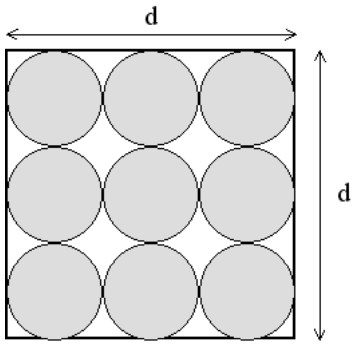

Figure 3.1: Diagram of using a circular cymbal geometry in a 3x3 array

3.1.2 Resonance Frequencies

Section 2.3.2.1 described the method for obtaining the first resonance frequency of a 3-1 PZT bar. We can see that the ceramic modes for bars with lengths near 50 mm fall close to 30 kHz. Radial modes of the circular ceramic satisfy a transcendental equation of the form

$$J_1(\eta) = 1 - \sigma^p \tag{3.1}$$

where J_1 is the Bessel function of the first kind of first order, η is an argument proportional to the frequency, and $\sigma^p = -s_{12}^E/s_{11}^E$ [17]. The first root of Equation 3.1 places the first resonance frequency of a circular ceramic similar in size to the ones used in previous research near 100 kHz. The flexural mode of the cap in a circular cymbal is close to 20 kHz. This shows that when the cap is vibrating at its resonance frequency, the ceramic is not and the displacement of the PZT is therefore not exhibiting maximum displacement. If we can close the gap between the two resonance frequencies, we can obtain a large displacement of the ceramic and of the cap simultaneously, giving a more efficient device. Using a rectangular geometry for the ceramic as previously analyzed allows us to bring the first resonance frequency of the PZT closer to the cap resonance, improving the efficiency.

3.2 Finite Element Analysis

Before construction and testing of the new rectangular geometry it is helpful to model the transducer. Finite element analysis provides an accurate method of predicting the transducer performance. ATILA and GiD was used to create the model and finite element mesh. The rectangular cymbal had the dimensions shown in Table 3.1

Table 3.1: Dimensions of a single rectangular cymbal transducer

Section	Dimension	Size (mm)
Ceramic	length	50.8
	width	12.7
	height	3
Cap	thickness	0.25
Cavity	length	46.8
	width	8.7
	height	0.6

Because of the symmetry of the transducer, only a $1/8^{th}$ section needed to be modeled. This reduced computer calculation time. The 3-D model is shown in Figure 3.2. A full description of the process can be found in Appendix B.

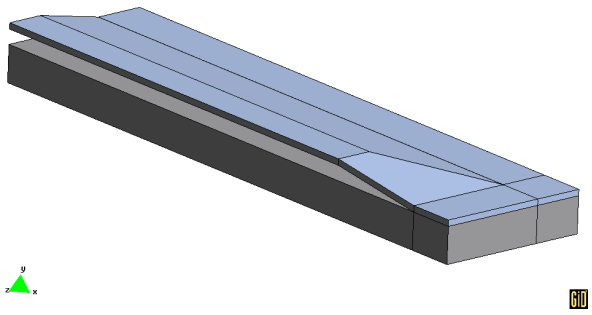

Figure 3.2: A 1/8th three dimensional model of the rectangular cymbal transducer

We can then allow GiD to automatically create a mesh for us. However, because the trans-

ducer is made of quadrilateral segments we can specify our own structured mesh composed of quadrilateral elements. This helps cut down on calculation time. The mesh created by GiD after specifying a structured mesh is shown in Figure 3.3.

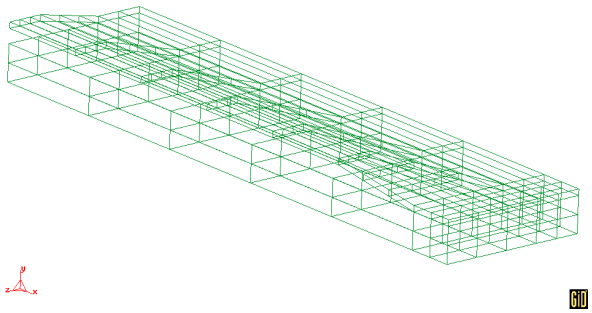

Figure 3.3: Mesh created by GiD after specifying a structured mesh of quadrilateral elements

We would like to operate the transducers at resonance so we first find a prediction for the admittance of the single element rectangular cymbal in air. Figure 3.4 shows the predicted admittance magnitude and phase of a single element rectangular cymbal transducer in air from 10 to 100 kHz. The predicted resonance occurs at 34 kHz, very close to the value calculated for a ceramic of the same dimensions using the method described in Section 2.3.2.1. Resonance frequencies will vary slightly for each device but we can be confident that they lie in the vicinity of 30 kHz. An admittance measurement can be made to determine the exact resonance frequency of each individual transducer or of an array.

The analysis provided by ATILA can also help to visualize the transducer displacement. As an example, Figure 3.5 shows a color contour of the axial displacement of the transducer caps at 10 kHz. We can see that at this frequency, the maximum displacement of the caps is in the center and that the cap moves up and down in the y direction in its first mode. By comparison, the magnitude of the displacement of the caps at resonance, or 34 kHz, is shown in Figure 3.6. Here the maximum displacement of the caps occurs at the ends and at the center of the caps simultaneously. Higher order modes of the cap are excited at resonance. We would expect that this difference from the circular cymbals creates a different intensity profile in the nearfield. In particular, we would expect that the nearfield

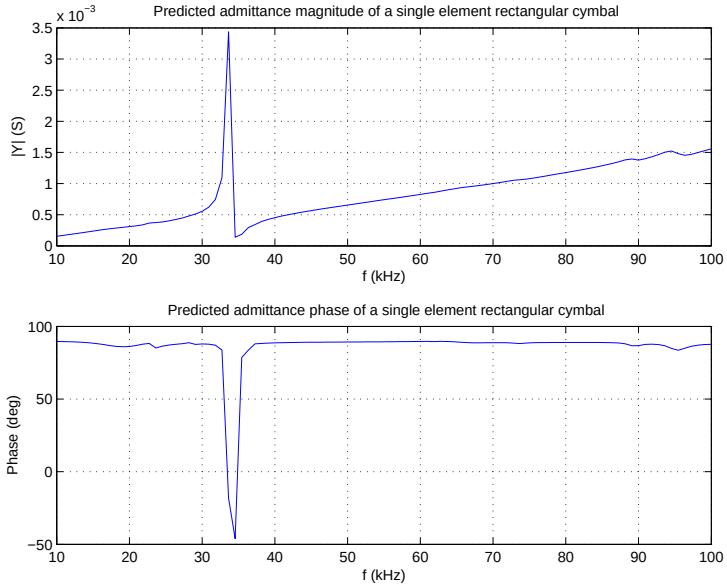

Figure 3.4: Predicted admittance magnitude and phase of a single element rectangular cymbal in air from 10 to 100 kHz

is characterized by more than one intensity peak on a plane in front of the transducer, giving a larger spatial average intensity. This does in fact occur and the measurements and implications are discussed in Section 4.1.

3.3 Transducer Construction

Construction of the rectangular cymbal transducers is done by hand. It is important to note that symmetry when fabricating the transducers is crucial to the performance of the device. Total construction time for one 3x1 array is approximately one week including time for transducer building and drying and curing time for the epoxy and polyurethane.

Rectangular Navy Type I 402 ceramics were ordered from Piezokinetics® poled in the thickness direction to use in the 3-1 bar configuration. The ceramics have a thin oxidized silver layer on the electrode surfaces that can be softly sanded away and cleaned with alcohol. The sanding also helps roughen the surface for when the epoxy is applied.

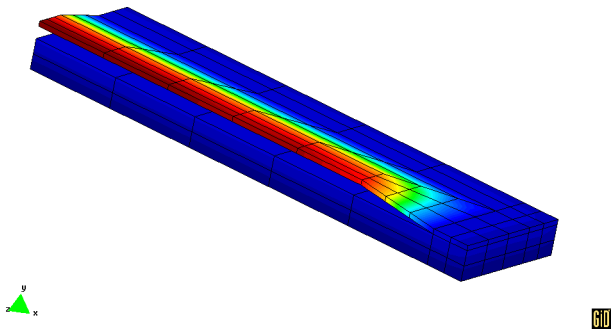

Figure 3.5: Contour plot of the axial displacement of the rectangular cymbal caps at 10 kHz

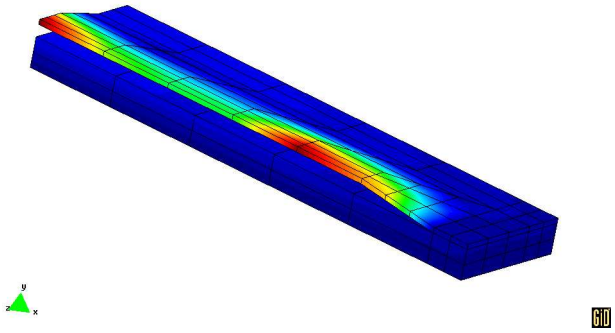

Figure 3.6: Contour plot of the axial displacement of the rectangular cymbal caps at 34 kHz

The titanium caps are made from titanium sheets obtained from Alfa Aesar with a 0.25 mm thickness. The titanium is cut into strips the same width and length as the rectangular ceramic. If the dimensions of the titanium strips are slightly longer in either dimension the edges can be sanded down. It is preferable to have slightly shorter cap dimensions than to have excess titanium over the edges of the ceramic.

The cap is shaped by pressing the cap using a shaping die. One cap is placed in the shaping die and pressed at 60 kpsi. To create a more symmetrical cap, the cap and the press are rotated and the procedure is repeated for a total of four presses per cap. Cap heights are

then measured at the center of the cap using a Starrett dial gauge. For symmetry, caps with the closest cap heights are paired together. Finally, the section of the caps that will be in contact with the ceramic are lightly sanded and cleaned with alcohol for a better bond.

The caps are bonded to the ceramics using Emerson-Cuming Eccobond 45 LV epoxy base and 15 LV catalyst in a 3:1 ratio. The epoxy is carefully spread on the edge of the ceramic by hand. The caps are then placed on the ceramic and clips are placed along the edges of the transducer to ensure a better seal. A one day drying time at room temperature is sufficient before testing and potting the transducer.

Arrays can be made by electrically connecting the transducers and potting them in a polyurethane. A conductive adhesive is used to connect the transducers in parallel and this is left to dry overnight to ensure a proper electrical connection. A two part polyurethane with a 90A shore hardness is mixed and is degassed. The liquid polyurethane is carefully poured on the array to minimize air pockets. Once the transducers are submerged in the liquid polyurethane, the array is left for three days to fully cure. Once cured, the array is ready to test and use. Figure 3.7 shows a single rectangular cymbal transducer and Figure 3.8 shows a 3x1 rectangular potted array compared to a 3x3 circular potted array.

Figure 3.7: A single element rectangular cymbal transducer

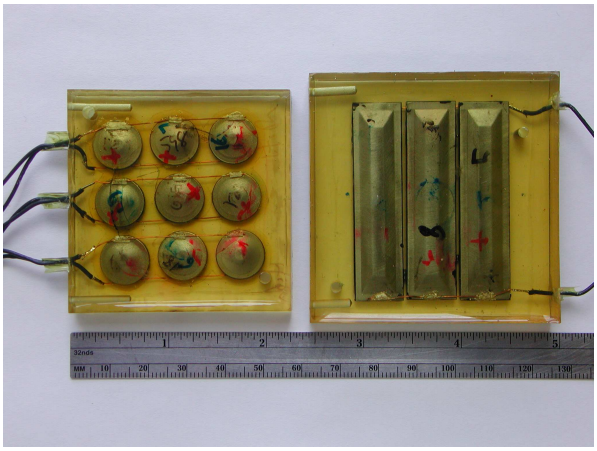

Figure 3.8: Size comparison of 3x3 circular and 3x1 rectangular cymbal transducer arrays

3.4 Electrical Characteristics

Once the transducer has been built, the admittance is measured to determine the resonance frequency of the device. As previously discussed, the resonance frequency of the device will be in the vicinity of 30 kHz and the admittance should describe a capacitive device away from the resonance frequency. The measured admittance magnitude and phase of one rectangular cymbal transducer in air is shown in Figure 3.9. The resonance of this particular rectangular cymbal is 33 kHz. Also plotted in Figure 3.9 is the ATILA predicted admittance and phase. Measured and predicted values agree.

We can also pot a single rectangular element, place it underwater and measure the admittance of one transducer underwater which includes the effects of mass loading. The measured underwater admittance magnitude and phase of a single element is shown in Figure 3.10. The resonance frequency of this transducer is 31 kHz underwater. The decrease in admittance magnitude is due to the mass loading of the transducer by the water as described in Section 2.3.2.2.

In Section 2.3.2.2 an equivalent circuit model was described for a transducer at or near resonance. Ignoring R_e we obtain an equivalent circuit in air shown in Figure 3.11. The resonance frequency of the transducer is governed by the series resonance of the mechanical

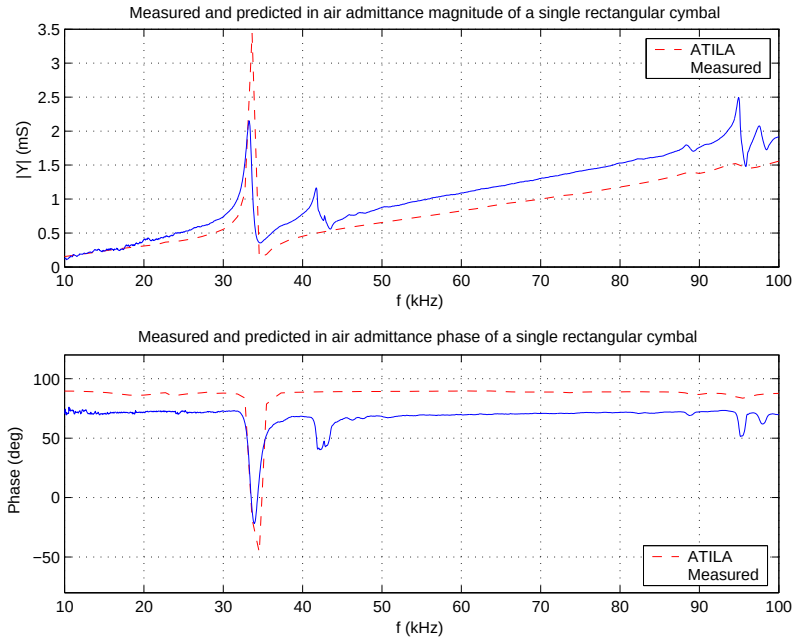

Figure 3.9: Measured and ATILA predicted admittance magnitude and phase of one rectangular cymbal transducer in air

components L_m and C_m. The resonance frequency for such a system can be calculated as

$$f = \frac{1}{2\pi\sqrt{L_m C_m}} \tag{3.2}$$

Using the values for L_m and C_m shown in Figure 3.11 we obtain a resonance frequency of 33.3 kHz. This shows that our circuit model accurately predicts the transducer at resonance.

For the underwater rectangular transducer, the equivalent circuit remains the same but a radiation resistance R_r and radiation reactance that can be modeled as an inductance L_r are added. Thus, the series resonance of the circuit is governed by C_m and $L_m + L_r$, effectively decreasing the resonance frequency.

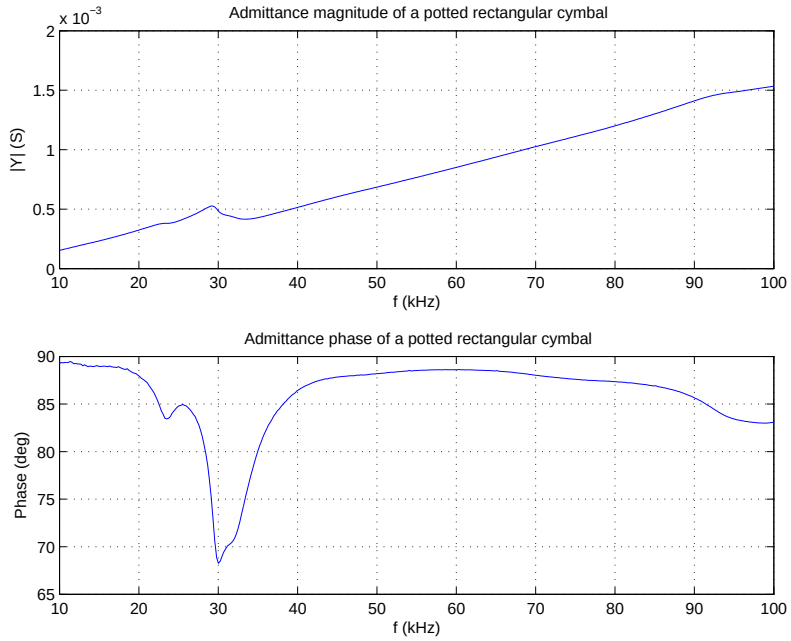

Figure 3.10: Measured underwater admittance magnitude and phase of one rectangular cymbal transducer

3.5 Impedance Matching

As shown in Section 2.3.2.1, the cymbal transducer acts primarily like a capacitor. The complex input electrical impedance of the transducers can be expressed as

$$Z = R + jX \tag{3.3}$$

where R is the resistance and X is the reactance. For a source with output impedance Z_o, maximum power transfer occurs when the input impedance of the load matches the output impedance of the source.

In our lab tests, the transducers are connected to amplifiers that have a 50 Ω output impedance. To obtain maximum power transfer to the transducer we would like to design

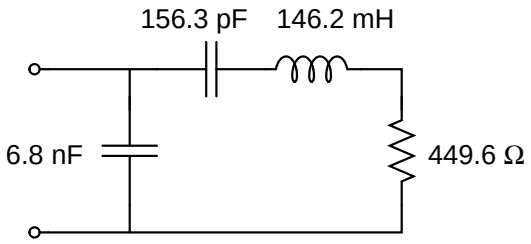

Figure 3.11: Equivalent circuit values for one rectangular cymbal transducer

and build a matching circuit that when connected to the transducer allows the amplifier to see a 50 Ω input impedance. For impedance matching to the amplifier with a 50 Ω output impedance we use the circuit shown in Figure 3.12 known as a pi type circuit.

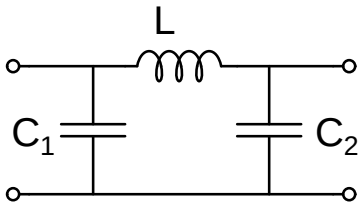

Figure 3.12: Low pass pi type impedance matching circuit used to match transducer to the source

To find the necessary values for C_1, C_2, and L we must first know what that impedance is of the transducer at the operating frequency. As one example, the resistance and reactance of one 3x1 rectangular array is shown in Figure 3.13.

We can then use a Smith chart to add admittance and impedance to the array to obtain an impedance equal to that of the source. Component values can be found knowing that the impedances of a capacitor and an inductor are $1/j\omega C$ and $j\omega L$ respectively. Note that there are many possible solutions to match impedances and a desired bandwidth over which the match will work should be known to complete the analysis.

A detailed analysis of how to match using the Smith chart is beyond the scope of this work. However, because the final system will be run off of portable electronics, it is likely that

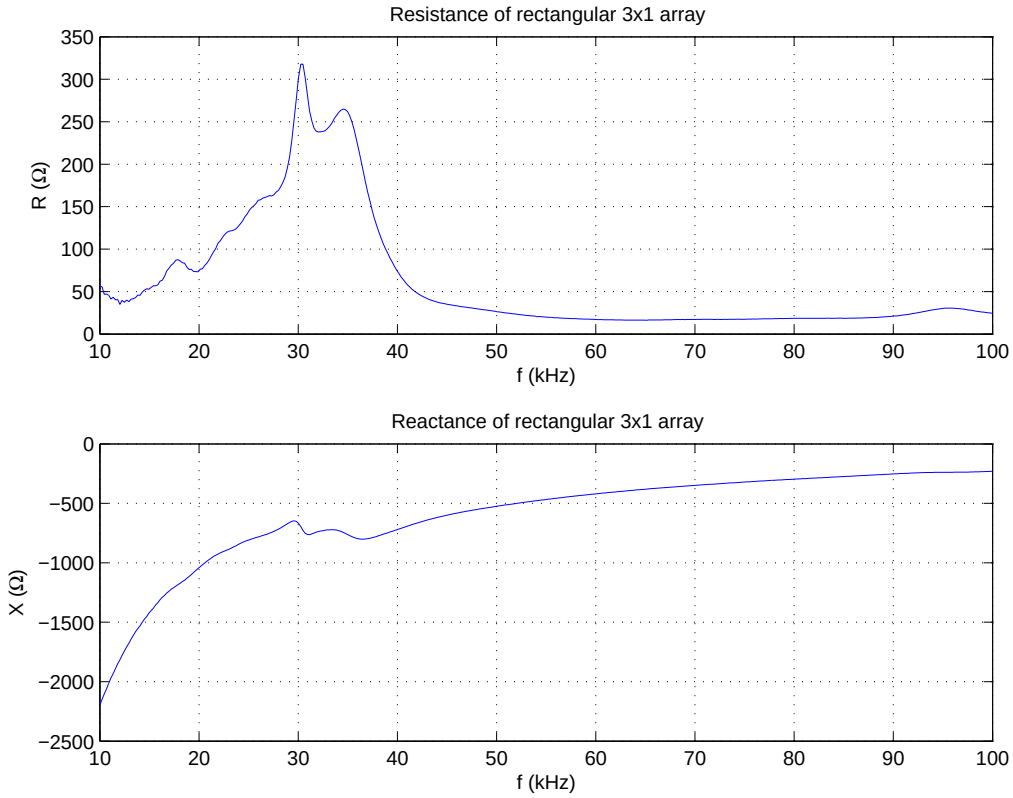

Figure 3.13: Resistance and reactance of one 3x1 rectangular cymbal array

the output impedance of the source will not be 50 Ω. For this reason, a MATLAB script has been written to calculate the necessary values for the pi matching circuit given the transducer's input impedance, the source output impedance, and the desired bandwidth. The code can be found in Appendix A.

If we look at the impedance of the transducer array we notice that the array has negative reactance, indicating that the system is capacitive. If impedance matching is not of primary importance, we can also tune the transducer using an inductor. This is done by using a tuning inductor either in series or in parallel with the device. For parallel tuning, we obtain a circuit diagram for the device shown in Figure 3.14.

As described in Section 3.4, the resonance frequency of the array is determined by the series resonance frequency of L_m and C_m. To tune the transducer, we would like to have

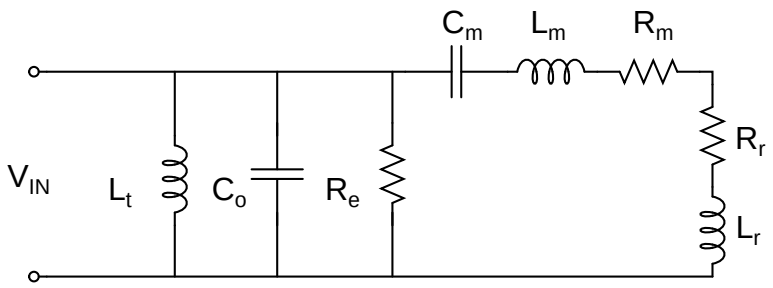

Figure 3.14: Circuit diagram for a parallel tuned transducer at resonance

two individual resonating circuits. The first is the mechanical circuit resonance governed by L_m and C_m and the second is the electrical resonance that will be governed by C_o and L_t. The clamped capacitance and resonance frequency of the transducer can be measured and we find that

$$L_t = \frac{1}{\omega_r^2 C_o} \tag{3.4}$$

where the resonance frequency $\omega_r = 2\pi f_r$. For the 3x1 rectangular arrays, C_o values are near 6 nF and resonance is close to 30 kHz, giving a tuning inductor value near 5 mH. Similar tuning can be achieved by placing the tuning inductor in series with the transducer and letting L_t and C_o resonate at the anti-resonance frequency, or the point of minimum admittance.

Chapter 4

Rectangular Cymbal Performance

The performance of the new rectangular devices can be divided into two sections, the electrical and acoustical efficiency and the ability of the devices to permeabilize the skin. To improve the overall system performance, the new devices must improve the efficiency in either area with no decreased efficiency in the other. The increased performance of the rectangular single element and 3x1 array are discussed here. Improvements made to the electrical efficiency are discussed first, followed by animal experiments showing better insulin delivery performance.

4.1 Measured Results

A description of the acoustic properties of the rectangular cymbals is given in this section. Far field measurements are shown and are then followed by near field exposimetry data. Far field measurements are shown in a small frequency band of interest and exposimetry measurements are shown at the operating frequency of the device. Measured results for array data are compared to the circular 3x3 cymbal array.

4.1.1 Single Element

Although the transducers are used in arrays to achieve high enough acoustic intensities, it can be useful to see the individual transducer's performance. Figure 4.1 shows the measured TVR of a single rectangular cymbal transducer. The frequency band of interest is from 15 kHz to 35 kHz. We would like to operate the device close to 20 kHz since it has been shown

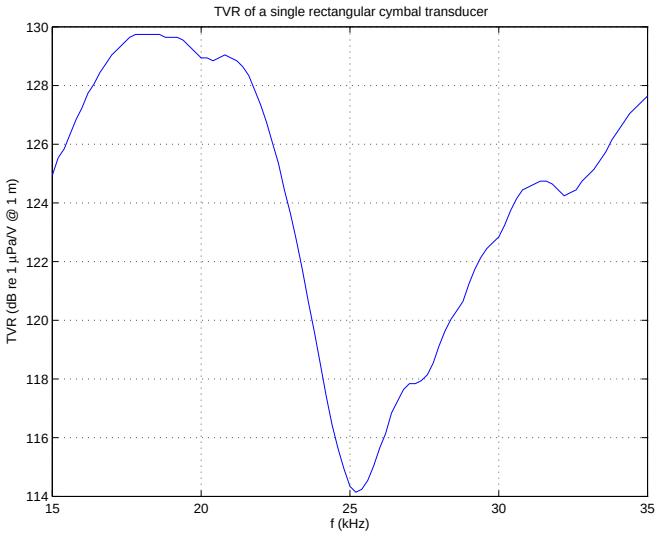

Figure 4.1: TVR of a single rectangular cymbal transducer

that sonophoresis works best at lower ultrasound frequencies.

At 25 kHz we see a large dip in the TVR of the single rectangular element. This dip is seen in transducers that are not symmetrical enough. When this occurs, asymmetrical modes can occur in which the caps are vibrating out of phase, essentially radiating like a dipole. Radiation from the transducer is severely limited when the caps operate in this way. For our purposes, we are operating at single frequencies and these asymmetrical modes are of minimal consequence. However, if we wanted to use a certain frequency band we would need to improve the manufacturing process to eliminate the asymmetries that can occur.

For the single element rectangular transducer, the VA/Watt ratio is shown in Figure 4.2. We can see that the drop in performance near 25 kHz is also a point of minimal electrical efficiency. In addition, the device overall is not an efficient transducer. This is the result of the cymbal being capacitive and the transducer is essentially an electrical energy storage device. This can be overcome by either impedance matching or tuning as described in Section 3.5. The following section will describe the untuned as well as the tuned efficiency of the rectangular array in comparison to the circular cymbal array.

In the near field at resonance, the rectangular cymbal transducer excites higher order modes

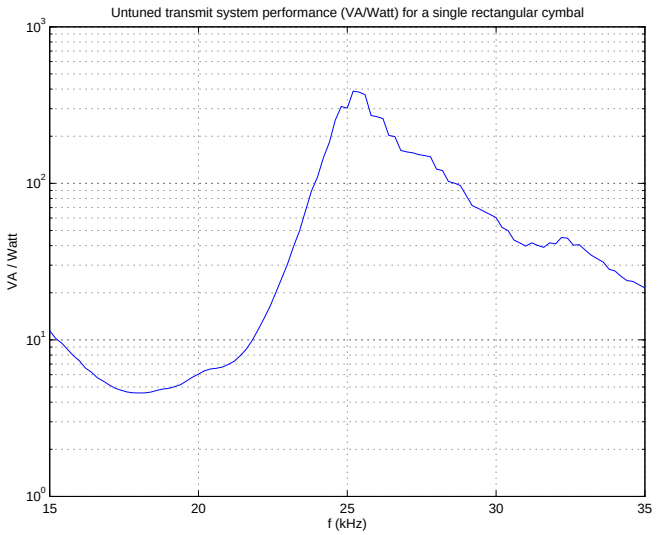

Figure 4.2: Untuned VA/Watt ratio of a single rectangular cymbal transducer

of the caps as described in Section 3.2. The result is a spatial intensity profile shown in Figure 4.3. An ideal spatial profile would be flat. This way, any spatial and temporal intensity specification could be given and that intensity would be delivered to all points on the skin. At resonance, the rectangular cymbal exhibits a three peak intensity profile on a plane 1 mm away from the transducer face. Spatially, this is an improvement over the circular single element and circular arrays, which have a single peak profile. Observing such a profile for the rectangular cymbal in the near field shows a potential improvement in insulin delivery when placing the transducers in a 3x1 array.

4.1.2 3x1 Array

For animal tests as well as with human patients in the future, cymbal arrays will be used. Using arrays enables us to produce larger acoustic intensities. Previous work has used circular cymbal arrays in the 3x3 configuration and here we will compare the 3x1 rectangular array to the 3x3 circular array.

Figure 4.4 shows the TVR of both the 3x1 rectangular array and the 3x3 circular array. The

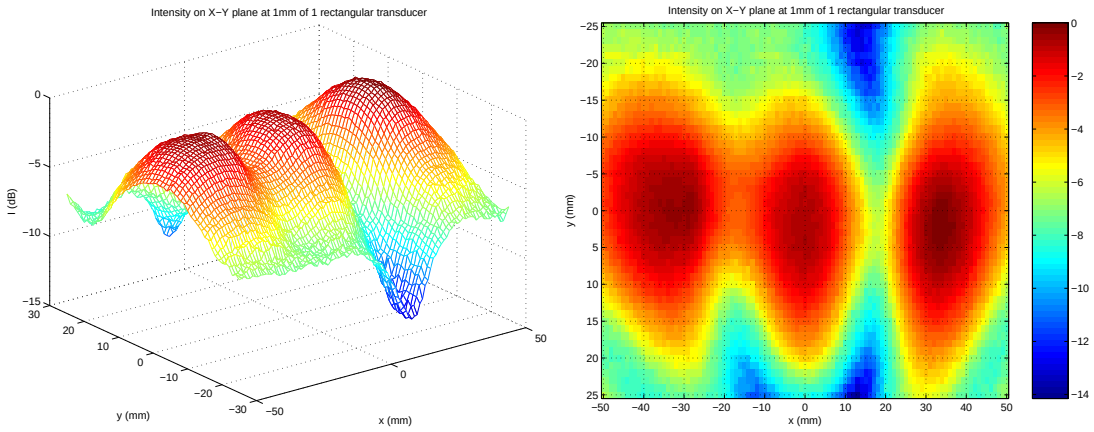

Figure 4.3: Normalized intensity exposimetry of a single rectangular cymbal in a plane 1 mm from the face of the transducer

rectangular array shows an improvement in far field performance over the circular array. There are drops in the TVR in the rectangular array and these are due to asymmetries in the device caused by the construction process. If these manufacturing issues are corrected, the TVR would have improved across the frequency band. In addition, we will operate the rectangular arrays near 30 kHz and at this frequency the new transducers give a better TVR.

For the electrical efficiency, we can also see how the 3x1 rectangular arrays outperform the 3x3 circular arrays. Figure 4.5 shows the untuned VA/Watt ratio for the 3x1 rectangular and 3x3 circular cymbal arrays. We can see an increased electrical efficiency by using the 3x1 rectangular configuration. At the same frequencies where the TVR drops, we also see the VA/Watt ratio increasing significantly. This is to be expected since the acoustic power radiated by a transducer operating like a dipole is minimal.

For the untuned cases, the VA/Watt ratio is large. We would like to see greater efficiency in order to achieve a portable device. To decrease the effect of having a capacitive device we can tune the transducer at various frequencies. Figure 4.6 shows the VA/Watt ratio of 3x1 rectangular and 3x3 circular arrays when tuned near 23 kHz, the resonance frequency of the circular array.

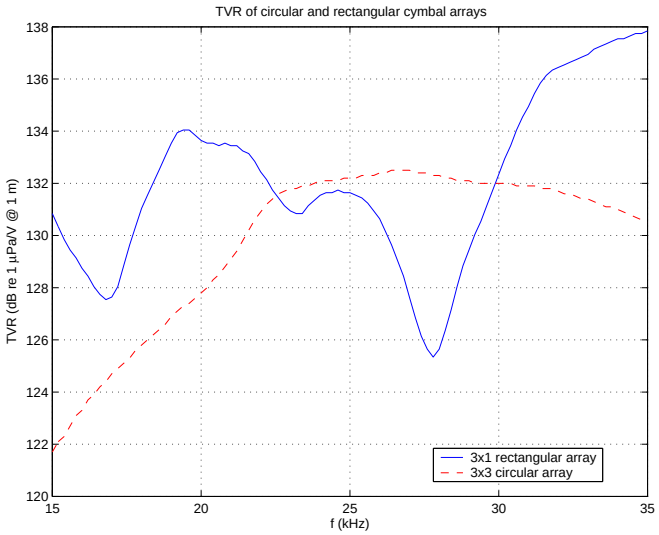

Figure 4.4: TVR comparison of a 3x1 rectangular and 3x3 circular array

When tuned, we can see a substantial improvement in the the VA/Watt ratio. The ratio at the tuned frequency drops near one and we can see that for single frequency operation it will be possible to use these transducer arrays in a portable device. At this frequency we notice that the rectangular cymbals are more efficient than the circular cymbals.

We can tune the devices to whatever frequency we like. As described earlier, the tuning frequency can be determined by the parallel resonance of the tuning inductor L_t and the clamped capacitance C_o. As an example, Figure 4.7 shows the VA/Watt ratio of 3x1 rectangular and 3x3 circular arrays near 32 kHz. Again the VA/Watt ratio drops near one and the rectangular cymbal array performs better than the circular array.

For far field performance we can see that by using the rectangular arrays we can achieve nearly double the electrical efficiency when using the VA/Watt efficiency measurement. In addition, the TVR of the rectangular and circular arrays indicate that the increased cap area of the rectangular cymbals help to radiate more acoustic energy.

In the near field we would like to see a nearly flat intensity profile in order to sonicate the area of skin evenly. As we saw in Figure C.12, repeated here as Figure 4.8, the spatial intensity profile of the 3x3 circular array has a single peak at the center of the transducer

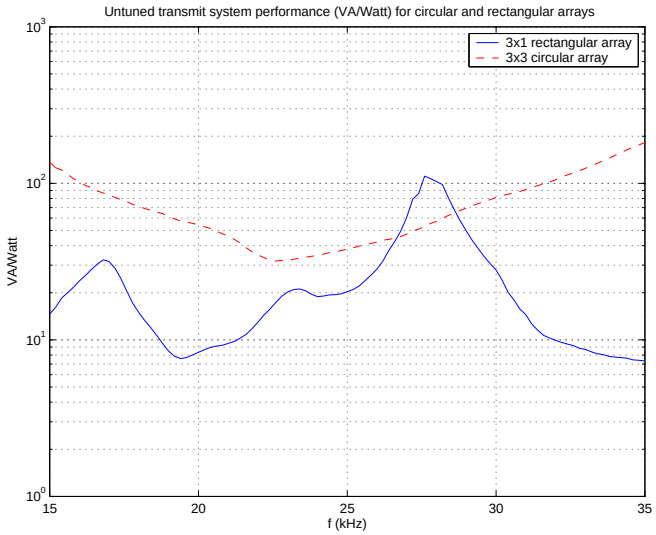

Figure 4.5: Untuned VA/Watt ratios of rectangular and circular cymbal arrays

and falls off as you move away from the center. Therefore, if you specify an intensity I_{sptp}, only a small portion of skin will be receiving that intensity while the rest will be sonicated at much lower level.

When exposimetry measurements are made for the 3x1 rectangular array at resonance, we see an intensity profile shown in Figure 4.9. Unlike the circular array, we see a three peak profile with the rectangular array. This profile is due to the higher order modes that are excited in the cap when operating at the ceramic resonance. The ceramic resonance frequency was decreased by changing the geometry and the increased ceramic length increased the cap cavity length, decreasing the cap's first resonant frequency. When operating near 30 kHz, the cap's ends and center move in phase, creating three distinct peaks in the intensity spatial profile.

As stated earlier, the ideal profile would be flat, describing even sonication of the skin. By moving to the rectangular arrays we have moved closer to those conditions. A specified I_{sptp} would give the same spatial peak intensity in the circular and rectangular arrays but a larger spatial average intensity is seen for the rectangular arrays. This leads us to believe that since the skin is being sonicated more evenly and at a higher spatial average intensity

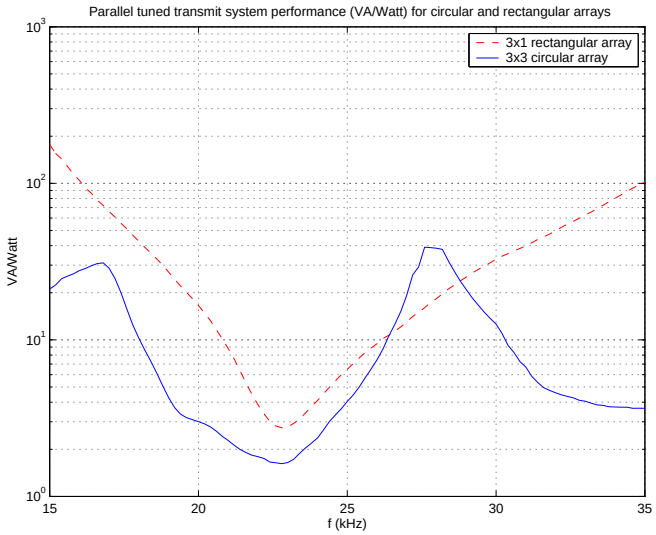

Figure 4.6: Parallel tuned VA/Watt ratios of rectangular and circular cymbal arrays near 23 kHz

that more insulin can be delivered in a shorter period of time. This is in fact true and the animal test results will be discussed in Section 4.2.2.

4.2 Animal Tests

In order to determine the effectiveness of the new rectangular arrays in ultrasonic transdermal insulin delivery, animal tests are performed. It is possible to have a transducer that is electrically efficient but does not improve the rate of insulin delivery. As we have seen, the rectangular cymbals are an improvement over the circular arrays in electrical efficiency. In addition, the rectangular arrays exhibit a larger spatial average intensity profile and the animal experiments performed in this work are to verify the hypothesis that the increased spatial average would increase the insulin delivery rate. All animal experiments are approved by The Pennsylvania State University's Institutional Animal Care and Use Committee (IACUC), protocol number 15262.

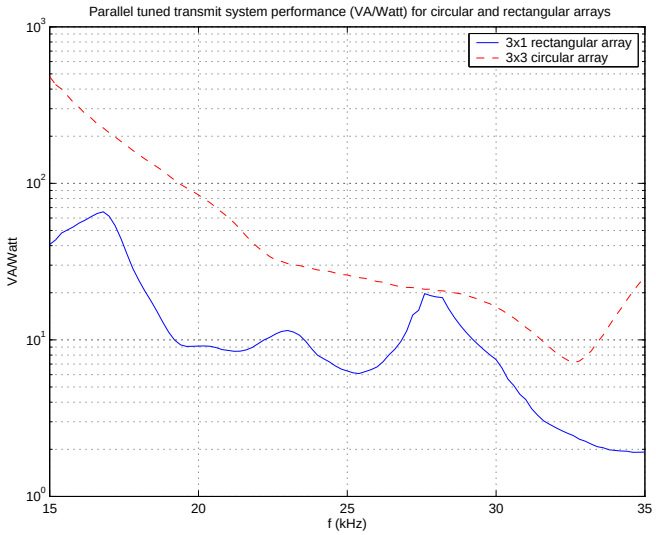

Figure 4.7: Parallel tuned VA/Watt ratios of rectangular and circular cymbal arrays near 32 kHz

4.2.1 Animal Test Procedure

The rabbits to be tested are first anesthetized. A combination of ketamine hydrochloride and sodium xylazine is used as an anesthetic. Specific doses vary by animal weight, with ketamine and xylazine being delivered in the doses 40 mg/kg and 10 mg/kg respectively. Using xylazine induces hyperglycemia in the the rabbits and blood glucose levels rise to nearly triple normal levels. This hyperglycemic state is steady for nearly 10 to 12 hours.

Once the animal is under anesthetic, the area to be treated is shaved. This is usually the thigh or abdomen area. For these experiments the thigh area was used. A small plexiglass stand off is made for the transducer in order to have a small reservoir of insulin between the transducer and the rabbit's skin. Figure 4.10 shows how the transducer arrays are placed on the rabbit's skin in preparation for testing.

Humulin R insulin with a 50 U/mL concentration is placed in the reservoir by way of a small hole drilled through the polyurethane of the array. A needle is used to carefully fill the space with insulin and minimize air pockets. Once the device is in place, blood is drawn from the ear to take an initial blood glucose level reading using an Accu-Chek glucose monitor.

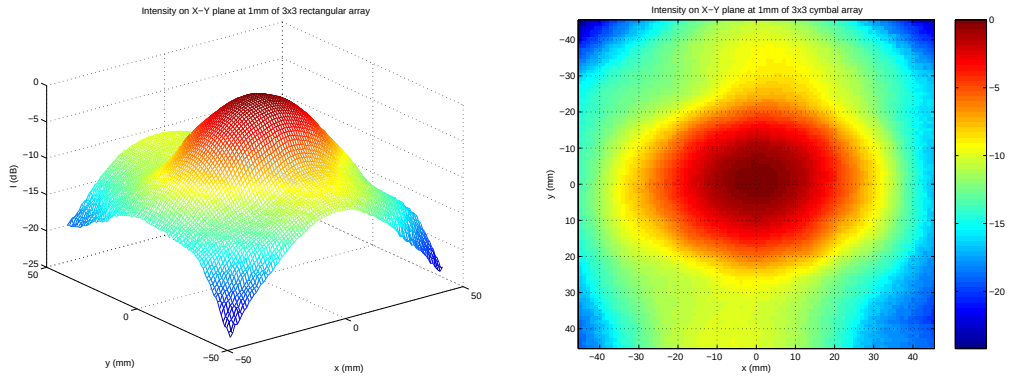

Figure 4.8: Normalized intensity exposimetry of a 3x3 circular array in a plane 1 mm from the face of the transducer

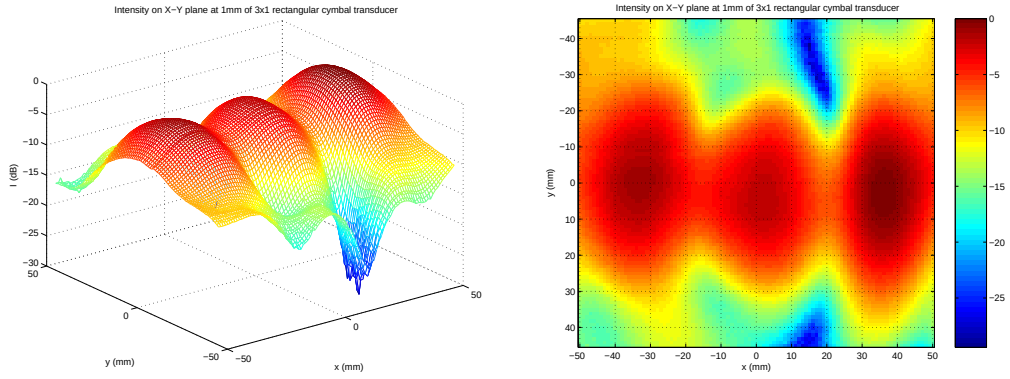

Figure 4.9: Normalized intensity exposimetry of a 3x1 rectangular array in a plane 1 mm from the face of the transducer

Measurements from the Accu-Chek systems vary slightly so two monitors are used and the results are averaged.

After the initial check of the blood glucose level, the ultrasound is turned on at $I_{sptp} = 50$ mW/cm^2 at the first resonance frequency of the transducer (∼30kHz) and is pulsed with a pulse period of 1 second and a 20 % duty cycle. A blood glucose measurement is made every 15 minutes by an ear prick blood draw and the Accu-Chek systems. The ultrasound is turned off after 60 minutes but the transducer and the insulin is left on the skin. It has been previously shown that the skin can remain permeable even after the ultrasound exposure and for this reason once the ultrasound is turned off, two more measurements at

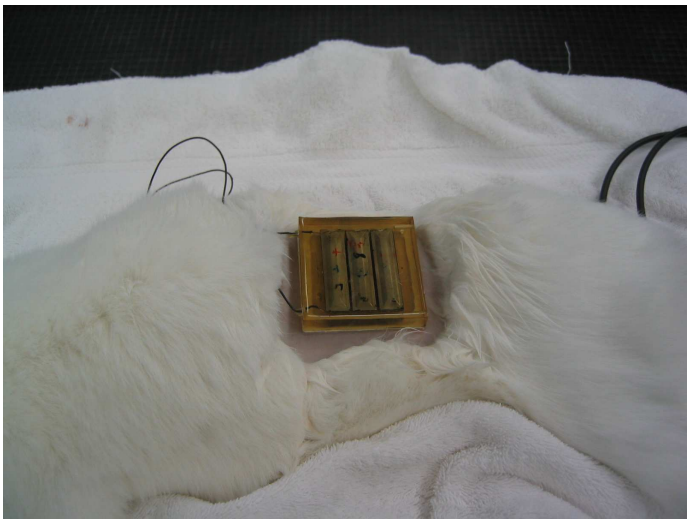

Figure 4.10: Placement of the rectangular 3x3 array on shaved area of rabbit thigh

75 and at 90 minutes are made. The result is a 90 minute test of which the first 60 minutes includes a pulsed ultrasound exposure at the spatial and temporal peak intensity specified. Seven data points are obtained and the levels are normalized to show changes in overall blood glucose levels in the rabbits during the 90 minute tests. Once testing is over, the array is removed and the rabbit is monitored until it regains consciousness.

4.2.2 Test Results

To present the results, the glucose levels measured are normalized to the first reading. Therefore, results are shown as a change in glucose level as opposed to actual glucose level measured. Figure 4.11 shows the normalized change in glucose levels in 5 kg rabbits using the 3x3 circular array and the new 3x1 rectangular array.

After 30 minutes, the two arrays perform similarly. However after 60 minutes, and after 90 minutes, the rabbit treated using the 3x1 rectangular array has glucose level drops nearly double those with the 3x3 circular array. These tests verify the increased effectiveness of the 3x1 rectangular arrays in making the skin permeable to allow diffusion of insulin across the skin.

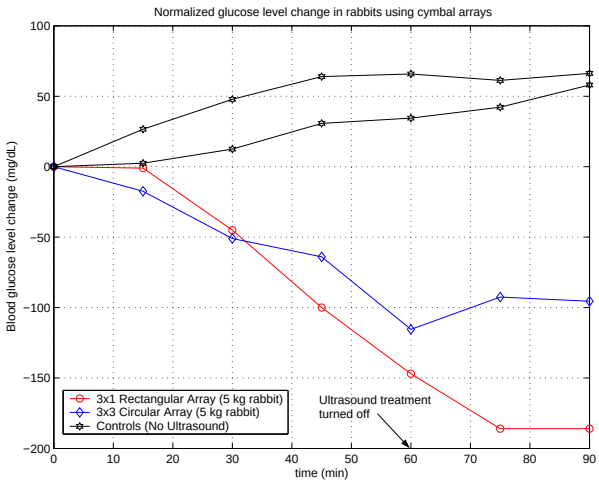

Figure 4.11: Normalized change in glucose levels in 5 kg rabbits after ultrasonic insulin delivery experiments

In addition to the insulin experiments, histological studies are performed to determine the bioeffects of the ultrasound treatment on the skin. Figure 4.12 shows an example of a histology study performed. The study shows no damage to hair follicles, no hemorrhage,

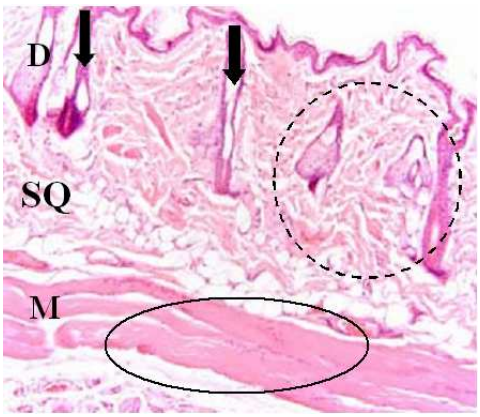

Figure 4.12: Histology study performed to show no damaging bioeffects due to ultrasound exposure during animal experiments

and healthy connective tissue. We can be confident that at the intensities used in these tests there are no damaging bioeffects. Larger intensities closer to 300 mW/cm^2 can cause damage to the skin including reddening and burning. However, we are in a safe operating

range and although we have increased the spatial average intensity in order to increase the insulin delivery rate, there has been no increase in spatial and temporal peak intensity.

Chapter 5

Conclusion

This work has evaluated the use of a new rectangular cymbal geometry for use in a portable ultrasonic transdermal insulin delivery system. It was determined that the rectangular geometry would provide more radiating area and an increased efficiency that would be important for a final portable and lightweight device.

Rectangular cymbal transducers were modeled using the finite element analysis program ATILA. The devices were then constructed and their properties were measured in air and in water. Arrays in the 3x1 configuration were constructed and tested in the far field and in the near field. Comparisons were made between the previously used 3x3 circular arrays and the new 3x1 rectangular arrays of similar size. Animal tests were also performed using the 3x3 circular and 3x1 rectangular array to compare the effect the new devices have on the rate of insulin delivery. It is concluded that the new rectangular cymbals are twice as efficient electrically when tuned to a single frequency. In addition, the rate of insulin delivery using the new rectangular devices is nearly double that of the circular arrays over one 90 minute test that included a 60 minute sonication. More animal tests would be needed to determine the variation between tests but the single test shows that the increase in spatial average intensity improves the insulin delivery rate.

5.1 Evaluation of Using Rectangular Cymbals

The new rectangular cymbals in the 3x1 configuration have shown improved performance over the 3x3 circular array. There was no significant increase in size to obtain this increased efficiency and increased rate of insulin delivery. In terms of cost, in mass quantities the two

arrays are similar in cost. Finally, if the circular cymbals are used, it would be difficult to increase the rate of insulin delivery at the same spatial and temporal peak since the near field intensity for a 2x2, 3x3, or nxn array is a single peak profile that falls off quickly. For these reasons, using the new rectangular cymbals will prove to be a step forward in the development of a portable insulin delivery device.

5.2 Suggestions for Future Work

In the rectangular cymbal, the cap of the transducer is attached to the ceramic in the length direction. One possibility is to only attach the cymbal at the ends of the bar and leave the length edges open [18]. This would not be an optimal design for underwater applications where the transducers may experience high static pressures but for our insulin delivery device this is not an issue. By not attaching the lengthwise edges, we can achieve a larger radiating area for the same size cymbal. A preliminary ATILA model is shown in Figure 5.1. Completion of the model and construction of the device to determine the new near

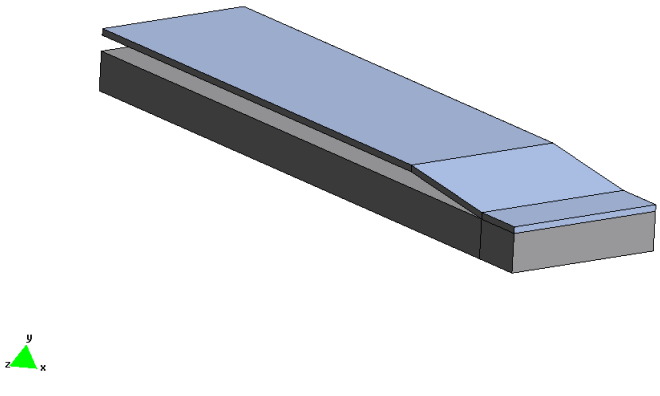

Figure 5.1: A model of a rectangular cymbal with no cap bonding along the length of the ceramic bar

field intensity spatial profile could show that this different rectangular design is an improved transducer for our drug delivery application.

As far as the portable insulin delivery device is concerned, work has been limited to the use of a single frequency. A 90% or more efficiency can be achieved if only a single frequency is used by tuning the transducers. Even though the frequency band of the rectangular cymbals is larger than the circular cymbals, the electrical efficiency away from the tuning frequency is poor. Work to improve the working bandwidth of the transducers would be useful in the exploration of using a multiple frequency skin sonication. Multiple frequencies would excite different sized pores and bubbles, perhaps increasing the insulin delivery rate further.

Improvements in the potting material can also be made. Currently, a 90A shore hardness is used, resulting in a stiff device. A material was found in this work with a 35A shore hardness and with the correct acoustic properties, but the material would have been toxic and therefore unacceptable for this project. A softer material with flexibility that still has a similar characteristic acoustic impedance to water would be valuable in making a portable patch.

Finally, larger animal tests are imperative before testing on humans. Glucose levels can be varied in small animals rapidly and insulin can be delivered to them at therapeutic levels using the current arrays. However, the same array will not deliver insulin at the therapeutic rates required for a 200 lb diabetic patient. It will be necessary to perform large animal experiments in which the intensity and the number of transducer elements are varied to determine the proper configuration for human patients.

Appendix A

MATLAB Code

```
%%%%%%%%%%%%%%%%%%%%%%%%%%%%%%%%%%%%%%%%%%%%%%%%%%%%%%%%%%%%%%%%%%%%%%%%
%This program plots the displacement of a rectangular ceramic given various
%user specified piezoelectric constants in the 3-1 mode.  There is a
%graphical interface to make it easier to input the constants.  The first
%resonance %frequency of the transducer is calculated as well so that
%displacement at resonance can be compared.
%%%%%%%%%%%%%%%%%%%%%%%%%%%%%%%%%%%%%%%%%%%%%%%%%%%%%%%%%%%%%%%%%%%%%%%%

function varargout = SolutionsGUI2(varargin)
% SOLUTIONSGUI2 M-file for SolutionsGUI2.fig
% SOLUTIONSGUI2, by itself, creates a new SOLUTIONSGUI2 or raises the
%existing singleton*.
%
% H = SOLUTIONSGUI2 returns the handle to a new SOLUTIONSGUI2 or the handle
% to the existing singleton*.
%
% SOLUTIONSGUI2('CALLBACK',hObject,eventData,handles,...) calls the local
% function named CALLBACK in SOLUTIONSGUI2.M with the given input arguments.
%
%SOLUTIONSGUI2('Property','Value',...) creates a new SOLUTIONSGUI2 or raises
%the existing singleton*.  Starting from the left, property value pairs are
%applied to the GUI before SolutionsGUI2_OpeningFunction gets called.  An
%unrecognized property name or invalid value makes property application
%stop.  All inputs are passed to SolutionsGUI2_OpeningFcn via varargin.
%
%    *See GUI Options on GUIDE's Tools menu.  Choose "GUI allows only one
%    instance to run (singleton)".
%
% See also: GUIDE, GUIDATA, GUIHANDLES

% Edit the above text to modify the response to help SolutionsGUI2

% Last Modified by GUIDE v2.5 07-Oct-2004 17:29:00
```

```
% Begin initialization code - DO NOT EDIT
gui_Singleton = 1; gui_State = struct('gui_Name',       mfilename,
...
                   'gui_Singleton',  gui_Singleton, ...
                   'gui_OpeningFcn', @SolutionsGUI2_OpeningFcn, ...
                   'gui_OutputFcn',  @SolutionsGUI2_OutputFcn, ...
                   'gui_LayoutFcn',  [] , ...
                   'gui_Callback',   []);
if nargin & isstr(varargin{1})
    gui_State.gui_Callback = str2func(varargin{1});
end

if nargout
    [varargout{1:nargout}] = gui_mainfcn(gui_State, varargin{:});
else
    gui_mainfcn(gui_State, varargin{:});
end
% End initialization code - DO NOT EDIT


% --- Executes just before SolutionsGUI2 is made visible.
function SolutionsGUI2_OpeningFcn(hObject, eventdata, handles,
varargin)
% This function has no output args, see OutputFcn.
% hObject    handle to figure
% eventdata  reserved - to be defined in a future version of MATLAB
% handles    structure with handles and user data (see GUIDATA)
% varargin   command line arguments to SolutionsGUI2 (see VARARGIN)

% Choose default command line output for SolutionsGUI2
handles.output = hObject;

% Update handles structure
guidata(hObject, handles);

% UIWAIT makes SolutionsGUI2 wait for user response (see UIRESUME)
% uiwait(handles.figure1);


% --- Outputs from this function are returned to the command line.
```

```
function varargout = SolutionsGUI2_OutputFcn(hObject, eventdata,
handles)
% varargout  cell array for returning output args (see VARARGOUT);
% hObject    handle to figure
% eventdata  reserved - to be defined in a future version of MATLAB
% handles    structure with handles and user data (see GUIDATA)

% Get default command line output from handles structure
varargout{1} = handles.output;


% --- Executes during object creation, after setting all properties.
function edit1_CreateFcn(hObject, eventdata, handles)
% hObject    handle to edit1 (see GCBO)
% eventdata  reserved - to be defined in a future version of MATLAB
% handles    empty - handles not created until after all CreateFcns
% called

% Hint: edit controls usually have a white background on Windows.
%       See ISPC and COMPUTER.
if ispc
    set(hObject,'BackgroundColor','white');
else
    set(hObject,'BackgroundColor',
    get(0,'defaultUicontrolBackgroundColor'));
end



function edit1_Callback(hObject, eventdata, handles)
% hObject    handle to edit1 (see GCBO)
% eventdata  reserved - to be defined in a future version of MATLAB
% handles    structure with handles and user data (see GUIDATA)

% Hints: get(hObject,'String') returns contents of edit1 as text
% str2double(get(hObject,'String')) returns contents of edit1 as a double
global l l=str2double(get(hObject,'String'));

% --- Executes during object creation, after setting all properties.
function edit2_CreateFcn(hObject, eventdata, handles)
% hObject    handle to edit2 (see GCBO)
```

```
% eventdata  reserved - to be defined in a future version of MATLAB
% handles    empty - handles not created until after all CreateFcns
% called

% Hint: edit controls usually have a white background on Windows.
%       See ISPC and COMPUTER.
if ispc
    set(hObject,'BackgroundColor','white');
else
    set(hObject,'BackgroundColor',
    get(0,'defaultUicontrolBackgroundColor'));
end



function edit2_Callback(hObject, eventdata, handles)
% hObject    handle to edit2 (see GCBO)
% eventdata  reserved - to be defined in a future version of MATLAB
% handles    structure with handles and user data (see GUIDATA)

% Hints: get(hObject,'String') returns contents of edit2 as text
% str2double(get(hObject,'String')) returns contents of edit2 as a
% double
global w w=str2double(get(hObject,'String'));

% --- Executes during object creation, after setting all properties.
function edit3_CreateFcn(hObject, eventdata, handles)
% hObject    handle to edit3 (see GCBO)
% eventdata  reserved - to be defined in a future version of MATLAB
% handles    empty - handles not created until after all CreateFcns
% called

% Hint: edit controls usually have a white background on Windows.
%       See ISPC and COMPUTER.
if ispc
    set(hObject,'BackgroundColor','white');
else
    set(hObject,'BackgroundColor',
    get(0,'defaultUicontrolBackgroundColor'));
end
```

```
function edit3_Callback(hObject, eventdata, handles)
% hObject    handle to edit3 (see GCBO)
% eventdata  reserved - to be defined in a future version of MATLAB
% handles    structure with handles and user data (see GUIDATA)

% Hints: get(hObject,'String') returns contents of edit3 as text
% str2double(get(hObject,'String')) returns contents of edit3 as a
% double
global t t=str2double(get(hObject,'String'));

% --- Executes during object creation, after setting all properties.
function edit4_CreateFcn(hObject, eventdata, handles)
% hObject    handle to edit4 (see GCBO)
% eventdata  reserved - to be defined in a future version of MATLAB
% handles    empty - handles not created until after all CreateFcns
% called

% Hint: edit controls usually have a white background on Windows.
%       See ISPC and COMPUTER.
if ispc
    set(hObject,'BackgroundColor','white');
else
    set(hObject,'BackgroundColor',
    get(0,'defaultUicontrolBackgroundColor'));
end



function edit4_Callback(hObject, eventdata, handles)
% hObject    handle to edit4 (see GCBO)
% eventdata  reserved - to be defined in a future version of MATLAB
% handles    structure with handles and user data (see GUIDATA)

% Hints: get(hObject,'String') returns contents of edit4 as text
% str2double(get(hObject,'String')) returns contents of edit4 as a double
global d33 d33=str2double(get(hObject,'String'));

% --- Executes during object creation, after setting all properties.
function edit5_CreateFcn(hObject, eventdata, handles)
```

```
% hObject    handle to edit5 (see GCBO)
% eventdata  reserved - to be defined in a future version of MATLAB
% handles    empty - handles not created until after all CreateFcns
% called

% Hint: edit controls usually have a white background on Windows.
%       See ISPC and COMPUTER.
if ispc
    set(hObject,'BackgroundColor','white');
else
    set(hObject,'BackgroundColor',
    get(0,'defaultUicontrolBackgroundColor'));
end



function edit5_Callback(hObject, eventdata, handles)
% hObject    handle to edit5 (see GCBO)
% eventdata  reserved - to be defined in a future version of MATLAB
% handles    structure with handles and user data (see GUIDATA)

% Hints: get(hObject,'String') returns contents of edit5 as text
% str2double(get(hObject,'String')) returns contents of edit5 as a
% double
global d31 d31=str2double(get(hObject,'String'));

% --- Executes during object creation, after setting all properties.
function edit6_CreateFcn(hObject, eventdata, handles)
% hObject    handle to edit6 (see GCBO)
% eventdata  reserved - to be defined in a future version of MATLAB
% handles    empty - handles not created until after all CreateFcns
% called

% Hint: edit controls usually have a white background on Windows.
%       See ISPC and COMPUTER.
if ispc
    set(hObject,'BackgroundColor','white');
else
    set(hObject,'BackgroundColor',
    get(0,'defaultUicontrolBackgroundColor'));
end
```

```
function edit6_Callback(hObject, eventdata, handles)
% hObject    handle to edit6 (see GCBO)
% eventdata  reserved - to be defined in a future version of MATLAB
% handles    structure with handles and user data (see GUIDATA)

% Hints: get(hObject,'String') returns contents of edit6 as text
% str2double(get(hObject,'String')) returns contents of edit6 as a
% double
global s11 s11=str2double(get(hObject,'String'));

% --- Executes during object creation, after setting all properties.
function edit7_CreateFcn(hObject, eventdata, handles)
% hObject    handle to edit7 (see GCBO)
% eventdata  reserved - to be defined in a future version of MATLAB
% handles    empty - handles not created until after all CreateFcns
% called

% Hint: edit controls usually have a white background on Windows.
%       See ISPC and COMPUTER.
if ispc
    set(hObject,'BackgroundColor','white');
else
    set(hObject,'BackgroundColor',
    get(0,'defaultUicontrolBackgroundColor'));
end



function edit7_Callback(hObject, eventdata, handles)
% hObject    handle to edit7 (see GCBO)
% eventdata  reserved - to be defined in a future version of MATLAB
% handles    structure with handles and user data (see GUIDATA)

% Hints: get(hObject,'String') returns contents of edit7 as text
% str2double(get(hObject,'String')) returns contents of edit7 as a
% double
global e33 e33=str2double(get(hObject,'String'))*(8.85e-12);
```

```
% --- Executes during object creation, after setting all properties.
function edit8_CreateFcn(hObject, eventdata, handles)
% hObject    handle to edit8 (see GCBO)
% eventdata  reserved - to be defined in a future version of MATLAB
% handles    empty - handles not created until after all CreateFcns
% called

% Hint: edit controls usually have a white background on Windows.
%       See ISPC and COMPUTER.
if ispc
    set(hObject,'BackgroundColor','white');
else
    set(hObject,'BackgroundColor',
    get(0,'defaultUicontrolBackgroundColor'));
end



function edit8_Callback(hObject, eventdata, handles)
% hObject    handle to edit8 (see GCBO)
% eventdata  reserved - to be defined in a future version of MATLAB
% handles    structure with handles and user data (see GUIDATA)

% Hints: get(hObject,'String') returns contents of edit8 as text
% str2double(get(hObject,'String')) returns contents of edit8 as a
% double
global rho rho=str2double(get(hObject,'String'));

% --- Executes during object creation, after setting all properties.
function edit9_CreateFcn(hObject, eventdata, handles)
% hObject    handle to edit9 (see GCBO)
% eventdata  reserved - to be defined in a future version of MATLAB
% handles    empty - handles not created until after all CreateFcns
% called

% Hint: edit controls usually have a white background on Windows.
%       See ISPC and COMPUTER.
if ispc
    set(hObject,'BackgroundColor','white');
else
    set(hObject,'BackgroundColor',
```

```
    get(0,'defaultUicontrolBackgroundColor'));
end



function edit9_Callback(hObject, eventdata, handles)
% hObject    handle to edit9 (see GCBO)
% eventdata  reserved - to be defined in a future version of MATLAB
% handles    structure with handles and user data (see GUIDATA)

% Hints: get(hObject,'String') returns contents of edit9 as text
% str2double(get(hObject,'String')) returns contents of edit9 as a
% double
global f f=str2double(get(hObject,'String'));

% --- Executes during object creation, after setting all properties.
function edit10_CreateFcn(hObject, eventdata, handles)
% hObject    handle to edit10 (see GCBO)
% eventdata  reserved - to be defined in a future version of MATLAB
% handles    empty - handles not created until after all CreateFcns
% called

% Hint: edit controls usually have a white background on Windows.
%       See ISPC and COMPUTER.
if ispc
    set(hObject,'BackgroundColor','white');
else
    set(hObject,'BackgroundColor',
    get(0,'defaultUicontrolBackgroundColor'));
end



function edit10_Callback(hObject, eventdata, handles)
% hObject    handle to edit10 (see GCBO)
% eventdata  reserved - to be defined in a future version of MATLAB
% handles    structure with handles and user data (see GUIDATA)

% Hints: get(hObject,'String') returns contents of edit10 as text
% str2double(get(hObject,'String')) returns contents of edit10 as a
% double
```

```
global V V=str2double(get(hObject,'String'));

% --- Executes during object creation, after setting all properties.
function edit11_CreateFcn(hObject, eventdata, handles)
% hObject    handle to edit11 (see GCBO)
% eventdata  reserved - to be defined in a future version of MATLAB
% handles    empty - handles not created until after all CreateFcns
% called

% Hint: edit controls usually have a white background on Windows.
%       See ISPC and COMPUTER.
if ispc
    set(hObject,'BackgroundColor','white');
else
    set(hObject,'BackgroundColor',
    get(0,'defaultUicontrolBackgroundColor'));
end


function edit11_Callback(hObject, eventdata, handles)
% hObject    handle to edit11 (see GCBO)
% eventdata  reserved - to be defined in a future version of MATLAB
% handles    structure with handles and user data (see GUIDATA)

% Hints: get(hObject,'String') returns contents of edit11 as text
% str2double(get(hObject,'String')) returns contents of edit11 as a
% double


% --- Executes on button press in pushbutton1.
function pushbutton1_Callback(hObject, eventdata, handles)
% hObject    handle to pushbutton1 (see GCBO)
% eventdata  reserved - to be defined in a future version of MATLAB
% handles    structure with handles and user data (see GUIDATA)
global l w t d33 d31 s11 e33 rho f V fr
omega=2*pi*f;
cb=1/sqrt(rho*s11);
fr=cb/(2*l)
set(handles.edit11,'String',fr);
k=omega/cb;
time=0;
```

```
E=V./t;
x=linspace(0,l,100);
Psi=((d31*E)/k).*(sin(k.*x)-tan(0.5*k*l).*cos(k.*x));
plot(x,Psi);
grid on xlabel('Distance along ceramic');
ylabel('Displacement(m)');
```

```
%%%%%%%%%%%%%%%%%%%%%%%%%%%%%%%%%%%%%%%%%%%%%%%%%%%%%%%%%%%%%%%%%%%%%%%%%%%%
%This file calculates a low pass pi matching circuit for any array given
%the measured complex impedance of the array at the resonance frequency and
%the desired Q of the circuit.  Source impedance is arbitrary and is
%typically 50ohms. For the program to work, the following conditions for
%the desired Q must be met:
%Q>0
%Q>sqrt( max(Rs,RL)/min(Rs,RL) )
%%%%%%%%%%%%%%%%%%%%%%%%%%%%%%%%%%%%%%%%%%%%%%%%%%%%%%%%%%%%%%%%%%%%%%%%%%%%

%Transducer array parameters
f=28800;           %Resonance frequency of array
w=2*pi*f;
RL=121.86;         %Transducer resistance
XL=-786.017;       %Transducer reactance
ZL=RL+j*XL;


%Source output impedance parameters
RS=50;          %Source resistance
XS=0;           %Source reactance
ZS=RS+j*XS;

%Calculation of C1, L, and C2
Q=2;                  %Desired Q

Rc=max(RS,RL)/(Q^2+1);

QL=-XL/RL;              %Node load Q
RpL=RL*(1+QL^2);        %Equivalent parallel load resistance
CpL=QL/(RpL*w);         %Equivalent parallel load capacitance
q1=sqrt(RpL/Rc-1);      %Match to source
C2=(q1/(w*RpL))-CpL     %C2 value
LL=(q1*Rc)/w;           %Inductance due to load

QS=-XS/RS;              %Node source Q
RpS=RS*(1+QS^2);        %Equivalent parallel source resistance
CpS=QS/(RpS*w);         %Equivalent parallel source capacitance
q2=sqrt(RpS/Rc-1);      %Match to source
C1=(q2/(w*RpS))-CpS     %C1 value
L_S=(q2*Rc)/w;          %Inductance due to source
```

```
L=L_S+LL                %L value


%Calculate the matched and unmatched impedance over the bandwidth
BW=f/Q;             %Bandwidth given by specified Q
f_axis=linspace(round(f-BW/2),round(f+BW/2),1000);
w_axis=2*pi*f_axis;

ZC1=1./(j*w_axis*C1);
ZC2=1./(j*w_axis*C2);
Z_L=j*w_axis*L;

Z1=(ZL.*ZC2)./(ZL+ZC2);
Z2=Z1+Z_L;
Zin=(Z2.*ZC1)./(Z2+ZC1);
Yin=1./Zin;

%Calculate the unmatched impedance over the bandwidth
Ct=1/(2*pi*f*abs(XL));
Zt=RL+1./(j*w_axis*Ct);

%Plots
f_axis=f_axis./1000;
subplot(2,1,1)
plot(f_axis,abs(Zin))
grid on
xlabel('f (Hz)')
ylabel('|Zin|')
title('Impedance magnitude of
rectangular array with matching');
subplot(2,1,2)
plot(f_axis,(180/pi)*angle(Zin))
grid on
xlabel('f (Hz)')
ylabel('Phase (deg)')
title('Impedance phase of rectangular array
with matching');

figure subplot(2,1,1)
plot(f_axis,abs(Zt))
```

```
grid on
xlabel('f (Hz)')
ylabel('|Zin|')
title('Impedance magnitude of rectangular array
unmatched');
subplot(2,1,2)
plot(f_axis,(180/pi)*angle(Zt))
grid on
xlabel('f (Hz)')
ylabel('Phase (deg)')
title('Impedance phase of
rectangular array unmatched');
```

```
%%%%%%%%%%%%%%%%%%%%%%%%%%%%%%%%%%%%%%%%%%%%%%%%%%%%%%%%%%%%%%%%%%%%%%%%%%%%
%This file inputs the ARL water tank test data and computes the cable
%capacitance corrected input current, input voltage, and other important
%far field measurement.
%%%%%%%%%%%%%%%%%%%%%%%%%%%%%%%%%%%%%%%%%%%%%%%%%%%%%%%%%%%%%%%%%%%%%%%%%%%%


%3x3 Cymbal Array
DiskArrayData=dlmread('3x3007.asc',' ',16,0);
VinDiskArraymag=10.^(DiskArrayData(:,2)./20);
VinDiskArrayphase=(DiskArrayData(:,3)).*(pi/180);
IinDiskArraymag=10.^(DiskArrayData(:,4)./20);
IinDiskArrayphase=(DiskArrayData(:,5)).*(pi/180);
VinDiskArray=VinDiskArraymag.*(cos(VinDiskArrayphase)
            +j*sin(VinDiskArrayphase));
IinDiskArray=IinDiskArraymag.*(cos(IinDiskArrayphase)
            +j*sin(IinDiskArrayphase));
SLDiskArray=DiskArrayData(:,9);
VA3x3=10.^(.05*DiskArrayData(:,2)).*10.^(.05*DiskArrayData(:,4));
Eff3x3=DiskArrayData(:,11); DI3x3=DiskArrayData(:,10);
Pa3x3=10.^(.1*(SLDiskArray-170.9-DI3x3)); VAperW3x3=VA3x3./Pa3x3;
TVRDiskArray=DiskArrayData(:,12); ZmagDiskArray=DiskArrayData(:,6);
ZphaseDiskArray=DiskArrayData(:,7);
ZDiskArray=ZmagDiskArray.*(cos(ZphaseDiskArray)+j*sin(ZphaseDiskArray));

%3x1 Rectangular Array
RectArrayData=dlmread('test007.asc',' ',16,0);
VinRectArraymag=10.^(RectArrayData(:,2)./20);
VinRectArrayphase=(RectArrayData(:,3)).*(pi/180);
IinRectArraymag=10.^(RectArrayData(:,4)./20);
IinRectArrayphase=(RectArrayData(:,5)).*(pi/180);
VinRectArray=VinRectArraymag.*(cos(VinRectArrayphase)
            +j*sin(VinRectArrayphase));
IinRectArray=IinRectArraymag.*(cos(IinRectArrayphase)
            +j*sin(IinRectArrayphase));
SLRectArray=RectArrayData(:,9)+20*log10(3);
VA3x1=10.^(.05*RectArrayData(:,2)).*10.^(.05*RectArrayData(:,4));
Eff3x1=RectArrayData(:,11); DI3x1=RectArrayData(:,10);
Pa3x1=10.^(.1*(SLRectArray-170.9-DI3x1)); VAperW3x1=VA3x1./Pa3x1;
TVRRectArray=RectArrayData(:,12)+20*log10(3);
ZmagRectArray=RectArrayData(:,6);
```

```
ZphaseRectArray=RectArrayData(:,7);
ZRectArray=ZmagRectArray.*(cos(ZphaseRectArray)+j*sin(ZphaseRectArray));

%Single element rectangle
SingleRectData=dlmread('1x1012.asc',' ',16,0);
VinSingleRectmag=10.^(SingleRectData(:,2)./20);
VinSingleRectphase=(SingleRectData(:,3)).*(pi/180);
IinSingleRectmag=10.^(SingleRectData(:,4)./20);
IinSingleRectphase=(SingleRectData(:,5)).*(pi/180);
VinSingleRect=VinSingleRectmag.*(cos(VinSingleRectphase)
            +j*sin(VinSingleRectphase));
IinSingleRect=IinSingleRectmag.*(cos(IinSingleRectphase)
            +j*sin(IinSingleRectphase));
SLSingleRect=SingleRectData(:,9)+20*log10(3);
VAsingle=10.^(.05*SingleRectData(:,2)).*10.^(.05*SingleRectData(:,4));
Effsingle=SingleRectData(:,11); DIsingle=SingleRectData(:,10);
Pasingle=10.^(.1*(SLSingleRect-170.9-DIsingle));
VAperWSingle=VAsingle./Pasingle;
TVRSingleRect=SingleRectData(:,12)+20*log10(3);
ZmagSingleRect=SingleRectData(:,6);
ZphaseSingleRect=SingleRectData(:,7);
ZSingleRect=ZmagSingleRect.*(cos(ZphaseSingleRect)+j*sin(ZphaseSingleRect));
```

```
%%%%%%%%%%%%%%%%%%%%%%%%%%%%%%%%%%%%%%%%%%%%%%%%%%%%%%%%%%%%%%%%%%%%%%%%
%This file analyzes the transducer using a parallel tuning inductor.  The
%new impedance is calculated and plotted.  Additionaly, far field
%measurements taken can be changed to show the effects of tuning given that
%the untuned performance has already been loaded into MATLAB.  This
%particular file is for the 3x1 rectangular array.
%%%%%%%%%%%%%%%%%%%%%%%%%%%%%%%%%%%%%%%%%%%%%%%%%%%%%%%%%%%%%%%%%%%%%%%%

%Circuit constants
Lm3x1=13.4e-3;
Cm3x1=1.9e-9;
Rm3x1=1100;
Co3x1=6.58e-9;     %Clamped capacitance

Cc=1340e-12;    %Cable capacitance
Lt3x1=10e-3;     %Tuning inductance
f=linspace(10000,50000,1000);
w=2*pi*f;

Z13x1=j*w*Lm3x1+1./(j*w*Cm3x1)+Rm3x1;
Z23x1=(Lt3x1/Co3x1)./(j*w*Lt3x1+1./(j*w*Co3x1));

Zin3x1=(Z13x1.*Z23x1)./(Z13x1+Z23x1);

subplot(2,1,1)
plot(f,abs(Zin3x1))
grid on
subplot(2,1,2)
plot(f,angle(Zin3x1)*180/pi)
grid on


%%%Changing untuned measured data to tuned%%%
Zmag_untuned3x1=ZmagRectArray;
Zphase_untuned3x1=ZphaseRectArray*pi/180;
Z_untuned3x1=Zmag_untuned3x1.*(cos(Zphase_untuned3x1)
            +i*sin(Zphase_untuned3x1));
Y_untuned3x1=1./Z_untuned3x1; G_untuned3x1=real(Y_untuned3x1);
B_untuned3x1=imag(Y_untuned3x1);

%Correct for cable capacitance
```

```
IinActual_untuned3x1=VinRectArray./Z_untuned3x1;

%Untuned efficiencies
VA_untuned3x1=abs(VinRectArray).*abs(IinActual_untuned3x1);
phi_untuned3x1=angle(VinRectArray)-angle(IinActual_untuned3x1);
TVR_untuned3x1=10*log10(G_untuned3x1)+170.9+DI3x1+10*log10(Eff3x1./100)
            +20*log10(3);
SPL_untuned3x1=TVR_untuned3x1+20*log10(VinRectArraymag);
SrcLvl_untuned3x1=RectArrayData(:,9);
Pin_untuned3x1=VA_untuned3x1.*cos(phi_untuned3x1);
Pout_untuned3x1=10.^(.1*(SPL_untuned3x1-170.9-DI3x1));
Efficiency_untuned3x1=Pout_untuned3x1./Pin_untuned3x1;
VAperW_untuned3x1=VA_untuned3x1./Pout_untuned3x1;

%Calculate tuned performance
f_tuned3x1=linspace(15000,35000,length(Zmag_untuned3x1));
omega_tuned3x1=2*pi*f_tuned3x1;
Y_tuned3x1=Y_untuned3x1.'+1./(i*omega_tuned3x1*Lt3x1);
Z_tuned3x1=1./Y_tuned3x1; G_tuned3x1=real(Y_tuned3x1);
B_tuned3x1=imag(Y_tuned3x1);

Vin_tuned3x1=100*ones(1,101);  %Choose a 100V input
Iin_tuned3x1=Vin_tuned3x1./Z_tuned3x1;

TVR_tuned3x1=10*log10(G_tuned3x1')+170.9+DI3x1+10*log10(Eff3x1./100)
            +20*log10(3);
SPL_tuned3x1=TVR_tuned3x1+20*log10(abs(Vin_tuned3x1'));

VA_tuned3x1=abs(Vin_tuned3x1).*abs(Iin_tuned3x1);
phi_tuned3x1=angle(Vin_tuned3x1)-angle(Iin_tuned3x1);

Pin_tuned3x1=VA_tuned3x1.*cos(phi_tuned3x1);
Pout_tuned3x1=10.^(.1*(SPL_tuned3x1-170.9-DI3x1));
Efficiency_tuned3x1=Pout_tuned3x1'./Pin_tuned3x1;

VAperW_tuned3x1=VA_tuned3x1'./Pout_tuned3x1;
```

```
%%%%%%%%%%%%%%%%%%%%%%%%%%%%%%%%%%%%%%%%%%%%%%%%%%%%%%%%%%%%%%%%%%%%%%%%%%%%
%XY plane exposimetry results for 3x1 rectangular array built Feb 2005
%using CPD 9150 potting material Test was performed at f=28.8 kHz.
%Microphone sensitivity at that frequency is -212.5 dB re 1V/uPa
%%%%%%%%%%%%%%%%%%%%%%%%%%%%%%%%%%%%%%%%%%%%%%%%%%%%%%%%%%%%%%%%%%%%%%%%%%%%

%%%Constants%%%
rho=998;      %densigy (kg/m^3)
c=1481;       %sound speed (m/s)
x=linspace(-50,50,101);
y=linspace(-45,45,91);

%%%Data%%%
Vmaxtemp=load('R31max.dat');
Vmintemp=load('R31min.dat');
Vrmstemp=load('R31rms.dat');

%Convert to correct indices
Vtemp=Vrmstemp;
Vnew=Vtemp;
[sizey sizex]=size(Vtemp);

for ii=1:sizey
    if mod(ii,2)==0
        for jj=1:sizex
            Vnew(ii,sizex-jj+1)=Vtemp(ii,jj);
        end
    end
end

Vrms=Vnew;

%%%Convert to acoustic data%%%
MicS=-212.5;            %Microphone sensitivity (dB re 1V/uPa)
S=10^(MicS/20)*10^6;    %Microphone sensitivity (V/Pa)

%Pressure
p_min=(1/S)*Vmin;       %min pressure (Pa)
p_max=(1/S)*Vmax;       %max pressure (Pa)
p_rms=(1/S)*Vrms;       %RMS pressure (Pa)
```

```
%Intensity
I=((p_rms).^2./(rho*c))*.1;  %Time average intensity (mW/cm^2)
IdB=10*log10(I./max(max(I)));

%Plots
imagesc(x,y,IdB)
grid on
colorbar
xlabel('x (mm)');
ylabel('y(mm)');
zlabel('I (dB)');
title('Intensity on X-Y plane at 1mm of 3x1 rectangular cymbal
transducer')

figure mesh(x,y,IdB)
xlabel('x (mm)');
ylabel('y (mm)');
zlabel('I(dB)');
title('Intensity on X-Y plane at 1mm of 3x1 rectangular cymbal
transducer')
```

Appendix B

ATILA/GiD Model Procedure

This work used the finite element program ATILA with GiD as the pre and post processor. ATILA is particularly useful for modeling piezoelectric and magnetostrictive transducers. In addition, a boundary element program known as EQI can be used with ATILA to make underwater transducer calculations easier. A description of the creation of the rectangular cymbal model, as well as a description of some of the subtleties that one can run into when using this software are described here.

B.1 Creating the Model

The ATILA tutorial as well as the GiD tutorial are useful in learning how to create points, lines, surfaces, and volumes. For this reason, those tasks are omitted here. Instead, a description of the tasks particular to the cymbal model will be described.

We can begin by creating the ceramic of the transducer. Due to the transducer's symmetry, we only need to model 1/8th of the transducer. Figure B.1 shows the volume created in GiD to model the 1/8th of the ceramic. Note that the volume is created in pieces, distinguishing

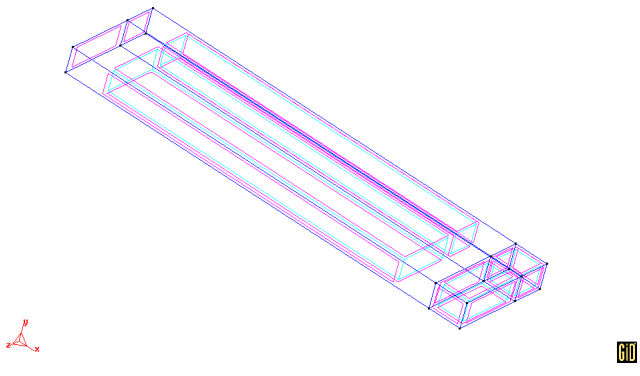

Figure B.1: Volume created to model 1/8th of the rectangular transducer ceramic

which sections of the ceramic will be in contact with the cap. This makes adding the cap into the model simpler. In addition, it is useful to create different layers for each part of the model. Layers can be defined by using the Utilities menu and selecting Layers. By defining layers, changes can be made to certain parts of the model that won't affect the entire model. This is especially useful for complex systems that include a large number of pieces or parts.

The cap can be made and the 1/8th model for the cap is shown in Figure B.2. Once again, the cap is separated into volumes that will make it easier to define material properties as well as define a structured mesh later on. The completed model of the rectangular cymbal

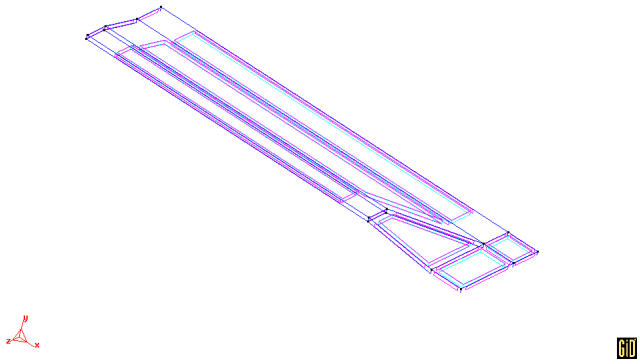

Figure B.2: Volume created to model 1/8th of the rectangular transducer cap

transducer is shown in Figure B.3.

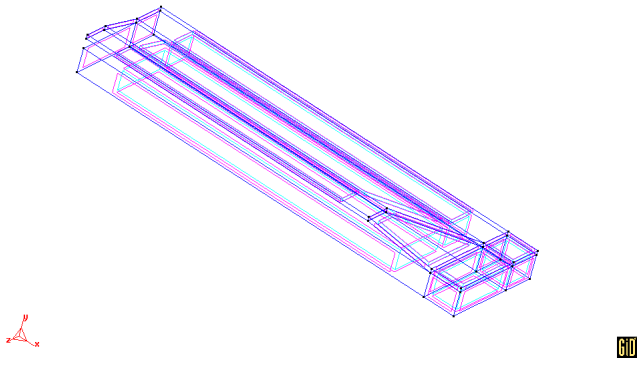

Figure B.3: Volume created to model 1/8th of the rectangular transducer

Changes to the model can be difficult to make since dimensions of volumes or surfaces cannot simply be resized. However, if a volume needs to be elongated you can use the Copy command in the Utilities menu. The copy menu is shown in Figure B.4. Although the copy

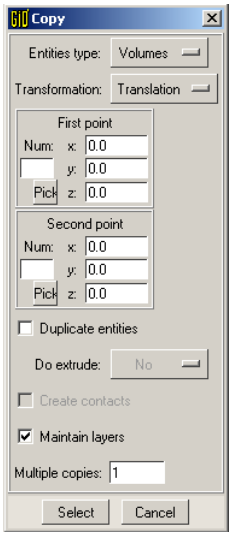

Figure B.4: GiD menu displayed by selecting Copy under Utilities

function cannot directly scale the model, you can translate surfaces or volumes in order to vary the dimensions of the transducer. To do so, select the desired surfaces or volumes, and define a vector in the direction you wish to translate. Changing the model in this way is faster than creating a new model. However, all definitions associated with the volume as well as with the surfaces and points are erased and need to be redefined.

Once the volume of the model has been created, you can begin to define the parts of the transducer. Either before the model is created, or before defining volumes, be sure to specify that the model will be using ATILA. This can be done by selecting the proper problem type as shown in Figure B.5.

Specifying this type of model should also bring up a new column of selections directly to the right of the geometry command selections also shown in Figure B.5. These commands allow the specification of materials as well as the frequency band to calculate in. In addition, surface and volume definitions can be easier to make if the view is rendered as flat or smooth lighting. This shows the model as volumes and surfaces of different colors as defined by the user in the Layer menu. Selection of volumes and surfaces can then be made simpler by selecting the color associated with the surface or volume to be defined. Table B.1 shows the necessary definitions that must be made for this particular model.

In Table B.1, outer surfaces correspond to any surface of the model that will be radiating

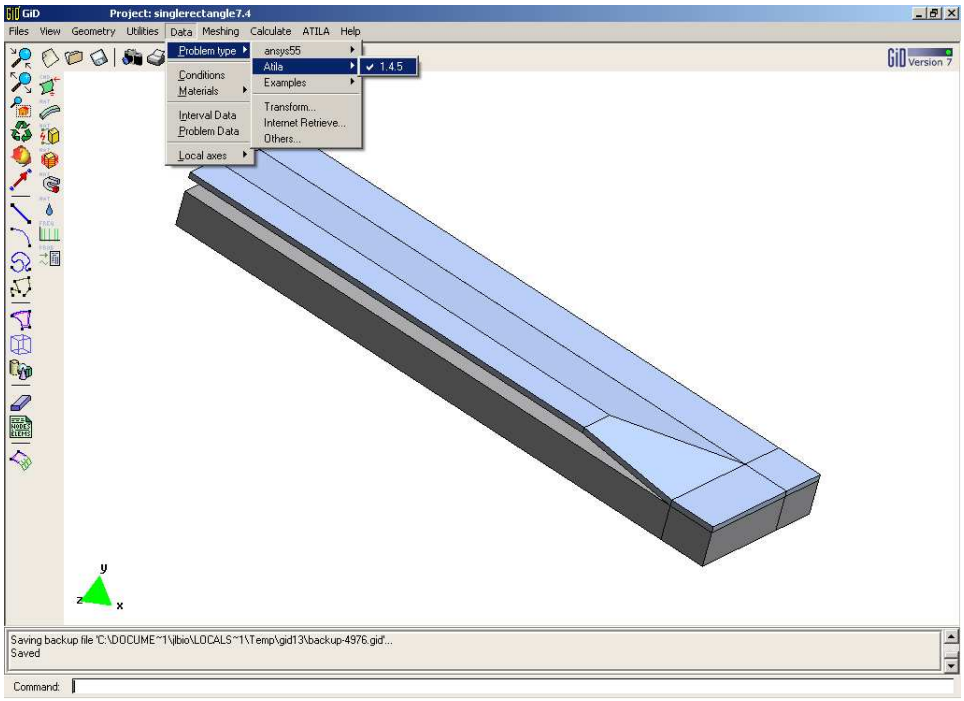

Figure B.5: Selecting the ATILA problem type for the model of the rectangular cymbal created using GiD

or in contact with the external environment. BEM constraints enable the use of EQI to calculate the radiation properties of the transducer in water. If EQI is not being used, a large water volume can be created surrounding the transducer, and a radiating boundary can be made on the surface of this volume. This can increase calculation time but it can also be used as a way to calculate radiation properties.

Symmetry surfaces refer to planes of symmetry. By clamping the planes of symmetry we force a zero displacement at the planes of symmetry, which will occur in the real transducer because of the boundary conditions at the transducer ends.

Once all conditions have been assigned, a mesh can be automatically generated or specified and calculations can begin. The following section describes this process.

Table B.1: Volume and surface constraints to be defined for the rectangular cymbal in GiD

Layer	Geometry	Constraint
Ceramic	Volume	PZT-4
	Volume	Polarization vector
	Outer surface	BEM
	Symmetry surface	Clamped
	Top surface	Non-zero electric potential
	Bottom surface	Zero electric potential
Cap	Volume	Titanium
	Outer surface	BEM
	Symmetry surface	Clamped

B.2 Calculating Transducer Properties

B.2.1 Creating a Mesh

In order to begin calculations, a mesh needs to be generated. A mesh can be generated automatically by GiD. However, this mesh may be coarser than is necessary to obtain accurate solutions and will tend to increase calculation times. Because we have been careful when building our model and only have quadrilateral volume elements, we can structure our own mesh quite easily and minimize the number of elements created while still obtaining accurate solutions.

Specifying your own mesh is known as a structured mesh. We can create a structured mesh by first going to the Mesh option and selecting Volume under the Structured option. This prompts the user to select a volume for creating a structured mesh. After selecting a single volume and pressing Esc, a menu for specifying the number of elements is shown as in Figure B.6. The number selected will be the number of elements created along the dimension to be specified following this menu. Once a number is given, you can select a dimension of your volume. Notice that the adjacent side of your volume is also highlighted since the elements will be made across the volume and not simply the line selected. After specifying a number of elements for each side of the volume, you can select a new volume and continue the process until the entire mesh has been structured. An important thing to remember is that all adjacent volumes must have the same number of elements along their common dimensions in order for GiD to create a valid structured mesh.

Once the structured mesh has been defined, a mesh can be generated by using the Generate Mesh command under Meshing. Figure B.7 shows the final created structured mesh. You must be sure all frequency specifications and material properties have been defined before

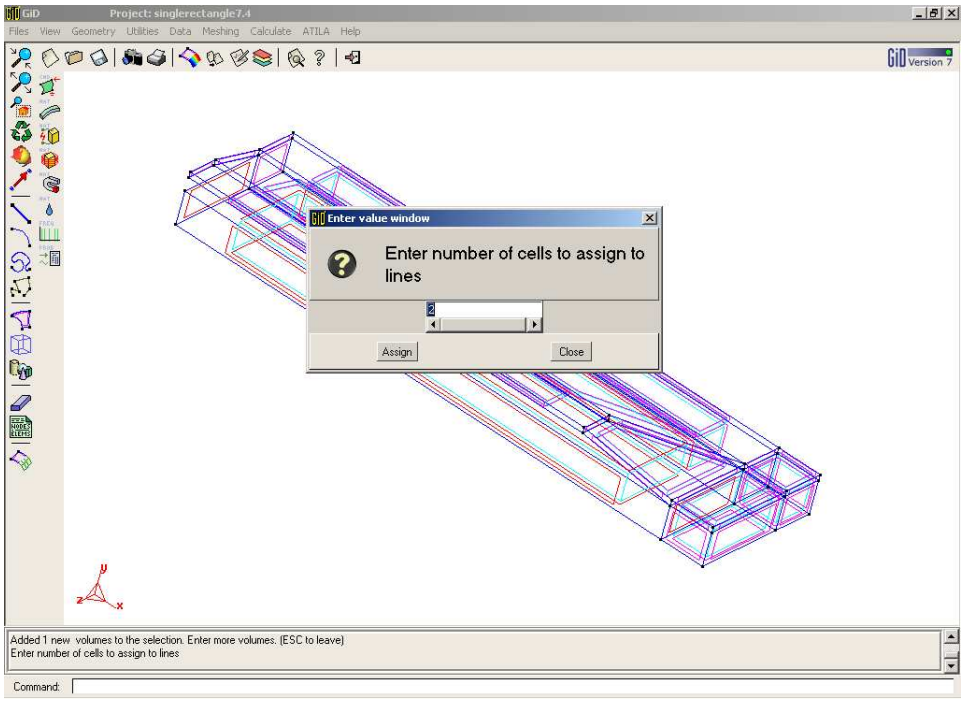

Figure B.6: Menu used to specify number of elements along a dimension when creating a structured mesh

generating the mesh to be certain that all properties will be accounted for when calculating.

B.2.2 Running Calculations

Calculations can be run via GiD or using ATILA supervisor. Using ATILA supervisor is advantageous since EQI can be used to calculate properties underwater. Using GiD can be useful since after calculations are done by ATILA, GiD can then be used as a post processor to present the data.

To calculate using GiD, simply use the Calculate command under the Calculate option. This begins calculation of the transducer properties at each frequency specified. Once finished, you can toggle between pre and post processor to view the impedance, admittance, and phase of the transducer.

To use ATILA supervisor, first use the Convert to ATI command under the ATILA option. Converting the model to ATI allows you to use ATILA supervisor to generate solutions. Also under ATILA you can select AILA Supervisor when the ATI file has been created.

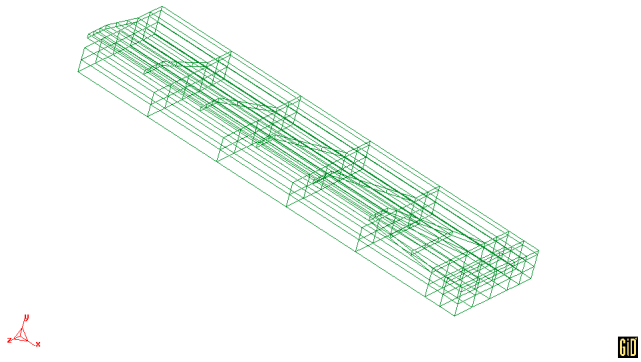

Figure B.7: Structured mesh created by GiD for the rectangular cymbal

Using the File menu, select the project.ati file that was created in the model folder. By selecting the computation tab in ATILA supervisor we see the the options shown in Figure B.8. Pressing the Solver button will begin computation.

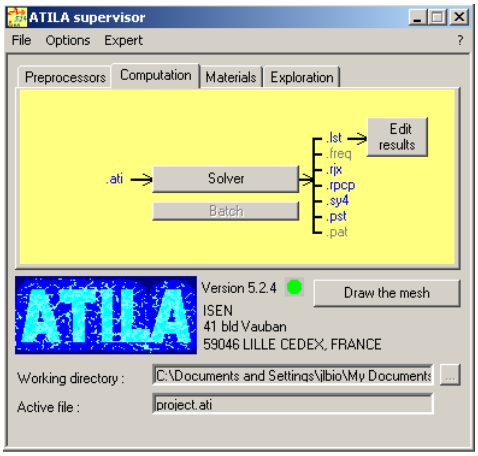

Figure B.8: Computation menu when using ATILA supervisor

Obtaining the solution data is not as user friendly as with using GiD. Once the solver is finished, the solutions are in the GiD model directory. In this folder there will be a file with extension rjx. This file contains impedance data. In the folder called project, there will be a number of files, each one corresponding to a single frequency calculation. Within each file are decibel levels associated with angles 0 to 90°. By selecting the values from each file at 90° you can obtain the predicted TVR of the transducer.

Appendix C

Rectangular Transducer Measurements

The following Appendix shows various measurements taken during far field and near field testing of the rectangular single element and 3x1 array. In addition, for far field measurements, the conditions of the test are shown. This will give the reader an idea of the electrical conditions under which the acoustic measurements were made. All measurements will vary slightly between each transducer and each array but these plots show typical characteristics of the rectangular cymbal transducer elements and arrays.

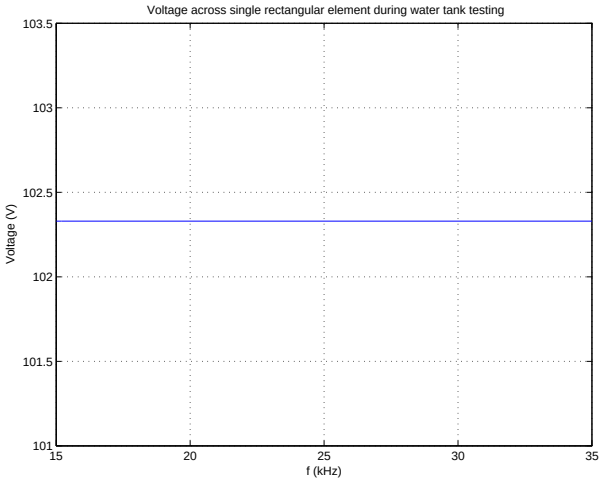

Figure C.1: Applied voltage to a single element rectangular transducer during far field underwater testing

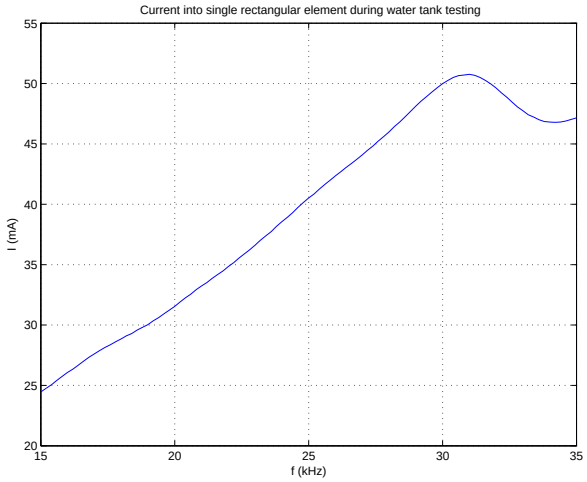

Figure C.2: Current supplied to a single element rectangular transducer during far field underwater testing

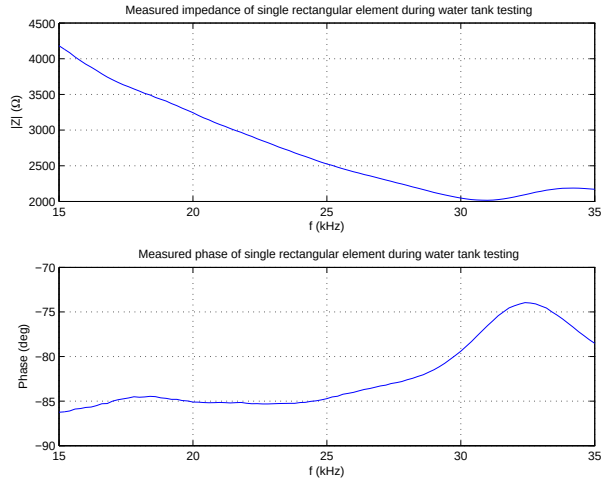

Figure C.3: Measured impedance magnitude and phase of a single element rectangular transducer

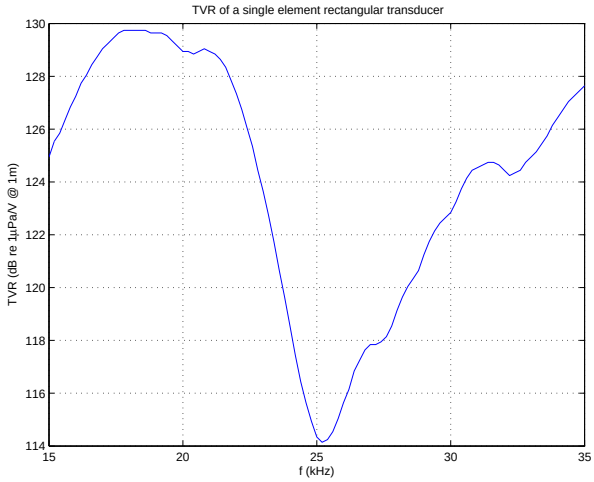

Figure C.4: TVR of a single element rectangular transducer

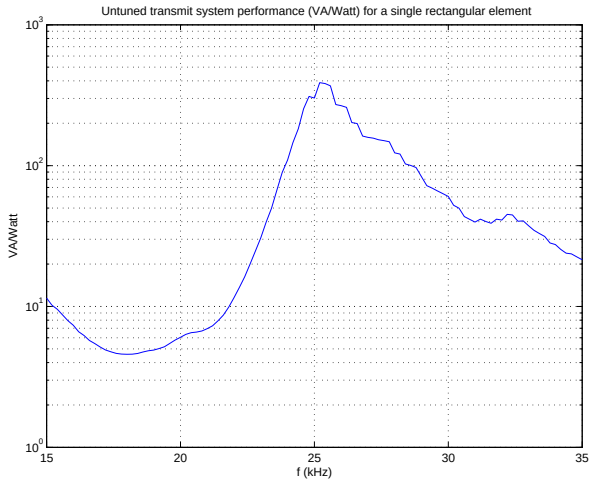

Figure C.5: VA/Watt ratio of an untuned single element rectangular transducer

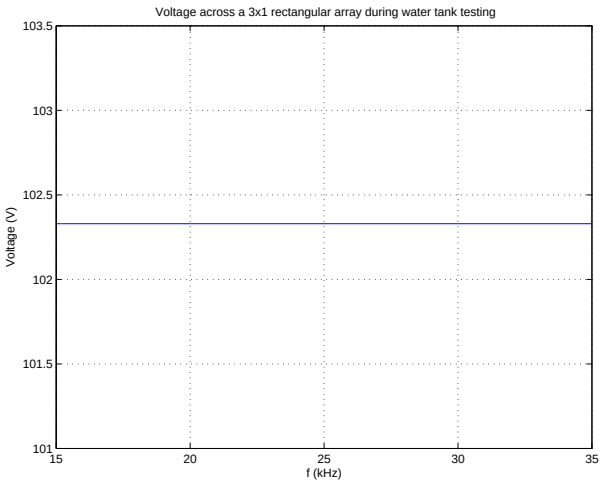

Figure C.6: Applied voltage to a 3x1 rectangular array during far field underwater testing

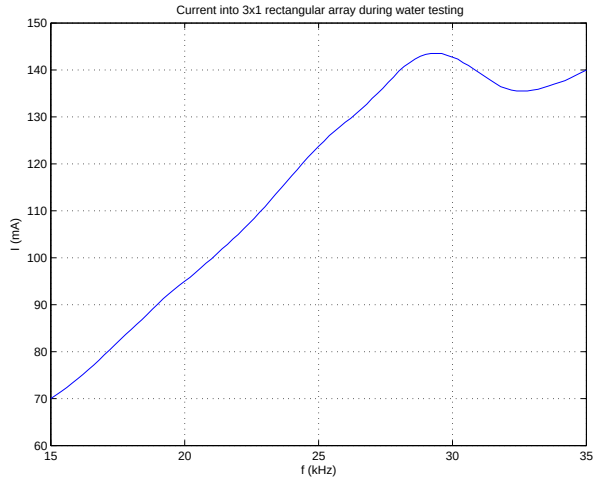

Figure C.7: Current supplied to a 3x1 rectangular array during far field teting

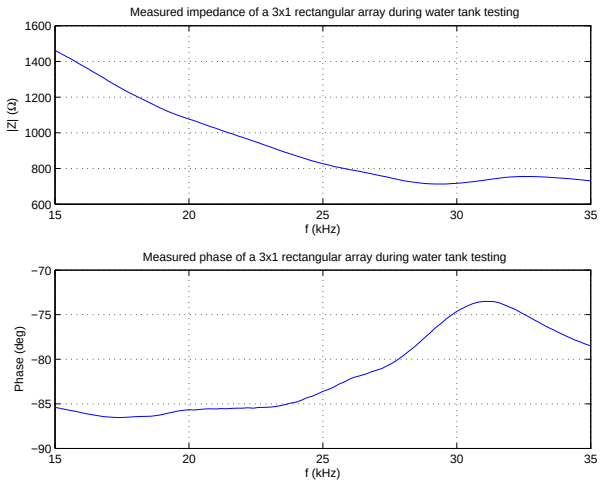

Figure C.8: Measured impedance magnitude and phase of a 3x1 rectangular array

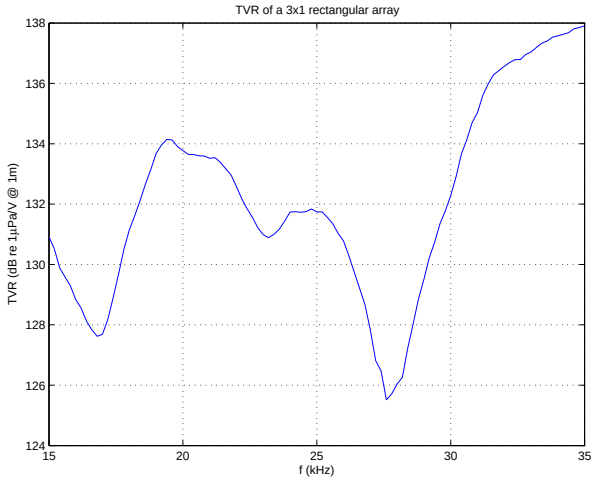

Figure C.9: TVR of a 3x1 rectangular array

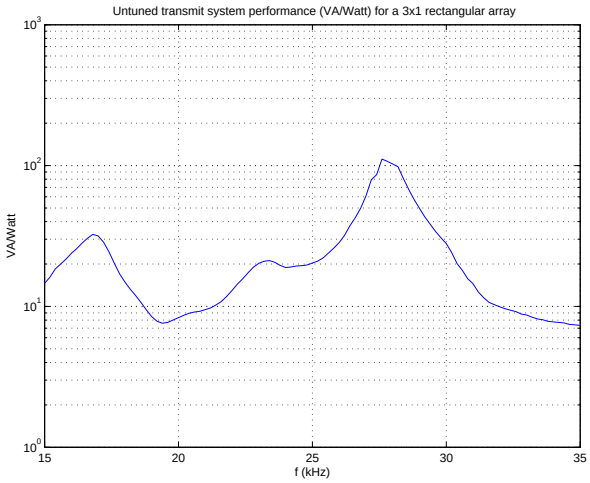

Figure C.10: VA/Watt ratio of an untuned 3x1 rectangular array

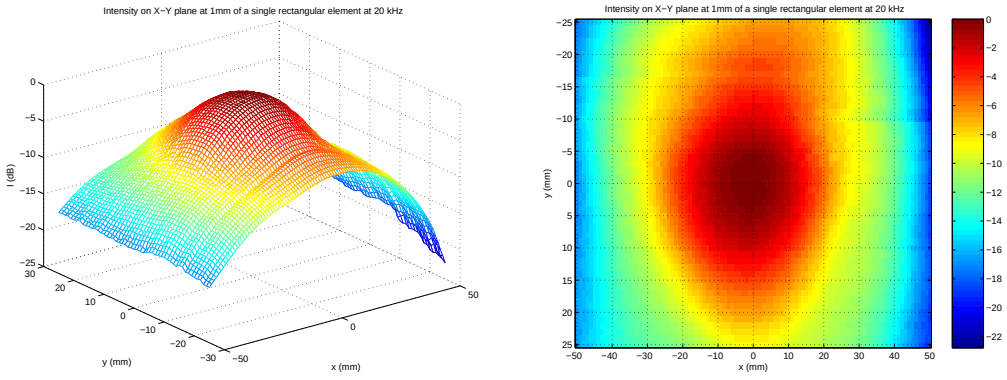

Figure C.11: Exposimetry of a single element rectangular cymbal transducer array 1 mm from the transducer face at 20 kHz

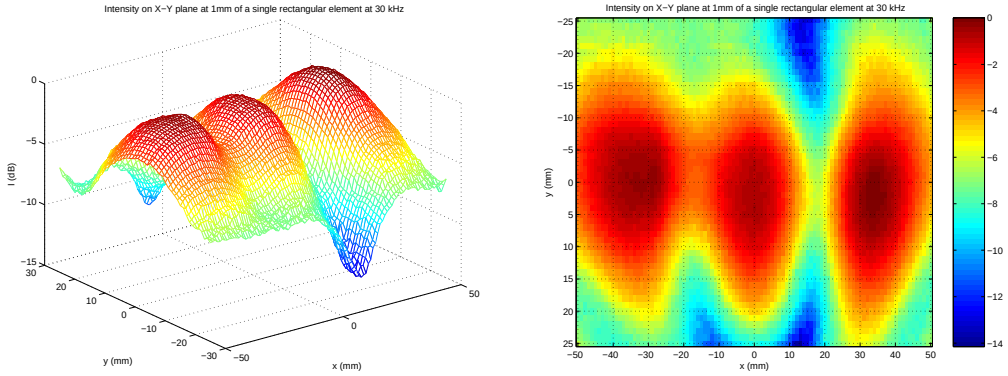

Figure C.12: Exposimetry of a single element rectangular cymbal transducer array 1 mm from the transducer face at 30 kHz

Bibliography

[1] American Diabetes Association, *Economic Costs of Diabetes in the U.S. in 2002*, Diabetes Care, Vol. 26, No. 3, 2003

[2] Smith, N.B., Newnham, R.E., Hughes, J.W., Meyer, R.J., Jr., Shung, K.K., Maione, E., *Transducer Design for a Portable Ultrasound Enhanced Transdermal Drug-Delivery System*, IEEE Transactions on Ultrasonics, Ferroelectrics and Frequency Control, Vol. 49, No. 10, 2002

[3] Lee, S. *Ultrasound-Mediated Transdermal Insulin Delivery and Glucose Measurement Using the Cymbal Array*, PhD Thesis, Pennsylvania State University, Department of Bioengineering, August 2004

[4] Mitragotri, S., Kost, J., *Low-frequency Sonophoresis: A Review*, Advanced Drug Delivery Reviews, Vol. 55, Issue 5, March 2004

[5] Joshi, A., Raje, J., *Sonicated Transdermal Drug Transport*, Journal of Conrolled Release, 83, 2002

[6] Smith, N.B., Lee, S., Shung, K.K., *Ultrasound-Mediated Transdermal In Vivo Transport of Insulin with Low-Profile Cymbal Arrays*, Ultrasound in Medicine & Biology, Vol. 29, No. 8, 2003

[7] Snyder, B., *Design, Development, and Implementation of the 3x3 Cymbal Array for Transdermal Insulin Delivery*, MS Thesis, The Pennsylvania State University, Department of Bioengineering, May 2004

[8] Marieb, E.N., *Human Anatomy & Physiology Fifth Edition*, Benjamin Cummings, 2001

[9] Leighton, T.G., *The Acoustic Bubble*, Academic Press, San Diego, CA, 1994

[10] Mitragotri, S., Edwards, D.A., Blankschtein, D., Langer, R., *A Mechanistic Study of Ultrasonically-Enhanced Transdermal Drug Delivery*, Journal of Pharmeceutical Science, 84 (6), 1995

[11] Kost, J., *Ultrasound-Assisted Insulin Delivery and Noninvasive Glucose Sensing*, Diabetes Technology and Therapeutics, Volume 4, Number 4, 2002

[12] Merino, G., Kalia, Y.N., Delgado-Charro, M.B., Potts, R., Guy, R., *Frequency and Thermal Effects on the Enhancement of Transdermal Transport by Sonophoresis*, Journal of Controlled Release, 88, 2003

[13] Wilson, O.B., *Introduction to Theory and Design of Sonar Transducers*, Peninsula Publishing, Los Altos, CA, 1988

[14] Tressler, J.F., *Capped Ceramic Underwater Sound Projector The 'Cymbal'*, PhD Thesis, The Pennsylvania State University, Department of Materials Science and Engineering, 1997

[15] Kinsler, L.E., Frey, A.R., Coppens, A.B., Sanders, J.V., *Fundamentals of Acoustics*, Fourth Edition, John Wiley & Sons, Inc., 2000

[16] Jensen, J.A., *Estimation of Blood Velocities Using Ultrasound A Signal Processing Approach*, Cambridge University Press, 1996

[17] IEEE Ultrasonics, Ferroelectrics, and Frequency Control Society, *IEEE Standard on Piezoelectricity*, 1988

[18] Newnham et. al., United States Patent 5,729,077, March 17, 1998

Rectangular cymbal arrays for ultrasonic transdermal insulin delivery[a)]

Joseph Luis[b)]
The Pennsylvania State University

Nadine Smith
The Pennsylvania State University

Richard J. Meyer Jr.
The Pennsylvania State University

(February 12, 2006)

Running title: Rectangular cymbal arrays for ultrasonic transdermal insulin delivery

[a)] Submitted in February 2006 to the Journal of the Acoustical Society of America.
[b)] Current address: JBL Professional, 8400 Balboa Blvd, Northridge, CA, 91329; jluis@harman.com

Joseph Luis, JASA

ABSTRACT

The use of sonicators for transdermal drug delivery has led to the development of lightweight cymbal arrays for use in a portable device. These arrays have proven effective in delivering therapeutic levels of insulin in rats and rabbits. To improve the system, rectangular cymbals are used in a 3x1 array. Rectangular cymbals maximize packing density and allows the flexural cap resonance and the ceramic length mode resonance frequencies to be designed closer in frequency. Bringing the cap and ceramic resonances closer together increases the transmitting power and improves the electrical efficiency. In addition, by using higher order modes excited in the cap while operating at the first ceramic resonance frequency, the intensity spatial average at a distance of 1 mm is increased, effectively sonicating more of the skin and nearly doubling the insulin delivery rate over the period of one 90 minute rabbit experiment. Using rectangular cymbal arrays improves the current portable insulin delivery system by decreasing the total power consumed and increasing the insulin delivery rate.

PACS numbers: 43.38.Fx, 43.80.Sh

Joseph Luis, JASA

I. INTRODUCTION

Non-invasive methods of drug delivery have been studied for some time to eliminate the pain induced by methods such as injections. In particular, alleviating the pain from needles during a diabetic's insulin shots is of interest due to the large number of type I and type II diabetics requiring blood glucose level regulation. Using ultrasound as a way to make the skin permeable enough to allow drugs to more readily diffuse through has proven to be an effective and painless method of delivering larger molecule drugs.[1,2] This work has shown that using ultrasonic treatments is a promising and painless method for delivering therapeutic levels of drugs to patients.

In addition to having a system to sonicate and deliver drugs transdermally, it would be useful to have a portable delivery device. A transducer array has been developed that can produce the necessary intensity levels to increase skin permeability and maintain a low profile.[3,4] The portable "patch" uses the cymbal, a flextensional transducer made of a circular piezoelectric ceramic sandwiched between two metal end caps.[5] The small radial displacement of the ceramic is mechanically transformed into larger displacements of the metal end caps. Using the cymbal transducer allows the use of 2x2 or larger arrays in a low profile device, a necessary design criteria for a portable transducer.

Various animal tests using rats and rabbits have been done to show the effectiveness of the 2x2 and 3x3 arrays in transdermal insulin delivery systems.[6,7] In rat experiments, the 2x2 array was used to deliver a 60 minute ultrasound treatment operating at $I_{sptp} = 100\ mW/cm^2$. The frequency of operation was 20 kHz and the ultrasound was pulsed with a 20% duty cycle and a 200 ms pulse duration.[6] Xylazine was used as a general anesthetic as well as to cause temporary (12 hr) hyperglycemia. Results in rats show a glucose level drop up to 276.5±61.9 mg/dL after the 60 minute ultrasound exposure.[6] Glucose levels continued to drop after the ultrasound treatment and 90 minutes after the initial ultrasound exposure there was a drop of 297.7±52.8 mg/dL.[6]

Because therapeutic levels of insulin would need to be delivered to larger animals, a 3x3 array configuration was built. Animal tests on rabbits were performed under the same intensity and pulse conditions using the new array and a drop in glucose level in rabbits averaged 94.1±32.3 mg/dL at the end of the 60 minute treatment, and 136.1±26.1 mg/dL measured 90 minutes after the beginning of ultrasound treatment.[7]

Although the cymbal transducer allows for a thin device, its circular geometry is not optimal if we are to obtain a minimal surface area array. For a portable insulin delivery device, we would prefer a cymbal transducer that is electrically more efficient at a single frequency in order to minimize battery drain. One improvement can be made by bringing the ceramic and cap resonances closer together. Doing so increases the displacement of the caps and increases the electrical efficiency.

In a sonicating device for transdermal drug delivery, a larger spatial average intensity can give higher drug diffusion rates. Previous 2x2 and 3x3 cymbal arrays have shown spatial intensity distributions with high intensities at the center of the device and rapid intensity drop off.[4,7] This type of spatial intensity distribution results in larger arrays that are not able to adequately improve the insulin delivery rate.[7] By exciting higher order modes in the cap we can increase the spatial average intensity.

To achieve a greater electrical efficiency and obtain a larger spatial average intensity at a 1 mm distance from the transducer, a rectangular cymbal was used.[8] The rectangular array was no larger than the 3x3 array previously used and a single rabbit experiment was performed to verify the effectiveness of the device.

II. MATERIAL AND METHODS

II.A. TRANSDUCER DEVELOPMENT

The circular cymbal arrays used the first resonance frequency of the caps for acoustic radiation. In order to maintain the same system operation frequency it is necessary to increase the cap size so that the same operation frequency excites

higher order modes in the cap. Higher order modes will create a more desirable spatial intensity profile.

Increasing the overall size of a circular ceramic decreases the first ceramic resonance frequency. Radial modes are governed by Equation 1

$$J_1(\eta) = 1 - \sigma^p \tag{1}$$

where J_1 is the Besel function of the first kind of first order, η is an argument proportional to the frequency, and $\sigma^p = -s_{12}^E/s_{11}^E$.[9] The first root of Equation 1 places the ceramic resonance of the circular cymbal near 100 kHz, far from the 20 kHz first resonance of the cap. A larger cap with a rectangular ceramic geometry resolves this issue.

A rectangular cymbal operates in the 3-1 ceramic mode where the longitudinal strain is given by Equation 2

$$S_1(x) = d_{31}E_o[cos(kx) + tan(\frac{k\ell}{2})sin(kx)] \tag{2}$$

where E_o is the electric field applied, $k = \omega/c$, c is the speed of sound in the long bar, and ℓ is the length of the bar. The expression for the admittance of the 3-1 bar is shown in Equation 3

$$Y = \frac{j\omega w d_{31}^2}{s_{11}^E kt}\sin(k\ell)[1 + \tan^2(\frac{k\ell}{2})] + \frac{j\omega w\ell}{t}[\epsilon_{33}^T - \frac{d_{31}^2}{s_{11}^E}] \tag{3}$$

where w is the width of the bar and t is the bar thickness. From Equations 2 and 3 the ceramic resonances now occur when $k\ell = (2n-1)\pi$, giving a first ceramic resonance of $f_r = c/2\ell$. A bar length of 50 mm, a similar length of a 3x3 circular array, results in a first resonance of 33 kHz. The system can now be operated at the ceramic resonance instead of the cap resonance giving maximum longitudinal strain of the bar.

II.B. TRANSDUCER MODELING

The final rectangular array was not to exceed the dimensions of the 3x3 circular array. In order to have a rectangular array of the same size, a 3x1 array was made with element dimensions of 50 x 12.7 x 3 mm^3. A finite element model of a single element was made to determine predict cap displacement and electrical impedance. ATILA is used as the processor for the model since it is a particularly useful tool for piezoelectric and magnetostrictive systems. Figure 1 shows a $1/8^{th}$ model of a single rectangular transducer element and the predicted cap displacement when operated at the first ceramic resonance.

II.C. Transducer Construction

Construction of the rectangular cymbal transducers is done by hand. It is important to note that symmetry when fabricating the transducers is crucial to the performance of the device.

Rectangular Navy Type I 402 ceramics were ordered from Piezokinetics poled in the thickness direction to use in the 3-1 bar configuration. The titanium caps are made from titanium sheets obtained from Alfa Aesar with a 0.25 mm thickness. The titanium is cut into strips the same width and length as the rectangular ceramic.

The cap is shaped by pressing the cap using a shaping die. One cap at a time is placed in the shaping die and pressed at 60 kpsi. Cap heights are measured at the center of the cap using a Starrett dial gauge. For symmetry, caps with the closest cap heights are paired together.

The caps are bonded to the ceramics using Emerson-Cuming Eccobond 45 LV epoxy base and 15 LV catalyst in a 3:1 ratio. Arrays can be made by electrically connecting the transducers and potting them in a polyurethane. A conductive adhesive is used to connect the transducers in parallel. A two part polyurethane with a 90A shore hardness is mixed, degassed, and poured on the array. Figure 2 shows a single rectangular cymbal transducer and a 3x1 rectangular potted array compared

to a 3x3 circular potted array.

II.D. Far Field Measurements

As a method of comparing transducer efficiencies, far field measurements are taken at the Applied Research Laboratory (ARL) water tank. Transmitting voltage response (TVR) and a volt-amp per watt ratio (VA/Watt) is measured. TVR is a ratio of the sound pressure at a distance of 1 m in a specified direction to the voltage applied. The reference voltage is 1 V and the ratio is expressed in dB re 1 $\mu Pa \cdot m/V$.

Ideally, we wold like to convert all electrical power delivered to the transducer into acoustic power out. However, in this particular system, the transducer behaves like a capacitor and the conversion of electrical to acoustic energy is not ideal. It is convenient to use an efficiency ratio known as the volt-amp per watt ratio (VA/W). Applied voltage and current are measured at the transducer and the product is divided by the total acoustic power output measured. An ideal ratio would equal one. For the cymbal transducers used in arrays a typical value of VA/W is on the order of 100.

II.E. Near Field Exposimetry

Of interest is what the intensity profile looks like close to the transducer. The transducer face will be approximately 1 mm away from the skin when in use and at that distance it is necessary to know how the acoustic intensity is distributed spatially. A method of measuring this profile is to use an exposimetry system. In such a system, the transducer is stationary and a hydrophone on a motor controlled system makes user specified steps and measures the pressure in a plane in front of the transducer. Exposimetry plots are presented in dB with respect to the highest intensity in order to show how the spatial distribution of intensity falls off as you move away from the maximum radiation point.

II.F. Animal experiments

In order to determine the effectiveness of the arrays in ultrasonic transdermal insulin delivery, animal tests are performed. All animal experiments are approved by The Pennsylvania State University's Institutional Animal Care and Use Committee (IACUC), protocol number 15262.

The rabbits to be tested are first anesthetized. A combination of ketamine hydrochloride and sodium xylazine is used as an anesthetic. Specific doses vary by animal weight, with ketamine and xylazine being delivered in the doses 40 mg/kg and 10 mg/kg respectively. Using xylazine induces hyperglycemia in the the rabbits and blood glucose levels rise to nearly triple normal levels. This hyperglycemic state is steady for nearly 10 to 12 hours.

Once the animal is under anesthetic, the area to be treated is shaved. For these experiments the thigh area was used. A small plexiglass stand off is made for the transducer in order to have a small reservoir of insulin between the transducer and the rabbit's skin.

Humulin R insulin with a 50 U/mL concentration is placed in the reservoir. Blood is drawn from the ear to take an initial blood glucose level reading using an Accu-Chek glucose monitor. Two monitors are used and results are averaged since measurements from the Accu-Chek systems vary slightly.

After the initial check of the blood glucose level, the ultrasound is turned on at $I_{sptp} = 50\ mW/cm^2$, half of the previously used intensity, at the first resonance frequency of the transducer (∼30kHz) and is pulsed with a pulse period of 1 second and a 20 % duty cycle. A blood glucose measurement is made every 15 minutes. The ultrasound is turned off after 60 minutes but the transducer and the insulin is left on the skin and two more measurements at 75 and at 90 minutes are made. The result is a 90 minute test of which the first 60 minutes includes a pulsed ultrasound exposure at the spatial and temporal peak intensity specified. The levels are normalized to show changes in overall blood glucose levels in the rabbits during the 90 minute tests.

III. Results

After construction, each transducer's admittance in air is measured and compared to the ATILA predicted admittance. Figure 3 (a) shows the measured and predicted admittance magnitude and phase for a single element rectangular transducer in air. The first resonance is well predicted by ATILA. The underwater admittance is then measured as shown in Figure 3 (b) and the first resonance frequency is the system operation frequency.

The TVR of the 3x1 arrays and the circular 3x3 arrays are compared. Figure 4 shows the measured TVR for the 3x3 circular and the 3x1 rectangular arrays. There are dips in the TVR for the rectangular array that are due to asymmetrical modes in the device. These are due to asymmetries in the device caused by making the transducers by hand. Over the rest of the band the rectangular arrays outperform the previous circular cymbals. For this system, the arrays will be operated at a single frequency and the asymmetrical modes are of minimal consequence. In order to use a large frequency band the manufacturing process needs to be improved to eliminate asymmetries that occur.

In the frequency of interest, the VA/Watt ratio is compared between the 3x3 circular and the 3x1 rectangular arrays. Figure 5 (a) shows the measured untuned VA/Watt ratios for the 3x3 circular and the 3x1 rectangular arrays. The 3x1 rectangular arrays improve the electrical efficiency of the system. As seen in the TVR measured, there are peaks that correspond to asymmetrical modes in the transducer due to small asymmetries in the device introduced during the construction process.

For a portable system, an untuned device would drain the battery quickly. For single frequency operation the arrays can be tuned to obtain a high efficiency at the operating frequency. For this particular work, the arrays are parallel tuned. An inductor is placed in parallel with the device and is designed to resonate at a user specified frequency with the known clamped capacitance of the array. By doing so, the efficiency is increased by an order of magnitude at a single frequency as shown

in Figure 5 (b).

The near field spacial intensity distribution partially determines the insulin delivery rate. Exposimetry comparisons of the 3x3 circular arrays and the 3x1 rectangular arrays show an improved spatial intensity distribution using the rectangular elements. Figure 6 (a) shows an exposimetry plot of the spatial intensity distribution 1 mm from the face of the transducer in dB of a 3x3 circular transducer array. There is a maximum intensity point in the center and the intensity falls off quickly in all directions. Figure 6 (b) shows the exposimetry plot of the spatial intensity distribution for the 3x1 rectangular array. There are three intensity maximums and the -3 dB points are further out in all directions. Exciting higher order modes in the caps creates a distribution with a higher spatial average intensity.

Animal experiments help determine the effectiveness of the arrays. A rabbit experiment was performed as described in Section II.F. Figure 7 shows the results of the rabbit experiments with the 3x3 circular and 3x1 rectangular arrays as well as two controls. The results are shown as a change in glucose level and are normalized to the first blood glucose measurement made. Over the single 90 minute test, the 3x1 rectangular array shows nearly double the decrease in glucose level, with the rectangular array decreasing the glucose level by 186 mg/dL and the circular array by 95.5 mg/dL. More tests need to be performed to determine the standard deviation between tests but the large difference shows the potential for using the new device.

IV. Discussion

A new cymbal transducer with a rectangular shape was modeled, constructed, and tested as an improvement over the circular transducer design currently used in the portable ultrasonic drug delivery device. Previous cymbal designs have been shown to be effective at delivering therapeutic levels of insulin to rats and rabbits. The new rectangular design improves the electrical efficiency and increases the spatial average intensity at the surface of the skin.

Measured TVR and VA/Watt ratios show that the 3x1 rectangular array is an improvement over the 3x3 circular design with little increase in array size. Depending on the desired frequency of operation, the rectangular arrays can be up to two times more eff cient. This can translate into an increase in battery life for a portable device.

In conclusion, the rectangular array is electrically more e±cient than the circular design and increases the insulin delivery rate by way of an increased spatial average intensity. These results show promise for the use of the rectangular cymbals in the portable ultrasonic system and larger animal studies will be conducted to begin to determine system requirements for human patients.

Acknowledgements

This work was supported by the Department of Defense Technologies for Metabolic Monitoring Award Number W81XWH-05-1-0617.

REFERENCES

[1]S. Mitragotri, J. Kost, "Low-frequency Sonophoresis: A Review," Advanced Drug Delivery Reviews, Vol. 55, Issue 5, March 2004

[2]A. Joshi, J. Raje, "Sonicated Transdermal Drug Transport," Journal of Conrolled Release, 83, 2002

[3]N.B. Smith, R.E. Newnham, J.W. Hughes,R.J. Meyer Jr., K.K. Shung, E. Maione, "Transducer Design for a Portable Ultrasound Enhanced Transdermal Drug-Delivery System", IEEE Transactions on Ultrasonics, Ferroelectrics and Frequency Control, Vol. 49, No. 10, 2002

[4]S. Lee, "Ultrasound-Mediated Transdermal Insulin Delivery and Glucose Measurement Using the Cymbal Array," PhD Thesis, The Pennsylvania State University, Department of Bioengineering, August 2004 [To be replaced by a paper reference]

[5]J.F. Tressler, R.E. Newnham, W.J. Hughes, "Capped ceramic underwater sound projector: The 'cymbal' transducer," Journal of the Acoustical Society of America, Vol. 105, No. 2, Pt. 1, February 1999

[6]N.B. Smith, S. Lee, K.K. Shung, "Ultrasound-Mediated Transdermal In Vivo Transport of Insulin with Low-Profile Cymbal Arrays," Ultrasound in Medicine & Biology, Vol. 29, No. 8, 2003

[7]B. Snyder, "Design, Development, and Implementation of the 3x3 Cymbal Array for Transdermal Insulin Delivery," MS Thesis, The Pennsylvania State University, Department of Bioengineering, May 2004 [To be replaced by a paper reference]

[8]Newnham et. al., United States Patent 5,729,077, March 17, 1998

[9]IEEE Ultrasonics, Ferroelectrics, and Frequency Control Society, "IEEE Standard on Piezoelectricity", 1988

FIGURE CAPTIONS

1. (a) ATILA model of 1/8th of a single rectangular cymbal transducer (b) Contour plot of the axial displacement of the rectangular cymbal caps at 32 kHz

2. (a) A single element rectangular cymbal transducer (b) Comparison of a 3x3 circular and a 3x1 rectangular cymbal transducer array showing equivalent size

3. Contour plot of the axial displacement of the rectangular cymbal caps at 32 kHz

4. TVR comparison of a 3x1 rectangular and 3x3 circular array

5. (a) Untuned VA/Watt ratios of 3x1 rectangular and 3x3 circular cymbal arrays (b) Parallel tuned VA/Watt ratios of rectangular and circular cymbal arrays near 32 kHz

6. (a) Normalized intensity exposimetry of a 3x3 circular array in a plane 1 mm from the face of the transducer in dB showing a single spatial intensity peak (b) Normalized intensity exposimetry of a 3x1 rectangular array in a plane 1 mm from the face of the transducer in dB showing more uniform intensity distribution

7. Normalized change in glucose levels in 5 kg rabbits after ultrasonic insulin delivery experiments

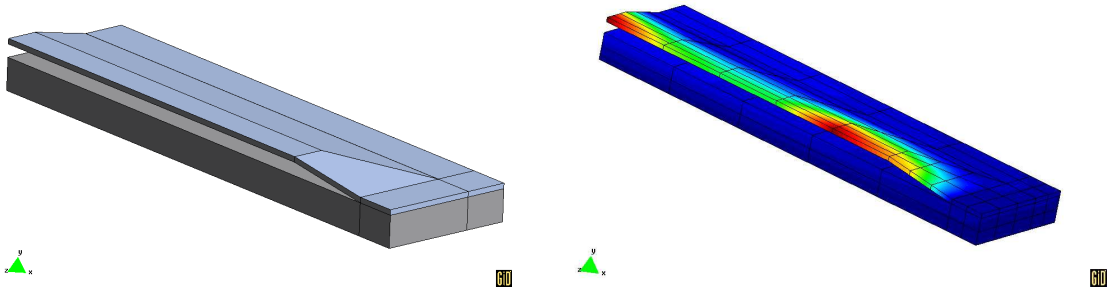

FIG. 1. (a) ATILA model of 1/8th of a single rectangular cymbal transducer (b) Contour plot of the axial displacement of the rectangular cymbal caps at 32 kHz

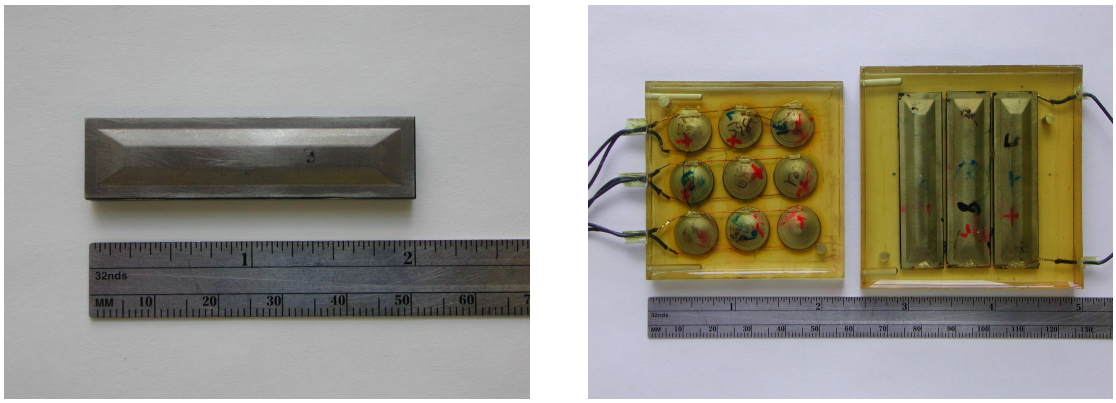

FIG. 2. (a) A single element rectangular cymbal transducer (b) Comparison of a 3x3 circular and a 3x1 rectangular cymbal transducer array showing equivalent size

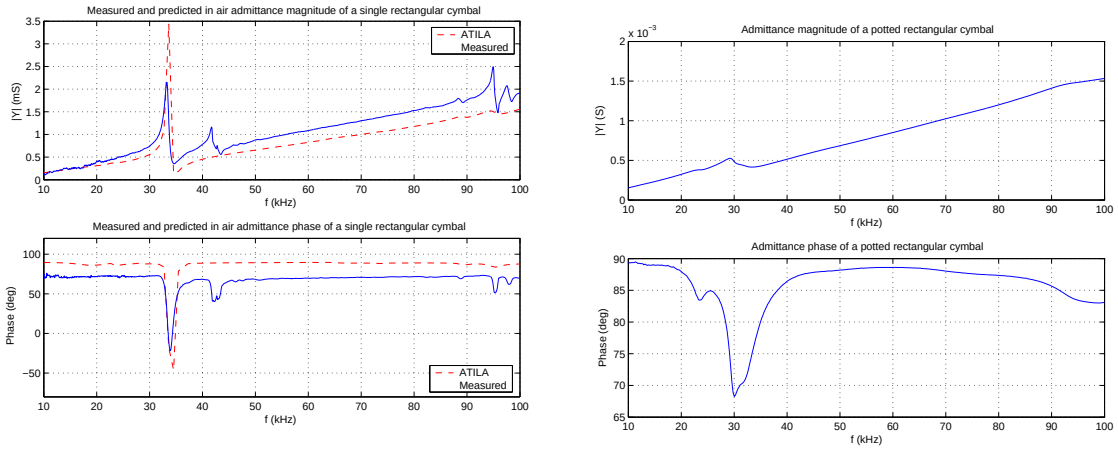

FIG. 3. (a) Measured and ATILA predicted admittance magnitude and phase of one rectangular cymbal transducer in air (b) Measured underwater admittance magnitude and phase of one rectangular cymbal transducer

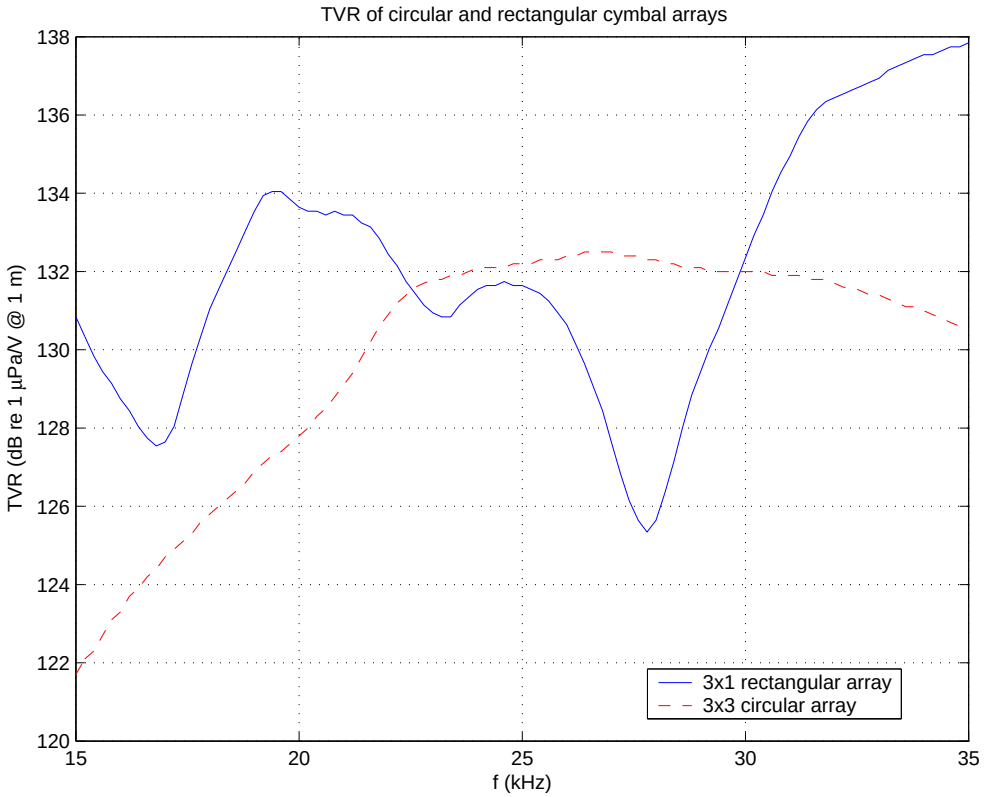

FIG. 4. TVR comparison of a 3x1 rectangular and 3x3 circular array

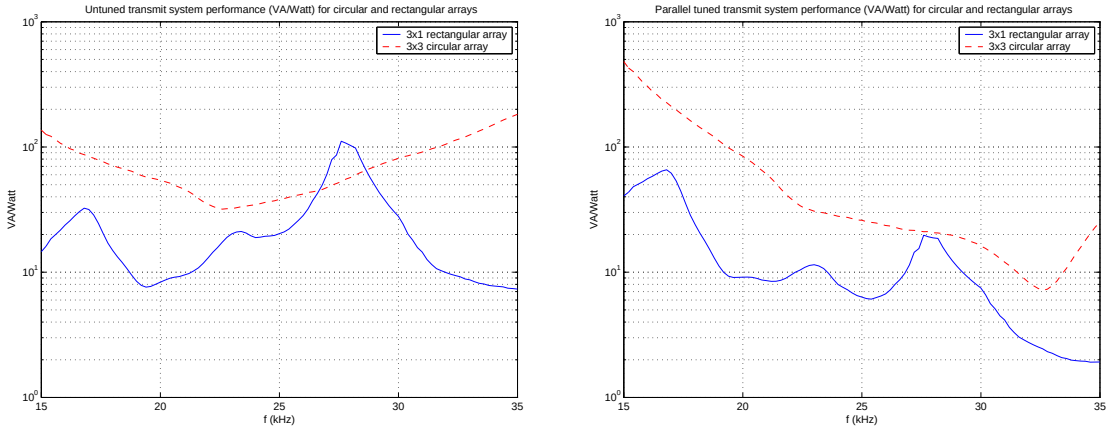

FIG. 5. (a) Untuned VA/Watt ratios of 3x1 rectangular and 3x3 circular cymbal arrays (b) Parallel tuned VA/Watt ratios of rectangular and circular cymbal arrays near 32 kHz

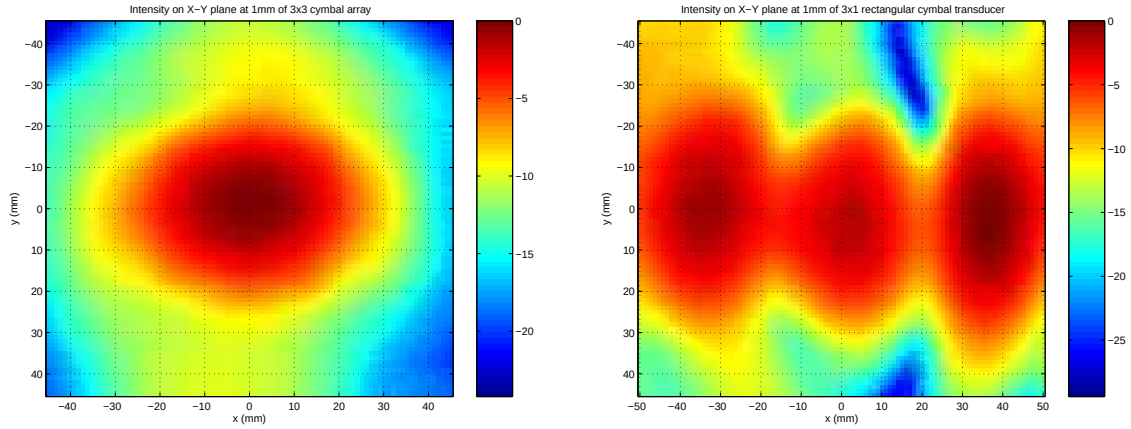

FIG. 6. (a) Normalized intensity exposimetry of a 3x3 circular array in a plane 1 mm from the face of the transducer in dB showing a single spatial intensity peak (b) Normalized intensity exposimetry of a 3x1 rectangular array in a plane 1 mm from the face of the transducer in dB showing more uniform intensity distribution

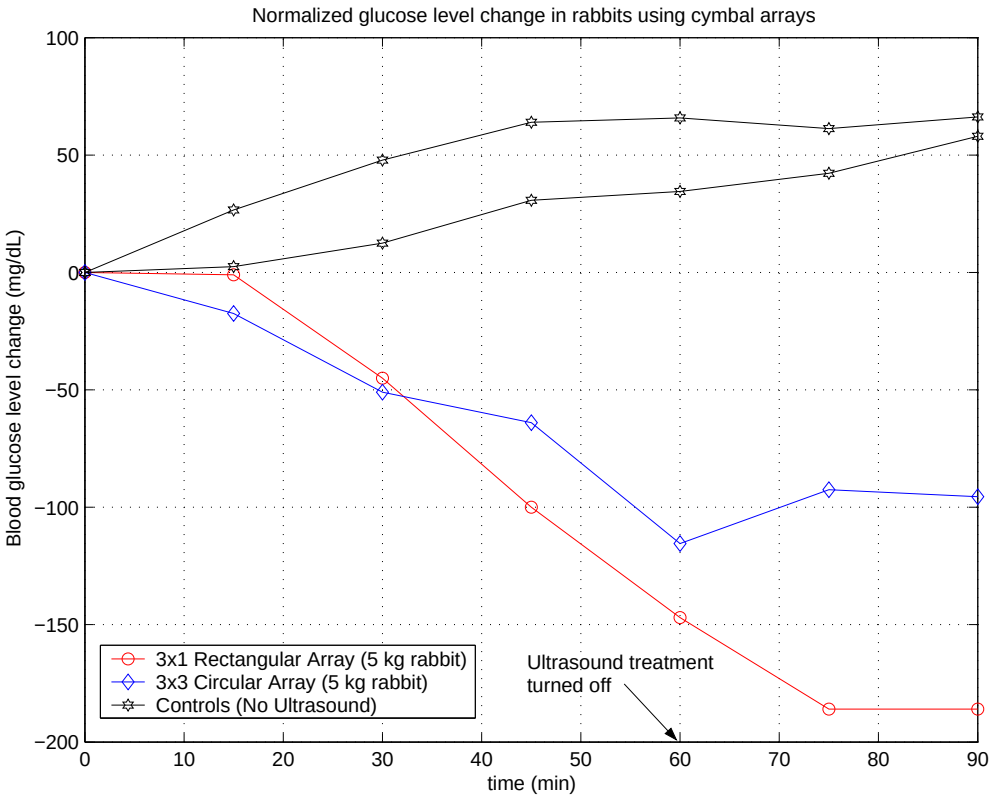

FIG. 7. Normalized change in glucose levels in 5 kg rabbits after ultrasonic insulin delivery experiments

Appendix III

The Pennsylvania State University

The Graduate School

College of Engineering

A "SMART" NONINVASIVE ULTRASOUND GLUCOSE MONITORING AND INSULIN DELIVERY SYSTEM

A Thesis in

Electrical Engineering

by

Vivekanand V Nayak

Submitted in Partial Fulfillment
of the Requirements
for the Degree of

Master of Science

I grant The Pennsylvania State University the non-exclusive right to use this work for the University's own purposes and to make single copies of the work available to the public on a not-for-profit basis if copies are not otherwise available.

_____

Vivekanand V Nayak

The Thesis of Vivekanand V Nayak was reviewed and approved* by the following:

Nadine Barrie Smith
Thesis Adviser
Associate Professor of Bioengineering

Lynn Carpenter
Associate Professor of Electrical Engineering

Kenneth Jenkins
Professor of Electrical Engineering
Head of the Department of Electrical Engineering

*Signatures are on file in the Graduate School.
We approve the thesis of Vivekanand V Nayak

Date of Signature

_____ _____

Nadine Barrie Smith
Thesis Adviser
Associate Professor of Bioengineering

_____ _____

Lynn Carpenter
Associate Professor of Electrical Engineering

_____ _____

Kenneth Jenkins
Professor of Electrical Engineering
Head of the Department of Electrical Engineering

ABSTRACT

Ultrasound enhanced transdermal drug delivery offers advantages over traditional injection drug delivery methods that are invasive and painful. The dermal interstitial fluid glucose concentration is highly correlated with the plasma glucose concentration. Thus, transdermal extraction of interstitial fluid offers a noninvasive method of obtaining a sample for blood glucose measurement. Combining the above two systems into a "smart" feedback control system using a controller will provide a continuous glucose measurement and insulin delivery system, to prevent hypoglycemia and hyperglycemia states in a diabetic person. Recent studies have shown that a low profile two by two ultrasound array based on the cymbal transducer when integrated with a π-type impedance matching network produces ultrasound at 20 kHz of 100 mW/cm^2 intensity that can be used to conduct experiments to demonstrate ultrasound mediated noninvasive transdermal insulin delivery in hyperglycemic rabbits. Experiments conducted by previous researchers using the cymbal array have demonstrated that the blood glucose level decreased by 208.1± 29 mg/dL for 60 minutes of ultrasound exposure of 100 mW/cm^2 and of duty cycle 20% in hyperglycemic rabbits. For this research, enzyme based glucose biosensors were used with the cymbal array to enhance skin permeability and conduct continuous glucose monitoring. Hyperglycemic rats were exposed to ultrasound for 60 minutes and the glucose sensor was placed on the exposed skin and current was measured using a potentiostat. The concentration of the glucose was measured using a calibration curve and compared with the reading obtained using an ACCU-CHEK^{TM} blood glucose monitoring system to check for consistency. Finally the feedback controller to integrate the insulin delivery and glucose monitoring system was

developed based on the proportional integral derivative (PID) algorithm. The simulation model controls the glucose concentration level within the desired level of 70-170 mg/dL with an error of ± 5%.

TABLE OF CONTENTS

LIST OF FIGURES

LIST OF TABLES

Acknowledgements

I wish to express my gratitude to my thesis advisor, Dr. Nadine Smith, for her patience, guidance and encouragement throughout the course of this research. I would also like to thank my thesis committee members Dr. Kenneth Jenkins and Dr. Lynn Carpenter for their advice and suggestions. I would like to extend my appreciation to my present and previous colleagues in the Therapeutic ultrasound laboratory. And last but not the least, I would also like to express my regards to my family and friends.

This work was supported by the Department of Defense Technologies for Metabolic Monitoring Award Number W81XWH-05-1-0617.

Chapter 1
Introduction

Ultrasound enhanced transdermal drug delivery offers advantages over traditional injection drug delivery methods, which are invasive and painful. Currently few drugs, proteins or peptides have been successfully administered transdermally for clinical applications because of the low skin permeability to these relatively large molecules. This low permeability is attributed to the stratum corneum, the outermost skin layer. One hypothesis indicates that once the drug has traversed the stratum corneum, the next layer is easier to cross and subsequently the drug can reach the capillary vessels to be absorbed. Recent developments in the area of transdermally drug delivery offers hope to millions of diabetics that someday they will be able to treat their disease without painful injections or needle sticks [1].

A number of different techniques for monitoring blood glucose using non or minimally invasive methods are under investigation including near infrared spectroscopy, implantable glucose sensors, reverse sonophoresis, reverse iontophoresis and interstitial fluid sampling devices [2]. The latter three techniques extract glucose transdermally and measure glucose concentration in interstitial fluid. Since dermal interstitial fluid glucose concentration is highly correlated with the plasma glucose concentration and capillary blood glucose concentration, transdermal extraction of interstitial fluid offers a noninvasive method of obtaining a sample for blood glucose measurements [3].

Noninvasive insulin delivery system and a glucose sensor system in conjunction with the feedback controller can be used to develop a “smart” diabetes management system, which will enable continuous glucose monitoring and deliver insulin into the

body thus preventing hypoglycemic (low glucose concentration) and hyperglycemic (high glucose concentration) states.

1.1 Motivation

From the data provided by the surveys conducted by the American Diabetes Association and endorsed by the National Institutes of Health and the Centers for Disease Control and Prevention, total number of Americans with diabetes rose to an all-time high with an estimated 18.2 million people in 2002 which is almost 6.3 percent of the population. Diabetes continues to be the sixth leading cause of death in the United States (US). An estimated 13 million Americans have been diagnosed with this disease. About 5.2 million additional Americans have the disease but have not been diagnosed. Diabetes is the leading cause of blindness among adults aged between 20 and 74 due to diabetic retinopathy, which is a condition of weakening blood vessels of the retina. The risk for death among people with diabetes is about twice that of people without diabetes. Diabetes costs around $132 billion annually to the US economy [4].

Diabetes can be divided into two main categories. Type 1 diabetes is an autoimmune disease. An autoimmune disease results when the body's system for fighting infection (the immune system) turns against a part of the body. In this case, the immune system attacks the insulin-producing beta cells in the pancreas and destroys them. The pancreas then produces little or no insulin. Someone with type 1 diabetes needs to take insulin daily to live. When type 2 diabetes is diagnosed, the pancreas is usually producing enough insulin, but, for unknown reasons, the body cannot use the insulin effectively, a condition called insulin resistance. After several years, insulin production decreases. Today, most people who take insulin to manage diabetes inject the insulin with a needle

and syringe that delivers insulin just under the skin. Several other devices for taking insulin are available including the insulin patches, pumps and inhalers [5].

Conquering Diabetes, a research report from the Diabetes Research Group funded by the National Institutes of Health, specified overarching goals to potentially prevent, cure, treat and manage this disease [6]. Specifically among these research challenges are methods to optimize glucose control. The recommendations include:" Increase basic and clinical research to discover novel approaches to controlling hyperglycemia in diabetes. These approaches should include developing technologies that enable administration of insulin by routes other than injection." One methodology is to use ultrasound for noninvasively mediating the transport of insulin across the skin.

1.2 Research Objectives

Three goals needed to be achieved for the research project. First the importance of applying an impedance matching network in the system to enhance the noninvasive ultrasound mediated transdermal transport of insulin using a low profile cymbal transducer array is studied. A π-type impedance network is used in this case to analyze the performance of the system. The following figure displays the system setup using the impedance matching network.

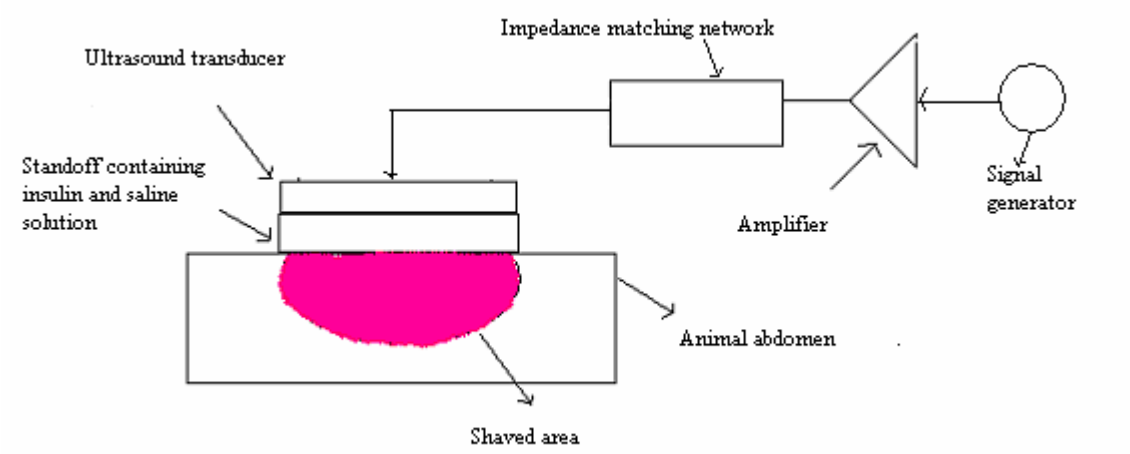

Figure 1.1 Array setup on the animal for in vivo experiments. The reservoir containing the saline solution and the insulin is placed on the shaved portion of the animal skin and then the transducer is attached to the reservoir. The transducer is connected to the impedance matching network and the amplifier for enhanced performance.

Secondly, a continuous noninvasive glucose monitoring system using screen-printed electrode sensors is developed. The results obtained from these glucose sensors is compared from that obtained by using invasive type glucose sensor developed by ACCUCHECK®. The system setup is shown below in Figure 1.2.

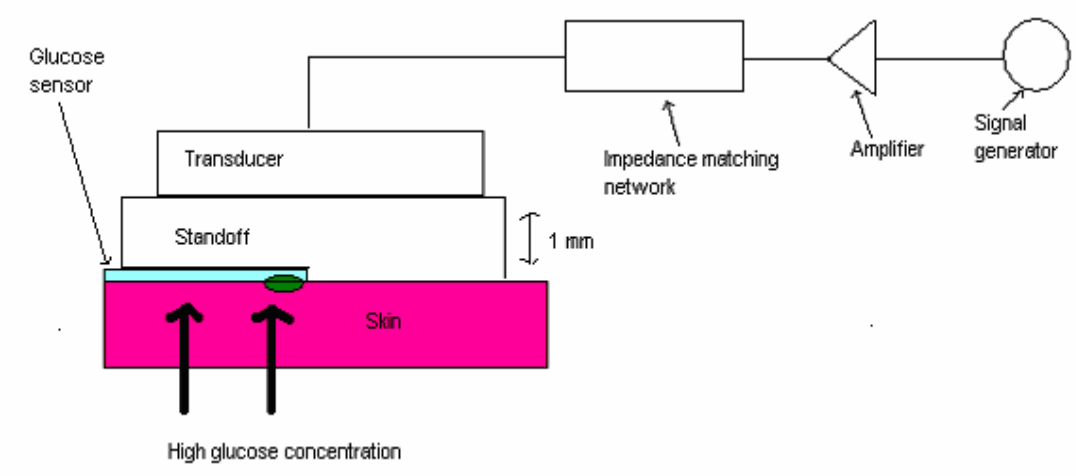

Figure 1.2 Glucose sensor setup on the ultrasound exposed area of the animal skin is shown with the standoff containing saline solution.

Finally the above two systems are integrated using a feedback controller to form a "smart" system for controlled diabetes management as shown in Figure 1.3. The

controller receives signal corresponding to the glucose concentration level in the interstitial fluid and send output signals to the insulin delivery system corresponding to the amount of insulin to be delivered.

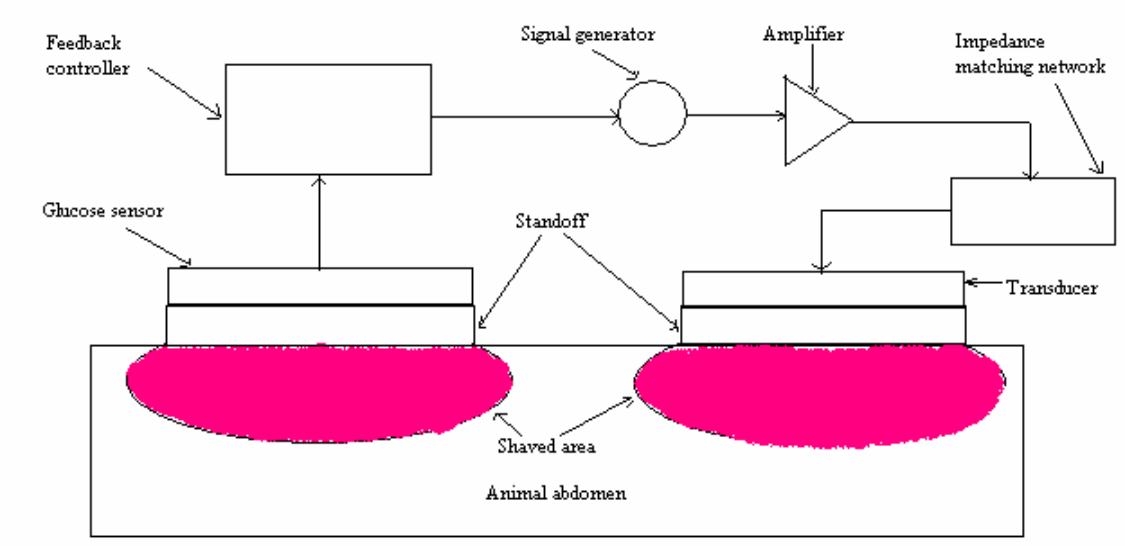

Figure 1.3 The insulin delivery system and the glucose sensor systems are integrated using a feedback controller to constitute a “smart” controlled diabetes management system.

Figure1.4 presents an overall picture of a portable system envisioned for the future.

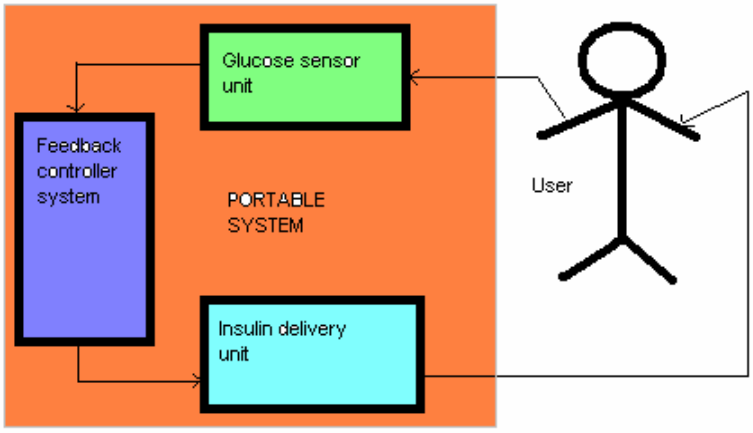

Figure 1.4 A closed loop control for implementing a smart glucose monitoring and insulin delivery system.

As shown in Figure 1.4, the three core modules of the system namely, the insulin delivery system, the glucose monitoring system and the feedback controller which integrates the first two systems are the goals to be achieved for the research project.

1.3 Thesis Outline

Chapter 2 reviews the ultrasound physics and the biological effects caused by high frequency ultrasound. It explains the components including the impedance matching network, cymbal array, the glucose sensor and the feedback controller used in the experimental setup. The description of the experimental set up used and the design process of each component used in the setup follows in the next chapter. Results obtained from the experiments conducted by introducing the impedance matching network in the experimental setup of ultrasound mediated transdermal insulin delivery and the noninvasive continuous glucose monitoring and simulation results of the feedback controller system are presented in Chapter 4. Finally the thesis report is concluded and future work needed in the topic of research is suggested.

Chapter 2
Theory

This chapter reviews the ultrasound physics and the ways in which ultrasound can be generated. The process of piezoelectric effect is explained in detail. Biological effects of ultrasound and the cavitational mechanisms are reviewed. A brief description of the electroacoustic transducers and the impedance matching network followed by the feedback controllers is given. Finally conventional and controlled diabetes management techniques are compared.

2.1 Ultrasound physics

Ultrasound is a sound wave having frequency higher than 20 kHz. Since ultrasound is a wave, it can be described in terms of the wave parameters including pressure, density, temperature and particle displacement. Ultrasound transmits energy when it travels through a medium other than vacuum. To understand how sound propagates through a medium, a three dimensional structure of spheres is considered. The spheres represent molecules, which are separated by springs perfectly elastic in nature. The springs here represent the forces between the particles. When a driving force is applied on any one sphere, this in turn gets transmitted to the adjacent sphere and so on and causes a chain reaction. The nature of the particle motion depends on the nature of the driving force. The movement of the spheres is the particle velocity whereas the sound propagation velocity is called as phased velocity. In case of a sinusoidal sound wave propagating in a liquid, regions of rarefaction and compression are produced in the medium. In case of compression, direction of phase velocity and the particle velocity is same while it is opposite in case of rarefaction [7].

A wave is a self-sustaining propagation at constant velocity of a disturbance without change of space. All acoustic processes are in general isentropic i.e. adiabatic and reversible. For perfect gases, a simple relation of its adiabatic describes the acoustic behavior given by

$$P/P_0 = (\rho/\rho_0)^{\gamma} \qquad (2.1.1)$$

where γ is the ratio of the specific heats and ρ and ρ_0 are the acoustic densities at a certain temperature and absolute temperature respectively having units in gm/cm^3 and P and P_0 are the corresponding pressures having units in Pascal [8].

For fluids other than perfect gases, the adiabatic is more complicated and is represented as a Taylor's expansion as follows

$$P = P_0 + \left(\frac{\partial P}{\partial \rho}\right)_{\rho_0} (\rho - \rho_0) + \frac{1}{2}\left(\frac{\partial^2 P}{\partial \rho^2}\right)_{\rho_0} (\rho - \rho_0)^2 + \ldots\ldots \qquad (2.1.2)$$

For small fluctuations in $(\rho - \rho_0)$, the above relation reduces to

$$P - P_0 = B\,(\rho - \rho_0)/\rho_0 \qquad (2.1.3)$$

with $B = \rho_0\left(\frac{\partial P}{\partial \rho}\right)_{\rho_0}$, the adiabatic bulk modulus having units of pressure.

In terms of acoustic pressure, P and condensation, s we have

$$P = Bs \qquad (2.1.4)$$

The equation of continuity, which relates the motion of a fluid with its compression or expansion, is given by $\frac{\partial \rho}{\partial t} + \nabla.(\rho \vec{u}) = 0$ (2.1.5)

where ∇^2 is $\frac{\partial^2}{\partial x^2} + \frac{\partial^2}{\partial y^2} + \frac{\partial^2}{\partial z^2}$ termed as the Laplacian operator.

For acoustic processes of small amplitude, the Euler's equation is given by

$$\rho_0 \frac{\partial \vec{u}}{\partial t} = -\nabla.P \qquad (2.1.6)$$

From equations (2.1.4), (2.1.5) and (2.1.6) we get the linear wave equation as

$$\nabla.\left(\rho_0 \frac{\partial \vec{u}}{\partial t}\right) = -\nabla^2 P \qquad (2.1.7)$$

Eliminating the divergence terms we have

$$\nabla^2 P = \rho_0 \frac{\partial^2 s}{\partial t^2} \qquad (2.1.8)$$

which is reduced to

$$\nabla^2 P = \frac{1}{c^2} \frac{\partial^2 P}{\partial t^2} \qquad (2.1.9)$$

where c is the thermodynamic speed of sound in m/sec and is defined by

$$c^2 = B/\rho_0 \qquad (2.1.10)$$

Equation (2.1.9) is also called as the linear, lossless wave equation for the propagation of sound in fluids with phase speed c. It represents a hyperbolic, second order and time dependent partial differential which models the transient movements of the sound waves [7].

2.2 Ultrasound generation and piezoelectric effect

Ultrasound can be generated in three ways namely piezoelectricity, laser generation and magnetostriction [9]. The mode of generation in case of cymbal transducers used in the research is through piezoelectric effect. Ultrasound transducers convert acoustic energy to electrical signals or electrical signals to acoustic energy acting as receivers or transmitters. When a force is applied perpendicular to the faces of a quartz crystal, an electrical charge is generated. This charge when amplified can be used as an electrical signal. If the same electrical signal is applied to the crystal, the crystal will vibrate and thus produce a sound wave into the medium. This is called as the piezoelectric effect and is used in medical ultrasound devices.

To explain the piezoelectric effect, individual molecules making up a crystal are considered. Each molecule in the crystal has a polarization where one end is more positively charged and the other is more negatively charged and thus making up a dipole. The polar axis is an imaginary

line that runs through the center of both the charges on the molecule. In case of mono crystal the polar axes of all the dipoles point in one direction. In a polycrystal, the polar axis of each molecule might lie in different regions so in order to produce the piezoelectric effect, the polycrystal is heated under the application of a strong electric field. Thus, heat allows the molecules to move freely and the dipoles in the crystal are forced by the electric field to line up and point towards the same direction. This crystal will exhibit piezoelectric effect. If the material is compressed then a voltage of the same polarity as the poling voltage will appear across two electrodes connected across the material. If the material is stressed, then voltage of opposite polarity is produced. If an ac signal is applied then the material vibrates at the same frequency as the signal. Development of piezoelectric composite materials has proved to be one of the most promising frontiers in transducer technology [10]. Lead zirconate titanate (PZT), a composite of lead zirconate and lead titanate are more suited for transducer technology applications.

2.3 Attenuation and biological effects of ultrasound

As ultrasound beams travels through the tissue, its amplitude and intensity are reduced as a function of distance the wave travels and frequency of the ultrasound wave. There are two sources of attenuation on the tissues namely reflection and scattering at the interfaces and absorption. In case of the absorption, the acoustic energy is converted to heat energy. Attenuation in soft tissues highly depends on frequency of the ultrasound signal. In most cases it is directly proportional to the frequency [11].

When sound passes through a medium it causes acceleration and displacement of the particles in the medium. Ultrasound beams of sufficient intensity can modify and even damage biological tissues. Depending on the acoustical exposure, the effect might be a small temperature elevation or complete destruction of the tissue [12]. Effects due to ultrasound treatment can be

classified into two broad categories, heating and non-thermal effects also known as mechanical effects. In case of heating, as sound beam propagates through tissue it gets attenuated and a significant fraction of this attenuation is due to conversion of the ultrasonic energy into heat energy. For low ultrasonic power levels this heat is dissipated and hence the heat produced does not offer any measurable rise in temperature. But in cases where the ultrasound device produces beams with areas of several square centimeters and higher and having spatial average time average intensities of 1000 mW/cm^2, significant rise of tissue temperature can be caused [12], [13].

In case of mechanical effects the sound waves have an ability to produce a biological effect without a significant degree of heating. There are two general classes of such mechanism namely cavitational and non-cavitational that may arise during exposure of a biological material to ultrasound. Cavitational processes occur in the presence of gas bodies while non-cavitational in the absence. 'Gas body' refers to any volume of gas or vapor that is nearly or completely surrounded by a liquid (like blood) or a solid (like tissue) or both and can be acted upon by an acoustic field.

2.4 Cavitational mechanisms and cavitation surface effects of low frequency ultrasound

The gas bodies required for cavitation are classified into three categories on the basis of how they are introduced into the body including the ones present naturally in the body or produced in the body from pre-existing cavitation nuclei within the body by the passage of an acoustic wave of sufficient intensity or produced by an external process and subsequently introduced into the body. A bubble that is composed of highly compressible gas in a sound field when acted upon by

the acoustic stress at its surface produces oscillations in the bubble volume. The amplitude of the radial oscillations is proportional to the acoustic pressure amplitude at low pressure and the mechanisms by which a bubble may affect nearby biological material are dependent on the magnitude of its response to the acoustic field. Almost all bubbles produce acoustic radiation forces and microstreaming while only the more strongly affected will exhibit the violent responses [5].

Two types of cavitation exist namely stable cavitation which is creation of bubbles that oscillate with the sound beam as mentioned before and transient cavitation which is a process in which the oscillations grow so strong that the bubbles collapse producing very intense localized effects.

Oscillating bubbles in a sound field produce a small-scale vigorous circulatory motion in the surrounding fluid. Such fluid motion is called a microstreaming. Since the velocity of the fluid flowing around the bubble is greatest near the bubble surface and since the fluid velocity decreases as distance from the bubble increases, a gradient exists in the fluid flow field around the bubble. When a cell is carried by the streaming flow into a region of strong fluid velocity gradients, the fluid will exert greater force on the side farther away. This unequal distribution of forces on the exterior of the cell results in shearing stresses that tend to distort and tear the cellular membrane. Because cells exhibit viscoelasticity, some minimum time is required for a given level of shear stress to disrupt a membrane [13].

Low frequency ultrasound of frequency from 20-40 kHz has been shown to increase the permeability of skin to certain molecules like insulin by 1000 times [14]. At this frequency ultrasound visibly deforms the surface of the skin on which it is incident. This is caused due to transient cavitation, which causes oscillations in the liquid medium and thus spontaneous

collapse of the gas bubbles when pressure waves are passed through them. This collapse near the surface causes the formation of a micro jet, which develops a force driving the insulin molecules across the skin surface.

2.5 Electroacoustic transducers based on piezoelectricity

An electroacoustic transducer converts electrical energy into sound energy, or vice versa. When the transducer is used to generate sound waves in a medium, it is called as a sound projector, transmitter (underwater) or speaker (air). Conversely, when it is used to detect sound, it is called a hydrophone (underwater) or microphone (air). Figure 2.1 summarizes the different types of transducers used over a broad range of frequencies.

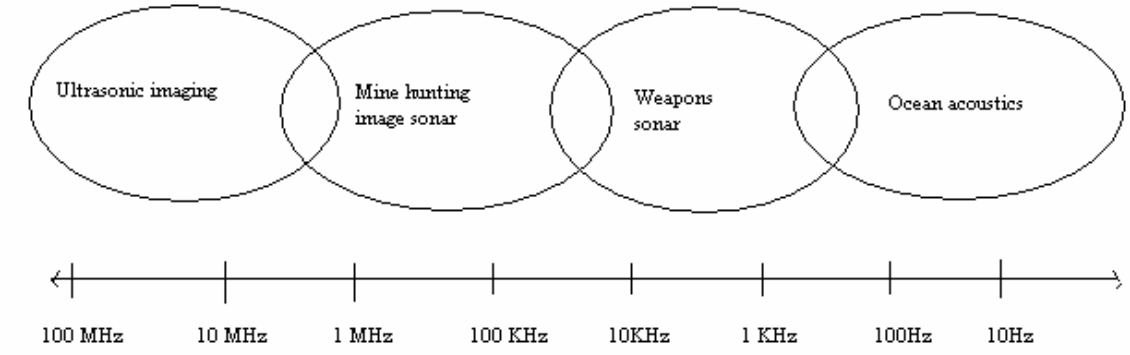

Figure 2.1 Transducers for different acoustic frequency range.

Flextensional transducers, which are used as low frequency resonators, use the flexural motion of the metal shells in contrast to the flexural disks, which use flexural motion of the ceramic. In flexural disk transducers, the ceramic disks are subject to tensile stresses during operation, which restricts the driving level since ceramics are fragile under tension. In the case of flextensional transducers the ceramics are pre-stressed and they are always under compression.

Therefore the flextensional transducers can be driven harder and hence are more reliable [15]. Flextensional transducers consist of an active piezoelectric or magnetostrictive drive element and a mechanical shell structure. The shell is used as a mechanical transformer, which transforms the high impedance, small extensional motion of the ceramic into low impedance, large flexural motion of the shell.

Since 1950s, flextensional transducers have been modified into many new designs. According to the shape and size of the shell, the flextensional transducers can be identified into five classes, Class I-V shown in Figure 2.2 [16]. Later more classes were added to the list and are shown as Class VI-VII. The cymbal is a Class V flextensional transducer according to its shape and possesses a compact, lightweight structure with a resonance frequency adjustable between 1-100 kHz. It was named “cymbal” because of the similarity in shape of its cap to that of the musical instrument. The cymbal was originally designed as an actuator but later proposed in as an underwater sound projector [15].

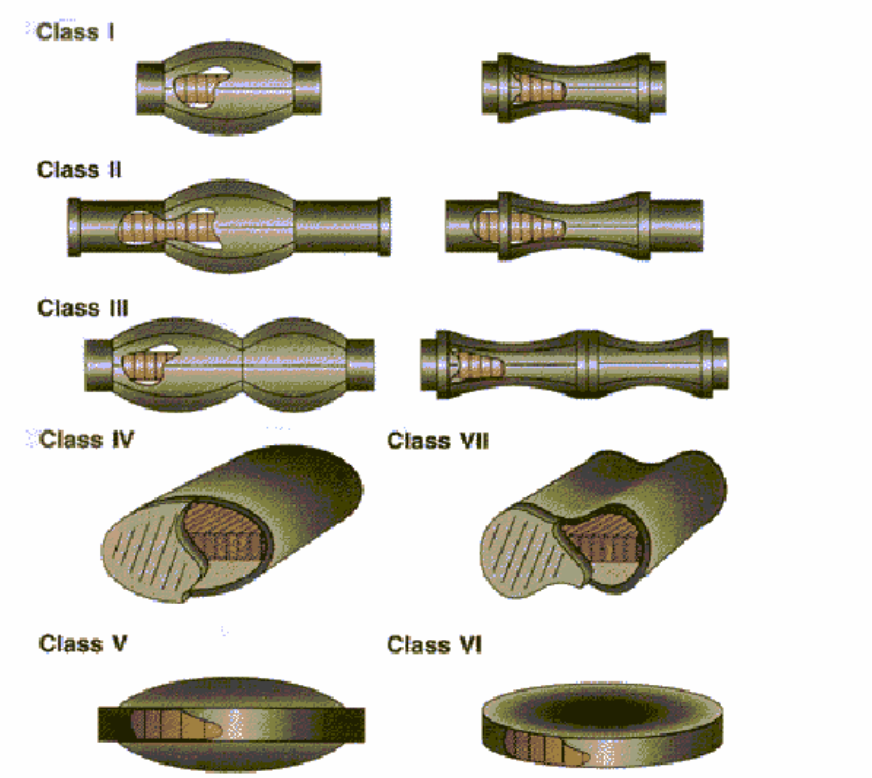

Figure 2.2 Different classes of flextensional transducers available presently.

A cymbal transducer can be represented in lumped elements as shown below

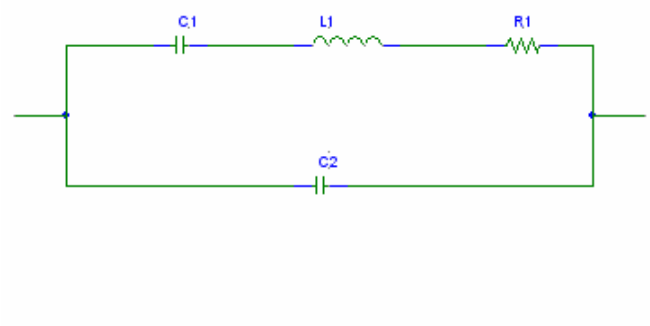

Figure 2.3 Equivalent circuit model of the cymbal transducer.

In Figure 2.3, C1 is the motional capacitance in Farad (F) and C2 is the clamped capacitance in F. The corresponding values for the electrical parameters are: C1 = 2.02 nF; C2 = 9.9 nF; L1, inductance = 8.25 mH; and, R1, resistance = 829.6 Ω [15].

The cymbal transducer is small compared to the wavelength in water around resonance and hence has a very low radiation resistance and a relatively high radiation reactance, which means that the transfer of radiated acoustic power from the surface of the radiator to the water is very

inefficient. Since the overall efficiency is the product of the radiation and mechanical transduction efficiencies, the cymbal's overall efficiency would also be very low, even if the mechanical transduction rate were very high. Hence it is necessary to assemble them into arrays to achieve the desired source level and directivity.

2.6 Impedance matching network

The arbitrary waveform generator (AWG) is designed to drive a characteristic impedance of 50Ω. This is the characteristic impedance of the output cable and allows the generator to deliver full power at maximum efficiency. If the output impedance varies from 50Ω the protection circuits in the AWG reduces the output power in order to protect the AWG from overload [17]. With the exception of dummy loads and some types of antenna most real world loads differ substantially from 50Ω and a device is needed to transform the output of the AWG to the actual load impedance of the system being driven. It is sometimes possible to use a conventional wound transformer, but most often the matching device is made up of a network of series and parallel impedances that combine to perform the transformation, i.e. an 'Impedance matching network'. There are several configurations of these in regular use and the selection of the right one is important.

The L-type network gets its name from the fact that it has two important tuning elements (the series connected capacitor C1 and inductor L1 count as one) and this network matches well to systems around the 5Ω region, and is able to cope with varying load capacitance. The main weakness of the L-type network is that the load resistance (or resistive part of series impedance) must be below 50Ω, preferably below 30Ω. It also requires an excessively large load capacitor to match loads below 4Ω [18]. Figure 2.4 shows a L-type impedance matching network used commonly.

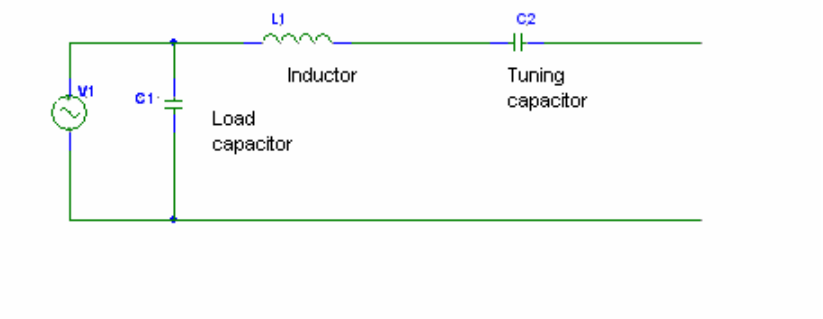

Figure 2.4 A L-type impedance matching network with L1 and C2 as the tuning elements and C1 as the loading capacitor.

The π-type network's name comes from the arrangement of the three impedances C1, C2, and L1 and is able to match impedances below and above 50Ω. Figure 2.5 shows a π-type impedance matching network used commonly.

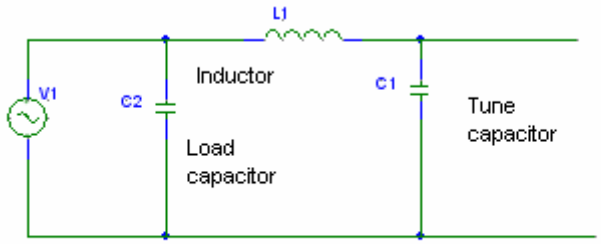

Fig 2.5 A π-type impedance matching network with L1 and C1 as the tuning elements and C2 as the load capacitor.

The T-network finds use where the load resistance is extremely low, even below 1Ω and is not able to cope with large variations in load capacitance, unless the inductor can be replaced or adjusted. One benefit of this network is that the bulk of the load current passes through the inductor and load capacitor but not through the tune capacitor. A T-network can achieve an RF match into its own circuit losses, risking severe overheating. Figure 2.6 shows a T- type impedance matching network.

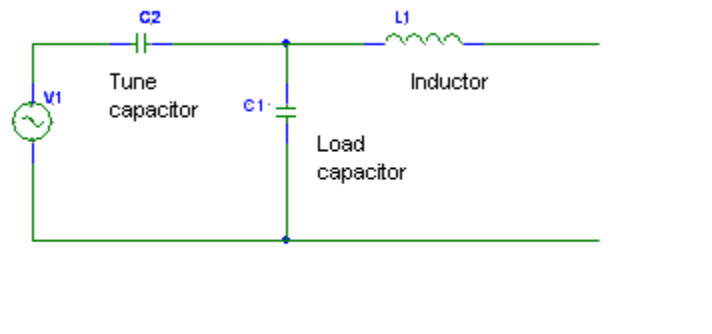

Figure 2.6 A T-type impedance matching network with L1 and C2 as the tuning elements and C1 as the load capacitor.

2.7 Mathematical analysis of the π-type impedance matching network

The π-type impedance matching network is shown below in Figure 2.7.

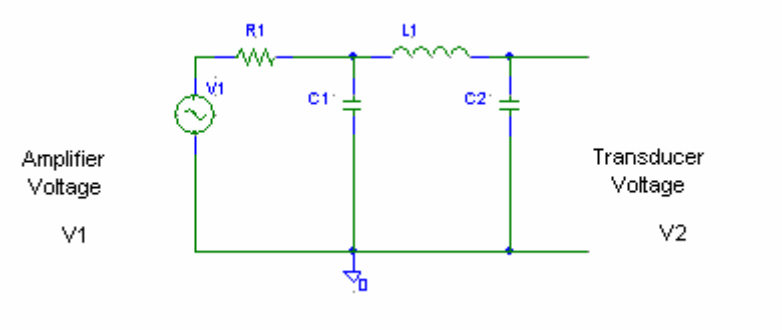

Figure 2.7 A low pass π-type impedance matching network with the input voltage to the network from the amplifier and the output to the transducer array. L, C1 and C2 are the components on the impedance matching network where the inductance is in mH and the capacitances are in nF. V1 and V2 are the amplifier output and transducer input voltage in volts respectively.

By doing a Laplacian analysis on the above circuit we get the equivalent impedance of the given circuit as

$$Z_{eq} = \left[\frac{\left(\frac{1}{sC2}+sL\right)\frac{1}{sC1}}{\left(\frac{1}{sC2}+sL\right)+\frac{1}{sC1}}\right]+R \qquad (2.7.1)$$

$$= \frac{s^2LC2+1}{s\left(s^2LC1C2+C1+C2\right)}+R \qquad (2.7.2)$$

where s is the Laplacian domain variable and Z_{eq} is the equivalent impedance of the network having units of ohms when viewed from the transducer voltage side.

As seen from the equation (2.7.2), the equivalent impedance has a real as well as imaginary component. At resonance frequency, the imaginary component of the equivalent impedance is equal to zero, which implies

$$1-4\pi^2 f^2 LC2=0 \qquad (2.7.3)$$

Hence, the resonating frequency for the impedance matching network is given by f where,

$$f= \frac{1}{2\pi\sqrt{LC2}} \qquad (2.7.4)$$

The gain of the above circuit is given as

$$\frac{V2(s)}{V1(s)} = \frac{1}{s\left(s^2 RLC1C2 + R\left(C1+C2\right) + sLC2\right)+1} \qquad (2.7.5)$$

where L is in mH and C1, C2 are in nF.

Now to determine the values for L, C1, and C2, we use the constraints of the resonating frequency of the matching circuit being equal to 20 kHz and the gain of the matching circuit combined with the amplifier in series should be able to give the required power level at the ultrasound. Using the first constraint we get an equation between L and C2. From the second constraint we get an equation between L, C1 and C2, which can be reduced to an equation between L and C1.Then we can take values for L and C1 to get the required frequency and the gain.

2.8 Glucose biosensors and the principle of Clark electrode

The history of biosensors started in the year 1962 with the development of enzyme electrodes. The definition of a biosensor changes with the application. A biosensor is defined as," a chemical sensing device in which a biologically derived recognition entity is coupled to a transducer, to allow the quantitative development of some complex biochemical parameter" [19].

The name biosensor implies that the device comprises of a bio-element and a sensor element. The bio-element may be an enzyme, antibody, antigen, living cells, tissues, etc whereas the sensor element can be electric current, electric potential, conductance, impedance or temperature. The basic concepts of biosensor can be illustrated using the following Figure 2.8 [20].

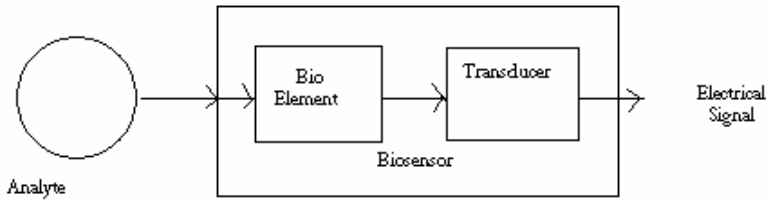

Figure 2.8 A basic biosensor structure having an analyte and a sensor bio-element which transduces the change in the bio molecule into an electrical signal.

As shown, a specific bio-element recognizes a specific analyte and the sensor element transduces the change in the bio-molecule into electrical signal. The bio-element needs to be very specific to the analyte to prevent it from being sensitive to any thing else.

Measuring the concentration of blood glucose is essential in diagnosing and for long-term management of diabetes. Glucose is the main circulating carbohydrate in the body. In normal, fasting individuals, the concentration of glucose in blood is very tightly regulated usually between 80 and 90 mg/dL, during the first hour or so following a meal. The hormone insulin, which is normally produced by beta cells in the pancreas, promotes glucose transport into skeletal muscle and adipose tissue. If the glucose concentrations exceed the normal range then the diabetic condition is reached. Glucose biosensors have been developed which detects the

glucose concentration in blood or interstitial fluids and generate a current, which is related to the concentration level [19].

Almost all of today's glucose sensors use the principle of Clark electrode and the enzyme glucose oxidase. The Clark electrode consists of platinum metal coated with glucose oxidase, an enzyme extracted from cows. As blood diffuses across the biological membranes, any glucose present in the blood reacts with glucose oxidase and is broken down into gluconic acid and hydrogen peroxide. The hydrogen peroxide then reacts with the platinum electrode and releases one electron for every molecule of glucose. Also the oxygen dissolved in the surrounding fluid reacts with the gluconic acid produced to regenerate the glucose oxidase, which is ready to react once more with glucose. Thus the enzyme breaks down glucose forming hydrogen peroxide as a by-product. As the peroxide reacts with the metal it produces a current that is proportional to the concentration of glucose in the blood. The current is then converted into a glucose concentration [21].

The equations given below depict the electro-chemical reactions of Clark electrode used for glucose sensing.

$$\text{Glucose} + O_2 \xrightarrow{\text{Glucose oxidase}} H_2O_2 + \text{gluconic acid} \qquad (2.8.1)$$

$$H_2O_2 \xrightarrow{Pt} 2e^- + O_2 + 2H^+. \qquad (2.8.2)$$

The main disadvantage of such sensors is their low sensitivity. The signals of the potentiometric glucose sensors are based on the Nernst equation, which gives a logarithmic dependence of the potential change on change in glucose concentration. This is sufficient in case of change in concentration in several orders of magnitude (as in case of pH measurements). In physiological fluids, however glucose concentration changes by no more than one order of magnitude, which makes the potential signal, obtained of very low magnitude.

2.9 Feedback Controller

Feedback control is the basic mechanism by which systems, whether mechanical, electrical, or biological, maintain their equilibrium or homeostasis. Feedback control may be defined as the use of difference signals, determined by comparing the actual values of system variables to their desired values, as a means of controlling a system [22]. An everyday example of a feedback control system is an automobile speed control, which uses the difference between the actual and the desired speed to vary the fuel flow rate. Figure 2.9 shows a basic feedback loop having a single input and a single output.

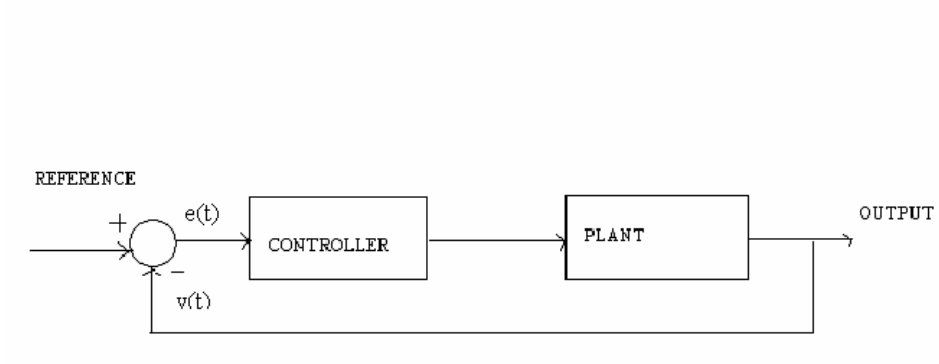

Figure 2.9 A basic feedback loop controlling the error generated in the plant.

As shown above in Figure 2.9, the output from the plant is fed back and compared with the desired level, which is the reference signal. The difference between the desired and the obtained signal is the error that is fed into the controller and is further processed depending on the nature of the controller used.

Several types of feedback loop controllers are available today based on different principles of which the proportional-integral-derivative (PID) algorithms are the most powerful ones. The PID algorithm is the most popular feedback controller used within the process industries. It has been successfully used for over 50 years. It is a robust easily understood algorithm that can provide excellent control performance despite the varied dynamic characteristics of process plant. The

PID algorithm consists of three basic modes, the proportional (P), the integral (I) and the derivative (D). Generally, three basic algorithms are used P, PI or PID [23]. With reference to the Figure 2.9, the controller algorithm is modified based on whether it is a proportional, proportional-derivative or proportional-derivative-integral control.

The mathematical representation for a proportional mode is,

$$\frac{v(s)}{e(s)} = k_c \text{ in Laplace domain} \qquad (2.9.1)$$

and

$$v(t) = v_{ss} + k_c e(t) \text{ in time domain} \qquad (2.9.2)$$

where v(t) is the output signal which needs to be controlled, e is the error signal and k_c is the controller gain.

The proportional mode adjusts the output signal in direct proportion to the controller input (which is the error signal, e). The adjustable parameter to be specified is the controller gain, k_c. The larger k_c the more the controller output will change for a given error. For instance, with a gain of 1 an error of 10% of scale will change the controller output by 10% of scale. The time domain expression also indicates that the controller requires calibration around the steady-state operating point. This is indicated by the constant term $v_{ss.}$ A proportional controller reduces error but does not eliminate it (unless the process has naturally integrating properties), i.e. an offset between the actual and desired value will normally exist.

The mathematical representation for a proportional integral mode is,

$$\frac{v(s)}{e(s)} = k_c \left(1 + \frac{1}{sT_i}\right) \text{ in Laplace domain} \qquad (2.9.3)$$

and

$$v(t)=v_{ss}+k_c\ [\ e(t) + \frac{1}{Ti}\ \int(e(t))\ ]\ \text{in time domain} \qquad (2.9.4)$$

The additional integral part (often referred to as reset) corrects for any offset (error) that may occur between the desired value (set point) and the process output automatically over time. The adjustable parameter to be specified is the integral time (T_i) of the controller having units of time.

Finally the mathematical representation for the proportional integral derivative mode is,

$$\frac{v(s)}{e(s)} = k_c\ (1+\frac{1}{sT_i}\ +T_Ds)\ \text{in Laplace domain} \qquad (2.9.5)$$

and

$$v(t)=v_{ss}+k_c\ [\ e(t) + \frac{1}{Ti}\ \int(e(t) + T_D\frac{de(t)}{dt})\ ]\text{in time domain} \qquad (2.9.6)$$

Derivative action (also called rate or pre-act) anticipates where the process is heading by looking at the rate of change of time of the controlled variable (its derivative). T_D is the 'rate time' and this characterizes the derivative action (with units of time). Derivative action depends on the slope of the error, unlike P and I. If the error is constant, derivative action has no effect.

2.10 Conventional and controlled diabetes management

Conventional therapy usually involves one to three daily injections that are the same every day. The types of insulin, number of injections and dose sizes are determined based on how much food is eaten, when it is eaten and how much activity has been there during the day. In conventional therapy, long acting insulin is used and the food intake is adjusted to fit in with the effects of the long acting insulin. The patient normally has to take six or seven calculated meals. But this therapy has some good points too including a smooth insulin activity curve. The advantage of giving two long acting insulin is that the peak of both the insulin profile occur at different times and at night time there is hardly any insulin activity which prevents hypoglycemia [4].

To prevent the rise in blood glucose sugar during the morning the patient will add long-acting insulin to a small amount of regular insulin. The addition of regular insulin to long-acting insulin is intended to ensure a more powerful insulin effect during the morning. Conventional insulin therapy requires fewer injections [24].

In case of conventional diabetes management, the timing and dose of insulin injections have to be adjusted to a variety of factors that influence the glucose level like carbohydrate intake, physical activity and rest and sleeping periods. In addition to being painful the glucose level estimation given by the glucose meters in such a therapy are just a snapshot of the glucose level at that particular instant which in no way predicts the past or future of the glucose level. If instead of conventional therapy, controlled therapy is used which will continuously monitor the glucose level and at the same time also predict the future glucose level taking into consideration the past value, then such a management system will definitely help in a smoother control of glucose level. A controlled diabetes management will work on an algorithm, which senses the glucose level continuously and determines the amount of insulin required taking into account the history of glucose insulin activity inside the body. Noninvasive techniques for sensing the glucose level and insulin delivery would be the best option in such a case where frequent measurements have to be made [25].

2.11 Controller design for automatic control of glucose concentration level

A closed-loop, controlled-feedback system that combines the noninvasive glucose monitoring and insulin delivery system, which will actively respond to peaks and valleys of the blood glucose and transfer the required amount of insulin thus acting as an ‘artificial pancreas’ has to be developed. Although insulin was first used for therapeutic purpose in 1922, diabetic patients still live in constant fear of over dosage or under dosage of their

medicines leading to consequent hyperglycemia and/or hypoglycemia episodes [26]. Control system design for the treatment of diabetes is a complex issue due to the varied scenarios that must be considered. Manual glucose monitoring and insulin injection involves the diabetic patient as an actuator and likelihood exists that the patient will deviate from expected behavior, either in terms of injection times and amounts, meals, or exercise. One of the problems with insulin therapy is insulin-induced hypoglycemia, which occurs when blood glucose level falls below the lower specified basal limit. The brain requires a certain minimum amount of glucose flux and only has reserves sufficient for at most a few minutes [27]. When glucose levels drop below the lower limit, neurophysiological deterioration can occur. In attempts to overcome hypoglycemia, the first defense is the suppression of glucose utilization, which may occur 2-2.5 hours after the onset of hypoglycemia. The factors affecting hypoglycemia and the dangerous results of this condition are important considerations for modeling and controller design.

The primary barrier to automated closed-loop control treatment of diabetes mellitus is the development of long-term reliable blood glucose sensors. It is difficult to achieve good glucose level control in diabetics. Continuous glucose monitoring can be used to detect fluctuations in blood glucose level over a prolonged period and thus indicate when the deviations occur from the normal range. The first step in this is to develop a noninvasive glucose sensor. This sensor will sense the glucose level after every 15 minutes and estimate this to a computer, a controller in this case, and then the insulin patch will pump out the amount of insulin corresponding to the glucose level deviation. Such systems could greatly simplify the life of insulin-dependent diabetics. The system should be able to sample, filter, and interpret the glucose sensor data, compare the reading with the allowable range and

accurately order just enough insulin to maintain normoglycemia and above all this process should operate at all times. But the way in which insulin dosage affects the glucose level varies from one person to another makes the system controller to be calibrated for each user. The system can also be used to sound a warning when the sensor or the insulin patch malfunctions and it must be reliable enough not to respond to random errors in sensor readings and at the same time be flexible enough to respond quickly to substantial insulin needs. This system will consist of three parts: the noninvasive ultrasound glucose sensor, a closed loop feedback controller and the transdermal ultrasound delivery setup.

Chapter 3
Experimental setup

This chapter describes the design of the various components used in the experimental setup for a "smart" noninvasive ultrasound mediated transdermal delivery of insulin and glucose monitoring including the cymbal transducer used in the array, the π-type impedance matching network, the glucose sensors and the feedback controller. Methods used to conduct in vivo experiments for insulin delivery and glucose monitoring are explained.

3.1 Design of cymbal transducer array

The design of the cymbal transducer integrates two metal caps epoxyed onto a lead zirconate-titanate (PZT) ceramic [1]. These caps create a shallow cavity beneath their inner surface and the ceramic. The fundamental mode of vibration is the flexing of the end caps caused by the radial motion of the ceramic [18]. Thereby, the overall displacement of the device is a combination of the axial motion of the disk plus the radial motion amplified by the end caps. These vibrations are depicted using the schematic given in Figure 3.1a. The cymbal specifically consists of a PZT-4 piezoelectric disk 12.7 mm diameter, 1 mm thick epoxyed between two titanium (Ti) metal caps (0.25 mm thick) and was designed to operate at a resonating frequency of 20 kHz. A cymbal transducer in finished form is shown in Figure 3.1b. PZT-4 was chosen because this material has a high failure voltage compared to ceramics with similar efficiency.

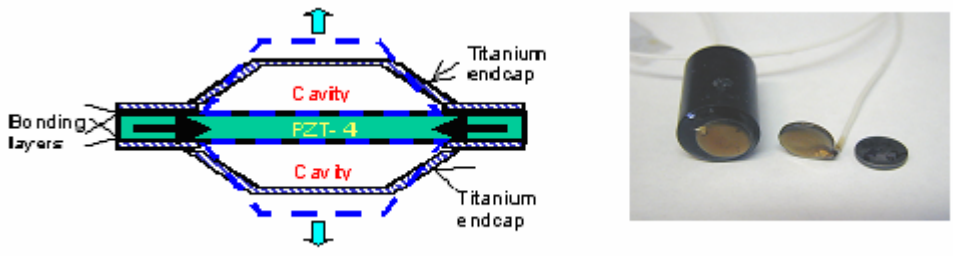

Figure 3.1 (a) The cross-sectional view and displacement motion of a cymbal flextensional transducer. (b) A cymbal element in finished form having a diameter of 12.7 mm used for the experiments conducted for the

research(rightmost), a cymbal element surrounded by a polymer(middle) and a complete cymbal transducer(leftmost).

Each cymbal transducer designed for the research purpose acted as a capacitor of capacitance 1.2 nF. Depending on the surface area of the skin required to be exposed, a two by two or three by three cymbal array is designed. For a two by two cymbal array, four cymbal transducers are connected in parallel and enclosed in URALITE® polymer [3]. This arrangement is in a 37 x 37 x 7 mm^3 block. For a three by three array, nine cymbal transducers are connected in parallel. If a two by two ultrasound array is designed then the four cymbal transducers are in parallel and the array acts as a single capacitance of 4.8 nF. For a three by three ultrasound array there are nine cymbals and the array acts as a capacitor of capacitance 10.8 nF. The sizes of a two by two array and a three by three array are compared to a quarter dollar coin using the Figures 3.2a and 3.2b.

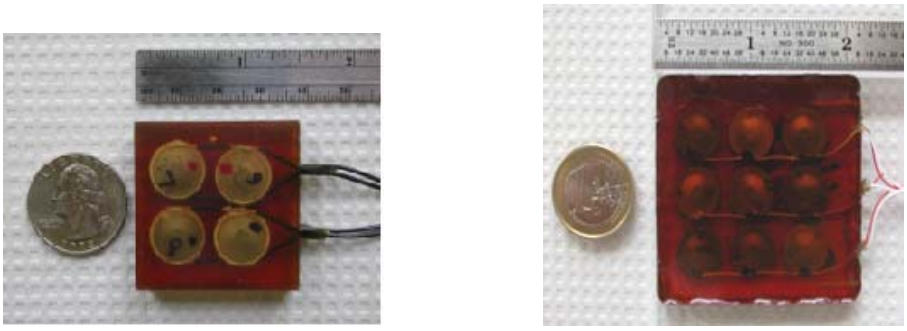

Figure 3.2 (a) A 2 x 2 cymbal transducer array used for the research purpose compared to the size of a quarter dollar coin. (b) A 3 x 3 cymbal transducer array used for the research purpose compared to the size of a quarter dollar coin.

3.2 Impedance matching and high frequency ferrite inductors

To increase the ultrasound intensity at the output of the ultrasound array, a matching circuit proposal was given. A low pass π-type impedance matching network was added between the amplifier output and the ultrasound array. Analysis of the matching network was done using the simulation software PSpice® (Cadence Design Systems, Inc., San Jose, CA). The components used in building the impedance matching network are described in the following sections.

The π-type impedance matching network used for the research is shown below in Figure 3.3.

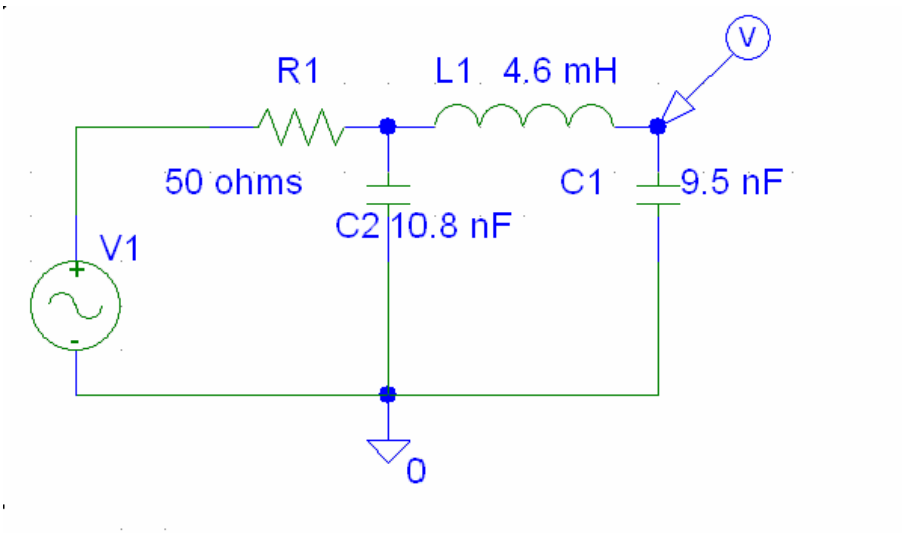

Figure 3.3 π-type impedance matching circuit used for the 2 x 2 cymbal transducer array. The capacitance of 9.5 nF is the external capacitance in parallel to the 2 x 2 cymbal array used.

Inductors used in the above impedance matching circuit had to operate at a high frequency of 20 kHz. At such high frequencies eddy current losses and hysterisis losses turn out to be high. The losses in the matching circuit would lead to lesser power at transducer output. To make the losses negligible ferrite cores were used due to their high resistivity. Pot core assembly was used to design the inductors [28]. Figure 3.4 describes the sub parts of a pot core assembly used in designing an inductor.

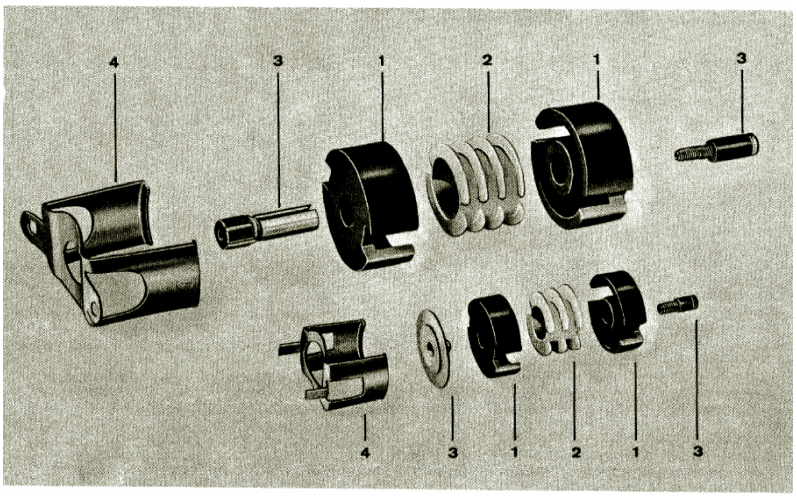

Figure 3.4 Sub parts of high ferrite inductor with the 2 matched pot core halves (1), bobbin on which the coils are wound (2), tuning assembly (3) and the clamp for holding the core halves together (4).

An example to describe the derivation of the inductance parameters is explained as follows. For designing an inductor of 8 mH, first the inductance factor A_L chart given in Appendix A, which has a range of A_L for different inductances for different core sizes is referred. Depending on the inductance core size required, a core of a given A_L with either one section or multiple sections is selected. From this, the number of turns required is calculated by using

$$N=1000\sqrt{\frac{L}{A_L}} \qquad (3.3.1)$$

where L is the inductance in mH. So if we select the core size of 18 mm by 11 mm (outer diameter by height) that has an A_L of 100, then the number of turns is 283. The bobbin area for the core is also available on the reference sheet. For the particular example the bobbin area is 0.17 cm^2 and the number of turns per bobbin area in cm^2 is 1665. Corresponding to the turns/area, the coil size of 27 AWG is selected. Inductor subparts manufactured by Magnetics® (Pittsburgh, PA) were used.

3.3 Experimental setup and ultrasound exposimetry system

The experimental setup for driving the cymbal array uses a RF amplifier (Model 25A250, Amplifier Research, Souderton, PA), a frequency pulse/function generator (Model 393, Wavetek Inc., San Diego, CA), an oscilloscope (Tektronix 2213A, Beaverton, OR), a cymbal transducer

array and a low pass π-type impedance matching network. For the in vitro experiments, the signal generator operated at 20 kHz, had a 1 V_{pp} (peak-to-peak) output with pulse duration of 200 ms and pulse repetition period of 1 second (i.e., 20% duty cycle) with the amplifier gain set to 50 dB. Pulse period, duty cycle and exposure time of the RF signal from the frequency generator was monitored using the oscilloscope [3]. Figure 3.5 shows the experimental setup mentioned above.

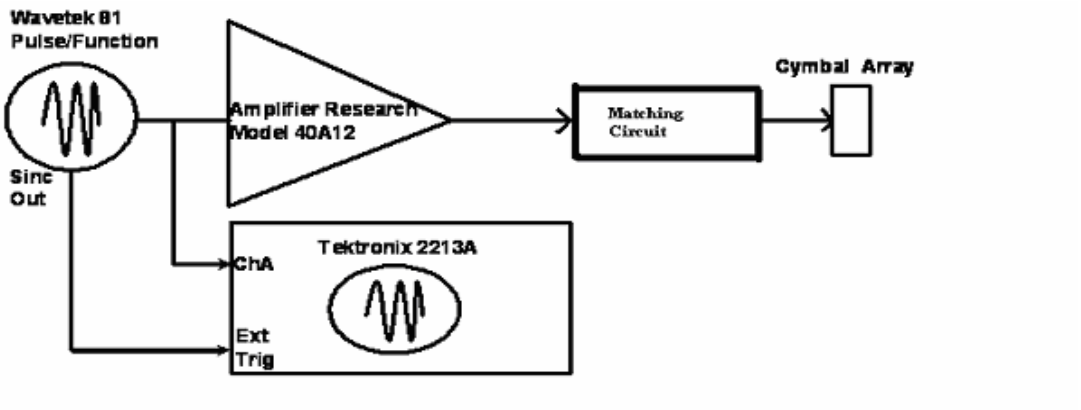

Figure 3.5 Experimental setup of the system driving the cymbal array comprising of the signal generator, the RF amplifier, the impedance matching circuit, the oscilloscope and the cymbal array.

Before the system is actually tested on animals, the exposimetry system shown in Figure 3.6 is used to derive the acoustic intensity of the cymbal transducer that will be applied for the in vivo experiments.

Figure 3.6 The computer controlled exposimetry system and electrical drive system for the 2 x 2 array utilized in measuring the spatial and temporal dependent power output of the array.

The ultrasound intensity is determined at a plane 1 mm from the transducer face by measuring the power output from the array using a calibrated miniature omni directional reference hydrophone (Model TC4013, RESON, Inc., Goleta, CA). The cymbal array was submerged in an anechoic water tank (51 x 54 x 122 cm^3). A custom made degasser, built in-house, reduced the dissolved oxygen content of the distilled water to 1-2 ppm to reduce cavitation effects. Precise, computer controlled positioning of the hydrophone was performed by a Velmex Positioning System (Velmex Inc., East Bloomfield, NY). An oscilloscope recorded pressure waves detected by the hydrophone. The scanning step size for each device was 1 mm and the scanning area was 20 x 20 mm^2. Spatial peak-temporal peak intensity (I_{sptp}) and spatial peak-pulse average (I_{sppa}) pressure were determined over a plane 1 mm from the array face. Based upon 3-5 independent scans of the array, a mean and standard deviation of the power output were calculated [3].

As discussed before in Chapter 2, section 2.4, low frequency ultrasound is effective in enhancing transdermal transport of insulin. The enhancement is determined by various parameters including the intensity, duty cycle and application time. The threshold energy was

found to be around 100 mW for rat skins. Below this threshold ultrasound energy the effect of skin conductivity cannot be detected. Beyond the threshold value the conductivity increases with the energy density [3].

The voltage at the hydrophone determines the ultrasound intensity at the hydrophone. The following relations described in [3] were used for this purpose.

(Pressure) = (Hydrophone Sensitivity) x (Voltage at the hydrophone)

$$P = HS \times V_H \quad (3.4.1)$$

$$= 39810 \times V_H \quad (3.4.2)$$

The ultrasound intensity I is given by

$$I = P^2/\rho c \ W/m^2 \quad (3.4.3)$$

ρc= 148000 kg/ m^2s in case water at 20°C. Hence,

$$I = P^2/1480000 \quad (3.4.4)$$

$$= P^2/14800000 \ mW/cm^2 \quad (3.4.5)$$

where ρ is the density of water in kg/ m^3 , c is the speed of sound in water in m/s, P is the acoustic pressure generated, HS is the hydrophone sensitivity and V_H is the voltage at the hydrophone terminal.

The quantity ρc is called as the acoustic impedance of the medium, which in this case is water and accounts for acoustic differences when the transducer is placed in differing media. The speed of sound in air is 344 m/s and 1500 m/s in water and the corresponding densities are 1.29 kg/m^3 and 1000 kg/m^3 respectively. Therefore, the acoustic impedance given by ρc for air is 420 kg/m^2s and 1,500,000 kg/m^2s for water, nearly 3600 times greater than air which explains the fact that it requires 3600 times more displacement in air than in water to achieve similar sound pressures. This demonstrates why transducers are more effective in water, or when they are coupled with an acoustic gel [16]. A voltage of 1 volt at the hydrophone gives P=39810 Pa and the ultrasound intensity as 100.07 mW/cm^2. Hence for an ultrasound intensity of 100 mW/cm^2, at least 1 volt at the hydrophone would be required.

3.4 In vivo transdermal insulin delivery experiment

Previous researchers have demonstrated in vivo transdermal insulin delivery in rabbits using the animal (rabbit) experimental protocol reviewed and approved by the Institutional Animal Care and Use Committee at the Pennsylvania State University. New Zealand White rabbits (3.0-3.4 kg) were divided into the three respective groups and 14 experiments were performed. The rabbits were anesthetized using ketamine (40 mg/kg) and xylazine (10 mg/kg), after which the hair on the thigh area was shaved. Xylazine was used to cause temporary but sustained (up to 12 hours) hyperglycemia in rabbits. After the rabbits were anesthetized, the average glucose level of the rabbits was 245.4 ± 45.5 mg/dL [28].

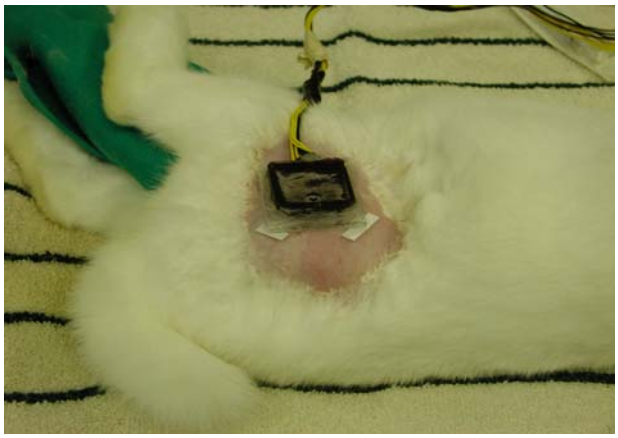

Figure 3.7 The 2 x 2 cymbal array for ultrasound exposure on the shaved part of the rabbit skin.

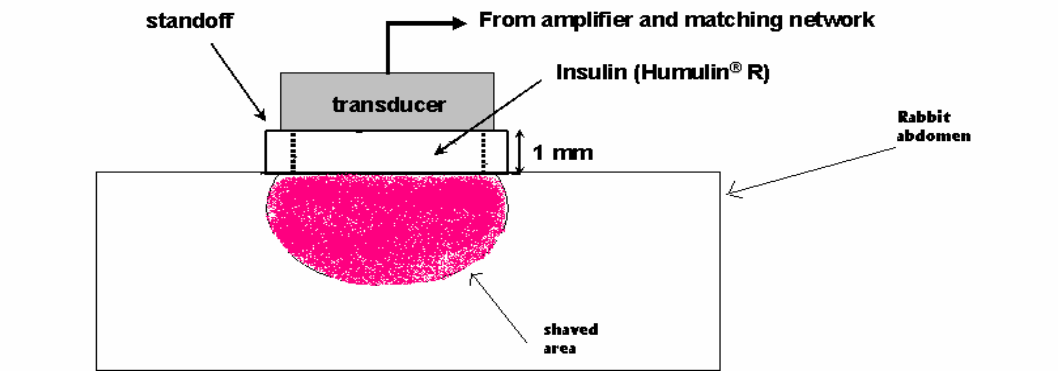

Figure 3.8 Array setup on the rabbit for in vivo experiments. The reservoir containing the saline solution and the insulin is placed on the shaved portion of the rabbit skin and then the transducer is attached to the reservoir.

With the rabbits placed in a lateral recumbent position, a 1 mm thick, watertight standoff was arranged between the skin and the array. The reservoir inside of the standoff was filled with saline or insulin (Humulin® R, 4 mL of 50 Units/mL) through holes in the back of the array. The first group (control 1, n = 5) had insulin in the reservoir with no ultrasound, while the second group (control 2, n = 3) had saline in the reservoir with ultrasound (US) operating at Isptp = 100 mW/cm^2 for 60 minutes. The third group (US and Insulin) was subjected to insulin with US exposure for 60 minutes (Isptp = 100 mW/cm^2) [28].

3.5 Glucose sensor fabrication

The screen-printed electrodes obtained from DuPont Electronic Technologies® (Research Triangle Park, NC) have three electrodes namely the working electrode, the reference electrode and the counter reference electrode as shown below in Figure 3.9.

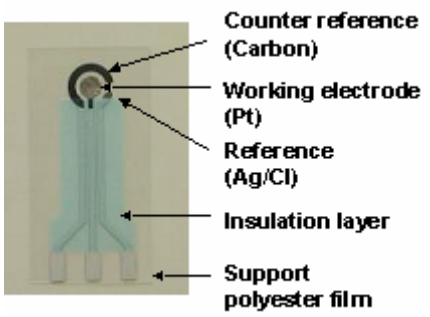

Figure 3.9 Components of a screen-printed electrode.

The working electrode was deposited with platinum, a catalyst for the hydrogen peroxide. 25 mM of platinic acid (Sigma-Aldrich Corp., St. Louis, MO) in 0.1 M NaCl solution were used for the platinization process. The platinization process using a potentiostat (Model 283, EG & G Instruments, Princeton Applied Research, TN) is used to transform the carbon coating on the working electrode into a platinum coated electrode.

The glucose oxidase (Sigma-Aldrich Corp., St. Louis, MO) of 5000, 000 unit/g was used for the purpose. This glucose oxidase was trapped in a gel form using polyethylene glycol (PEG) hydrogel. PEG diacrylate (MW = 575, Aldrich Corp., St. Louis, MO) was diluted with distilled water to make a 20% solution and then liquid photoinitiator (2-hydroxy-2-methyl-1-phenyl-1-propanone, Ciba Specialty Chemicals, Tarrytown, NY) and glucose oxidase were mixed using a mini vortexer machine (VWR Science product, PA) with the solution [28].

Figure 3.10 The vortexer machine is used to mix the gel and the glucose oxidase.

The electrodes were covered with the solution and exposed to ultraviolet light for solidifying the gel. The amount of gel added and the time for which it is exposed to ultraviolet light decides the post exposure hardness of the gel. Care needs to be taken that the gel layer is not too hard to avoid cracking during the use or too viscous to avoid spreading of the gel. Figure 3.11 shows the ultraviolet source machine that is used to expose the gel to ultraviolet light.

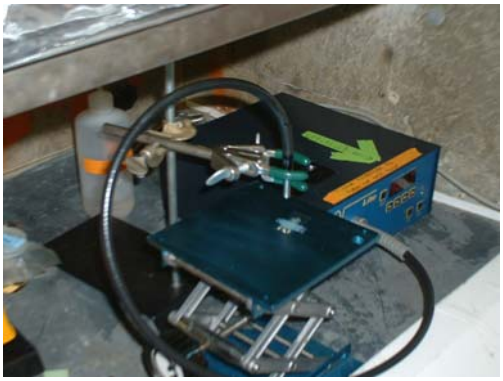

Figure 3.11 The ultraviolet source machine and the stand on which the glucose sensor is placed. A pipe as seen in the figure has its outlet facing the gel and the glucose oxidase mixture on the sensor to emit ultraviolet light.

3.6 In vivo glucose monitoring experiments

The low profile cymbal array with the impedance matching network developed for the research was used for demonstrating in vivo glucose monitoring in nine Sprague Dawley rats (300-400 gm) divided into two groups, seven rats in the ultrasound exposure and two rats in the control group(no ultrasound exposure). The rats were anesthetized using a combination of ketamine hydrochloride (60 mg/kg intramuscularly, Ketaject®, Phoenix, St. Joseph, MO, USA). The abdominal area of the rats was shaved using an electric shaver and a skin remover was applied to the shaved region for two minutes. After two minutes the shaved portion of the rat was cleaned and it was placed on the dorsal decubitus position with the cymbal array on its abdomen region as shown in Figure 3.12.

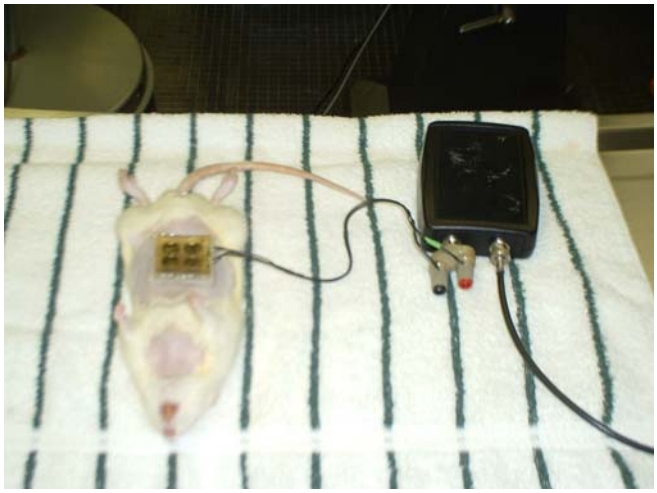

Figure 3.12 The cymbal array is attached to the rat and the impedance matching network. The matching network is connected to the amplifier on the other side (not visible in the picture).

The cymbal array had the watertight standoff attached for the saline solution. The ultrasound system was started for 20 minutes in case of control-grouped rats. The array was then removed and the glucose sensor was placed on the abdominal area of the rat, which was exposed to ultrasound as shown in Figure 3.13.

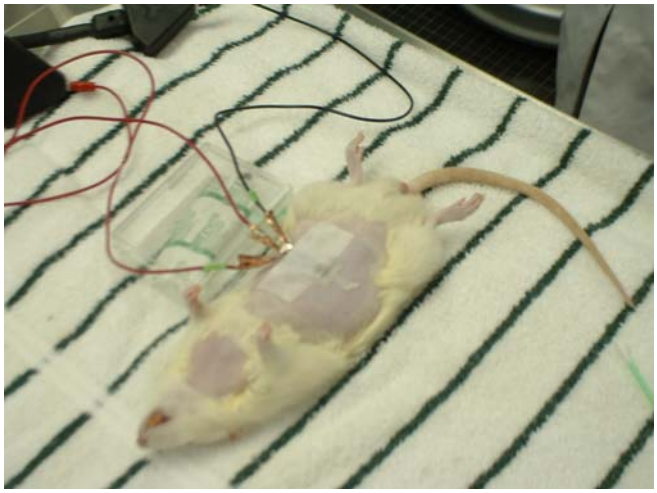

Figure 3.13 The glucose sensor attached to the ultrasound exposed area of the rat. The sensor has three electrodes that are connected to a potentiostat through three probes.

A detailed view of the glucose sensor position on the skin exposed to ultrasound is shown in Figure 3.14 below.

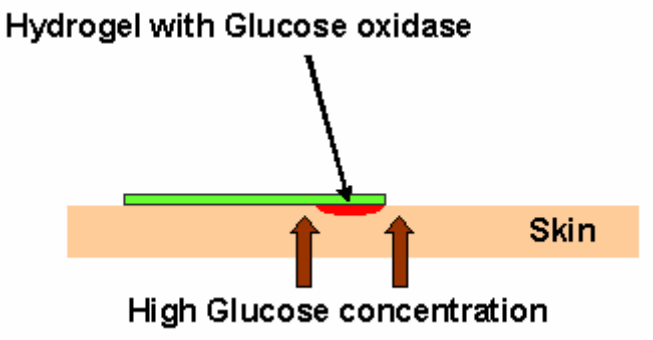

Fig 3.14 The glucose sensor is placed on the ultrasound exposed area of the skin with the face of the sensor containing the gel in contact with the skin.

The glucose sensor was kept in the position for 10 minutes and then the glucose test program was started in the potentiostat (Model 283, EG & G Instruments, Princeton Applied Research, TN) to measure the current between the working and the counter electrodes of the sensor. Using this current the glucose concentration in the interstitial fluid was determined from calibration curves developed for each sensor from known glucose concentration solutions. Also 0.3 mL of blood was collected from the rat and the glucose concentration was measured using ACCU-CHEK^{TM} blood glucose monitoring system (Roche Diagnostics Co., Indianapolis, IN). The error in the electrochemical biosensor was estimated by calculating the mean difference between the biosensor and glucose meter values.

3.7 Controller modeling

The objective of the feedback controller was to integrate the noninvasive insulin delivery and the glucose monitoring systems using a PID algorithm and thus maintain the glucose concentration level between 70-170 mg/dL. The feedback controller is designed on the basis of a simple rule: 'Insulin has an effect of reducing the glucose concentration level and in absence of insulin the glucose concentration level increases provided that the person has a means of increasing glucose level by eating food, etc.' But the main problem while implementing this rule is the variation in amount of insulin required, the time for which it

should be introduced and the rate at which it is introduced. All these factors play an important role in designing the feedback controller. To avoid any discrepancies, the data obtained by conducting ultrasound mediated insulin delivery using the low profile cymbal arrays on rabbits given in Figure 4.4 in Chapter 4, Section 4.2 is referred.

The results obtained indicate how the glucose concentration varies as the insulin amount and the exposure time are changed for the specific rabbits used for the experiment. In the experiment conducted, the exposure time was always maintained at 60 minutes. But when the glucose concentration level needs to be stabilized, exposure time will be changed. It is assumed that once the ultrasound exposure is started, it will be turned on for atleast 15 minutes. Different exposure times i.e. 15, 30, 45 and 60 minutes are used for the simulation model.

The table below gives the data used in designing the model. It has the four exposure times used and the reduction in glucose concentration level in mg/dL during the experiment for the different exposure times.

		Experiment time								
		0	15	30	45	60	75	90	105	120
Exposure time	60	0	0	15	25	30	25	15	5	0
	45	0	0	15	25	30	15	5	0	0
	30	0	0	15	15	5	0	0	0	0
	15	0	0	15	5	0	0	0	0	0

Exposure time (minutes)

Experiment time (minutes)

Reduction in glucose concentration level (mg/dL)

Table 3.1 The effect of external insulin on the glucose level when the ultrasound exposure is stopped after 60, 45, 30 and 15 minutes. The data for this table were taken from the results described in Chapter 4, section 4.2.

To explain the data presented in the above table, consider an example of exposing the rabbit with ultrasound for 60 minutes. As seen from the Table 3.1, there is a no reduction in the glucose concentration level at time equal to 0, which implies that the insulin effect has not started yet. This means that the insulin-glucose interaction is not instantaneous. After 15 minutes, the glucose concentration level has still not changed. Finally after 30 minutes there is a net reduction of 15 mg/dL of glucose level and of 25 mg/dL after 45 minutes. The ultrasound exposure is stopped after 60 minutes which causes a slow down in the drop of glucose concentration level, as ultrasound is no more aiding the insulin present in the standoff. The effect of insulin on glucose concentration level completely stops after 120 minutes. At this point if the rabbit is still hyperglycemic then a new insulin profile is started and the process is continued until a stabilized glucose concentration level is reached within the specified limits.

The first step in designing the model was to decide the normal basal limit, which was taken as a range from 70-170 mg/dL. To design the operation module of the feedback controller, the range of 70-170 was divided into 6 sections i.e. section A: 70-100, section B: 100-110, section C: 110-120, section D: 120-130, section E: 130-140 and section F: 140-170 as shown in Figure 3.15.

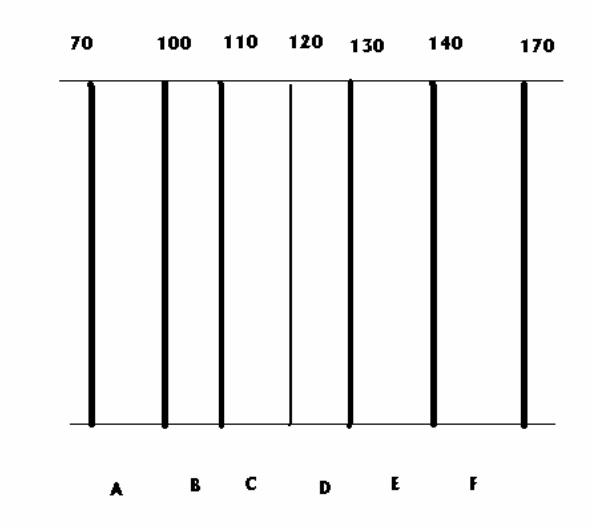

Figure 3.15 Glucose range used to customize the model so that the controlled glucose level is maintained between 70-170 mg/dL.

At any time if the signal is in region C or D, no action is required. When the signal is in region E then the rate of increase in the glucose concentration is measured. If it exceeds a specified value then the ultrasound exposure is started. If it is lesser than the specified value then no action is required. When the glucose signal is in region F then no matter what the rate of increase in glucose signal is, the ultrasound exposure is started. If the signal goes in region B then the signal's rate is checked and in case of higher rate, the ultrasound exposure is stopped. In case there was no ultrasound exposure when the glucose signal is in region B and the rate of decrease is more than the specified allowed limit then the user needs to have an external source of glucose (i.e. eat food). If the glucose signal is in region A, then in any case the user has to eat food to increase the glucose concentration level.

The model designed using MATLAB® 6.5.1 (MathWorks, Natick, MA) will alternate a switch from on to off and vice versa whenever the ultrasound system needs to be turned on or off. A custom-made glucose signal is taken which alternates between different levels outside the normal range. The model will track the glucose level based on the principles explained before and limit the glucose level between the desired normal range. The process will continue until

stabilized glucose concentration level is reached. Now the data assumed above will vary with the physiological condition of the subject. But since the change in the glucose level is normally very slow in the body, we can assume that the controller gets enough time to detect the change on the glucose level and take suitable action. Also the glucose sensor would be having a lag, which has to be taken in consideration for future work.

Chapter 4

Results

This chapter presents the results obtained by introducing the impedance matching network in the experimental setup for transdermal noninvasive insulin delivery for in vivo experiments using 2 x 2 array. Results obtained from noninvasive glucose monitoring using 2 x 2 array are presented in the second section and finally the simulation results for the feedback controller are provided in the final section.

4.1 Impedance matching network for 2 x 2 cymbal transducer array

As explained in Section 3.3, impedance matching circuits play an important role in feeding high power to the cymbal transducer array input. This statement is supported by the results obtained by applying voltage from the signal generator and measuring the voltage at the transducer. The following π-type circuit was used between the amplifier output and the transducer array input.

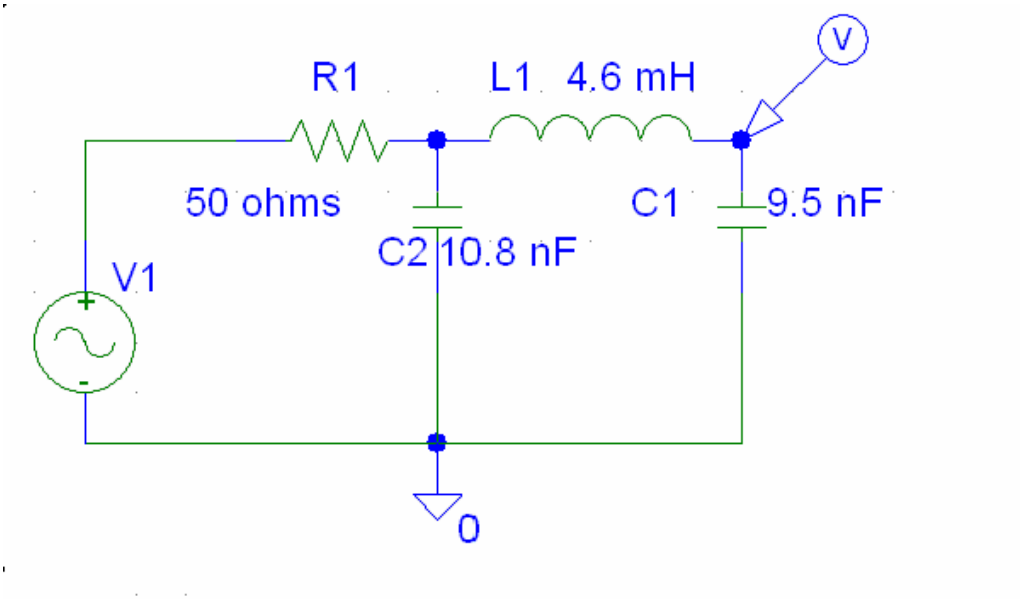

Figure 4.1 The π-type impedance matching circuit used for the 2 x 2 cymbal transducer array. The capacitance of 9.5 nF is the external capacitance in parallel to the 2 x 2 cymbal array used.

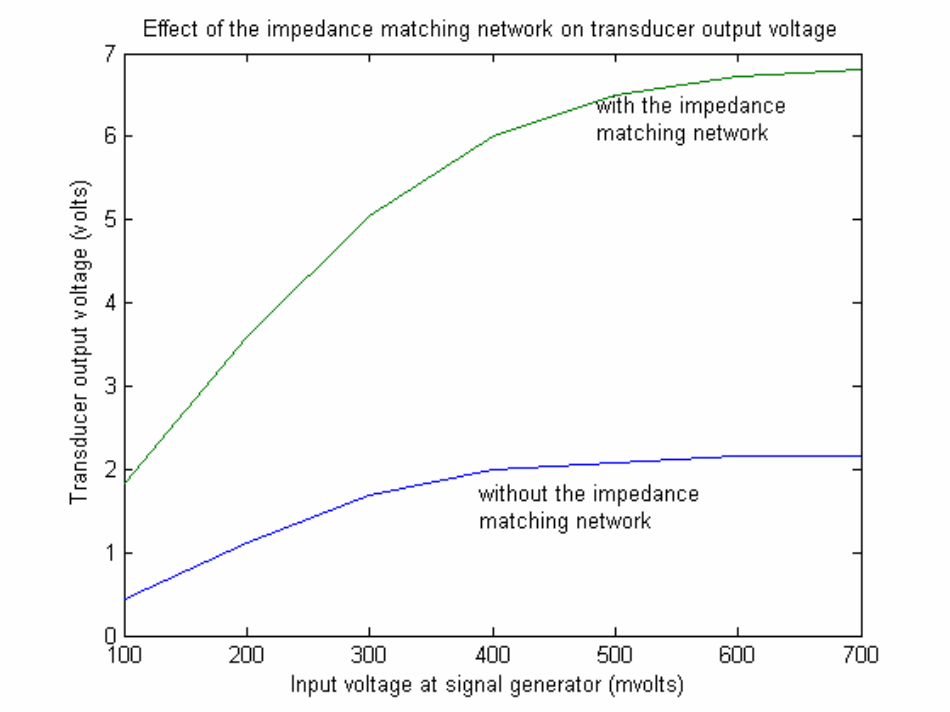

Figure 4.2 The effect of the impedance matching network on the transducer voltage for a given voltage from the signal generator.

As shown in Figure 4.2, the voltage obtained at the transducer increased by more than three times when an impedance matching network was introduced between the amplifier output and the transducer input terminals. Once the voltage amplification property of the impedance matching circuit was verified, exposimetry experiments were conducted as described in Section 3.3 to determine the ultrasound intensities at a plane 1 mm away from the cymbal transducer face. The experimental setup shown in Figure 3.5 was used for this purpose. The results for the ultrasound intensity obtained are summarized in the Figure 4.3 below.

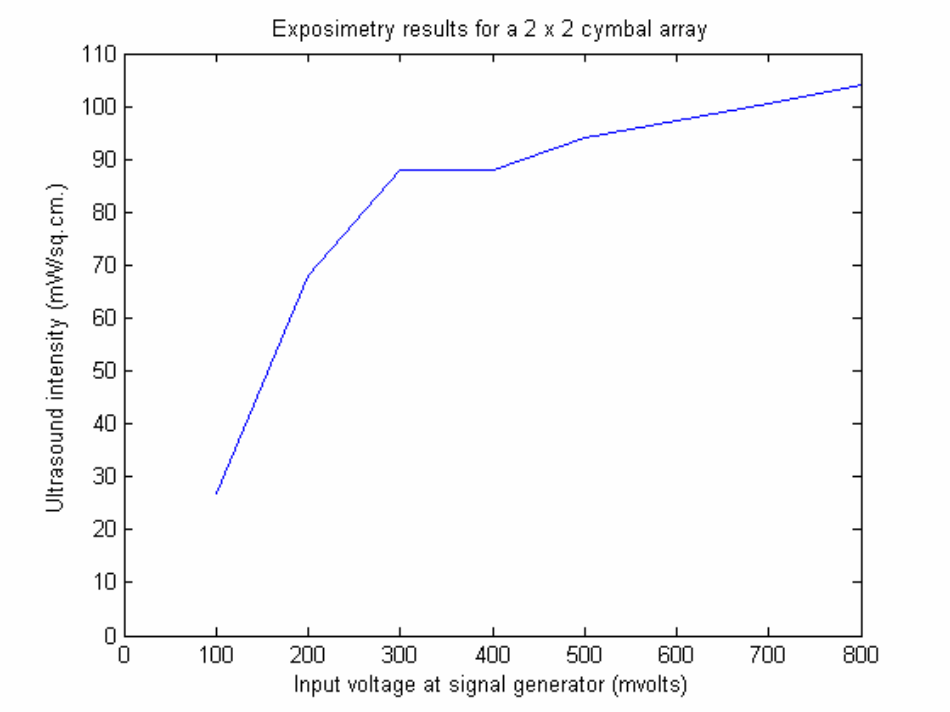

Figure 4.3 Exposimetry results for the 2 x 2 cymbal transducer array using the setup described in section 3.3.

As shown in Figure 4.3, as the voltage at the signal generator is increased linearly from 100 mV to 800 mV the ultrasound intensity increases nonlinearly once the input voltage is greater than 200 mV. For voltages greater than 800 mV at the signal generator, the ultrasound intensity increased at a slower rate and started to settle down at around 105 mW/cm^2. It is observed from Figure 4.3 that, to obtain an ultrasound intensity power of at least 100 mW/cm^2, an input voltage of 700 mV would be required at the signal generator. Hence, the experimental conditions for the animal tests included the signal generator operating at 20 kHz with a 700 mV (peak-peak) output, pulse duration of 200 msec and pulse repetition period of 1 sec (20% duty cycle). A low duty cycle was chosen to have minimum continuous ultrasound exposure and thus avoid any skin damage.

4.2 In vivo results for the transdermal ultrasound mediated insulin delivery

As explained in Section 3.4, three groups of rabbits were used in the experiment conducted by previous researchers [3]. Results obtained from the transdermal ultrasound mediated insulin delivery experiments are shown in Figure 4.4. During the 90 minutes of experimental time, the blood glucose level of the rabbits was shown to drop from its average value. After the rabbits were anesthetized, the average initial glucose level of the 16 rabbits was 245.4 ± 45.5 mg/dL. The average blood glucose level in normal rabbits is approximately 100-135 mg/dL [29]. The average initial glucose level of 245.4 ± 45.5 mg/dL was then taken as a baseline and the change in the blood glucose level was normalized to this baseline to analyze the results.

The glucose level measured was then graphed as its mean and standard deviation. For the first control group (insulin-no ultrasound), the glucose level increased 75.1 ± 36.8 mg/dL after 30 minutes and maintained its level over a 90 minute period. The glucose level of the second control group (saline w/ ultrasound) increased 47.9 ± 36.2 mg/dL after 30 minutes and remained at that level approximately. For the third control group (insulin-ultrasound), the glucose level decreased by -20.0 ± 20.8 mg/dL in 30 minutes and -132.6 ± 35.7 mg/dL in 60 minutes from the initial level. After the ultrasound was discontinued and the insulin reservoir was removed (i.e. at 60 minutes), the glucose level continued to decrease to -208.1 ± 29 mg/dL in 90 minutes. Visual examination of the post ultrasound exposed skin did not indicate any noticeable damage or significant change to the skin.

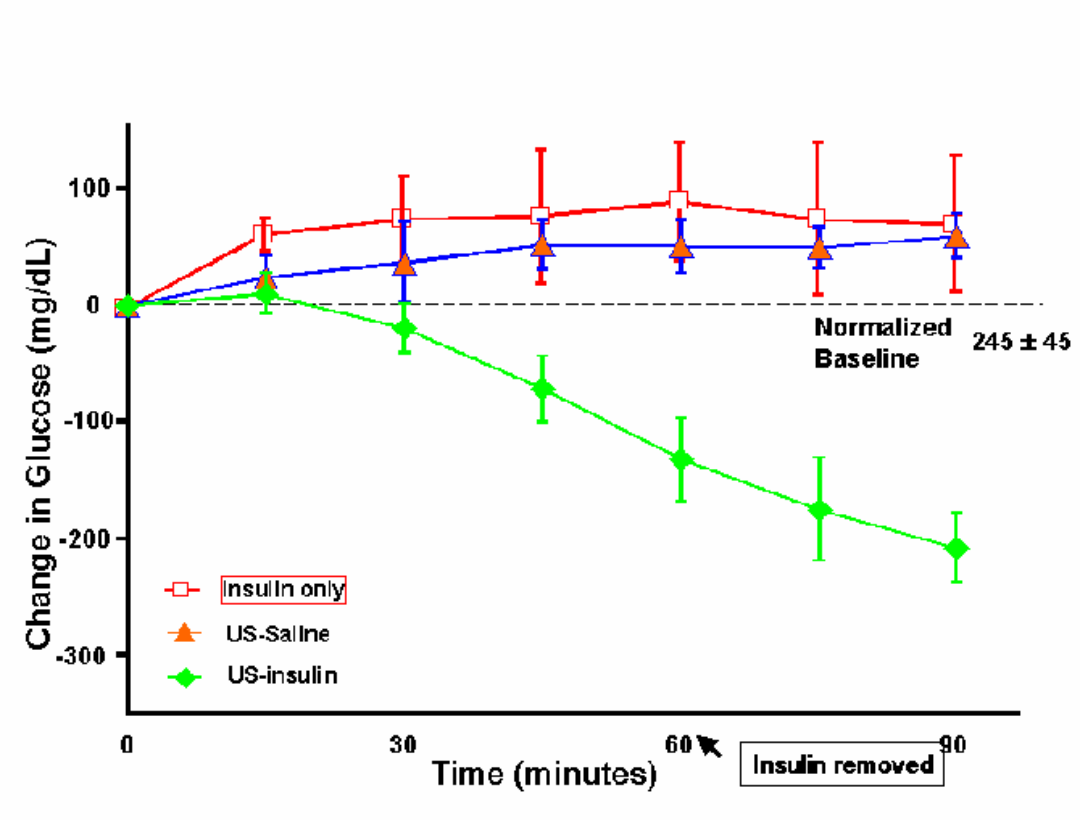

Figure 4.4 From N. B. Smith, S. Lee and K. K. Shung *et al.*, [3], over a period of 90 minutes, the blood glucose level of the rabbits decreased with ultrasound exposure (Isptp = 100 mW/cm^2) using the cymbal array. With 60 minutes of US exposure, the glucose level decreased to 208.1 mg/dL. Both Control 1 and 2 did not show any decrease of the blood glucose level.

4.3 In vivo results for glucose monitoring using 2 x 2 array

As explained in Section 3.6, the current between the working and the counter electrodes was measured using the potentiostat and the average value for a series of readings was taken. A group of known glucose concentration solution was taken and the current at the electrodes for each solution was measured again for the same sensor using the potentiostat. For the different current obtained for the different glucose concentration a calibration curve was plotted with the known glucose concentration on the x-axis and the current obtained at the y-axis. The average current obtained for this sensor using the potentiostat was 21.5 μA. From the calibration curve, the glucose concentration for this current is approximately 180 mg/dL. The blood glucose concentration in the rat was also measured using the ACCU-

CHEK™ blood glucose monitoring system (Roche Diagnostics Co., Indianapolis, IN). Multiple measurements were taken and the average was considered which was equal to 369 mg/dL in this case. The percentage error between the results for glucose concentration obtained from the glucose biosensors and the ACCU-CHEK™ blood glucose monitoring system was 46%.

To analyze the operation of the same sensor after an inactive period of two days, the same sensor was tested on a different rat. During these two days the sensor was stored in a flask containing distilled water. This is done to avoid dryness of the gel to prevent any cracking. The current between the electrodes was measured as explained above and the average current of 34.1 μA that corresponds to a glucose concentration of 504 mg/dL from the calibration curve was obtained. The blood glucose concentration obtained from the ACCU-CHEK™ system was 490 mg/dL that results in a percentage error of 2.81%. The calibration curve for the sensor obtained for both tests are presented in Figure 4.5.

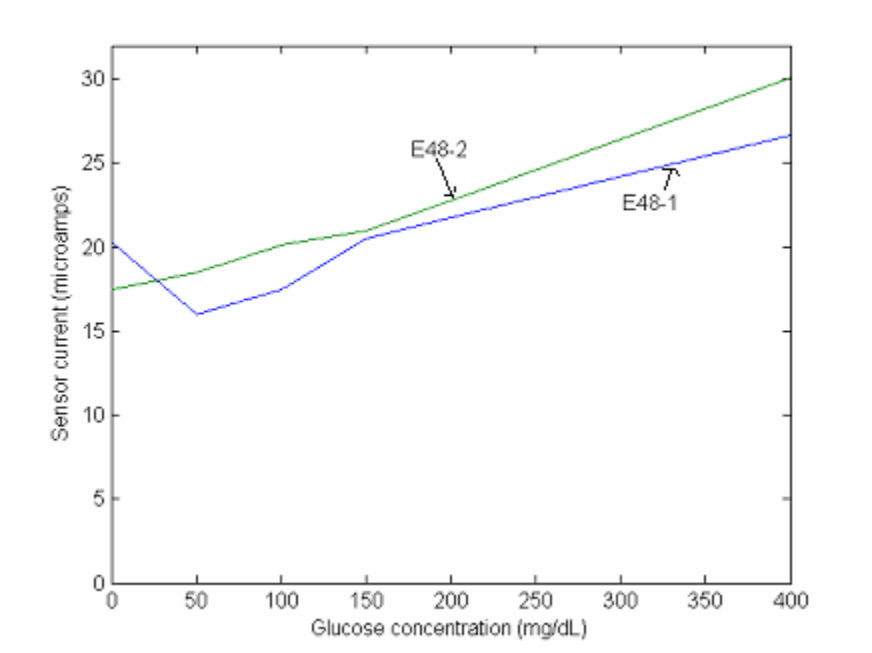

Figure 4.5 Calibration curve for sensor number 48 within a period of two days obtained from performing glucose test using known glucose concentration solution.

Similar experiments were conducted on sensor 50 and 1, the results of which are described below and the calibration curves for the sensor 50 and 1 were obtained as shown in Figure 4.6.

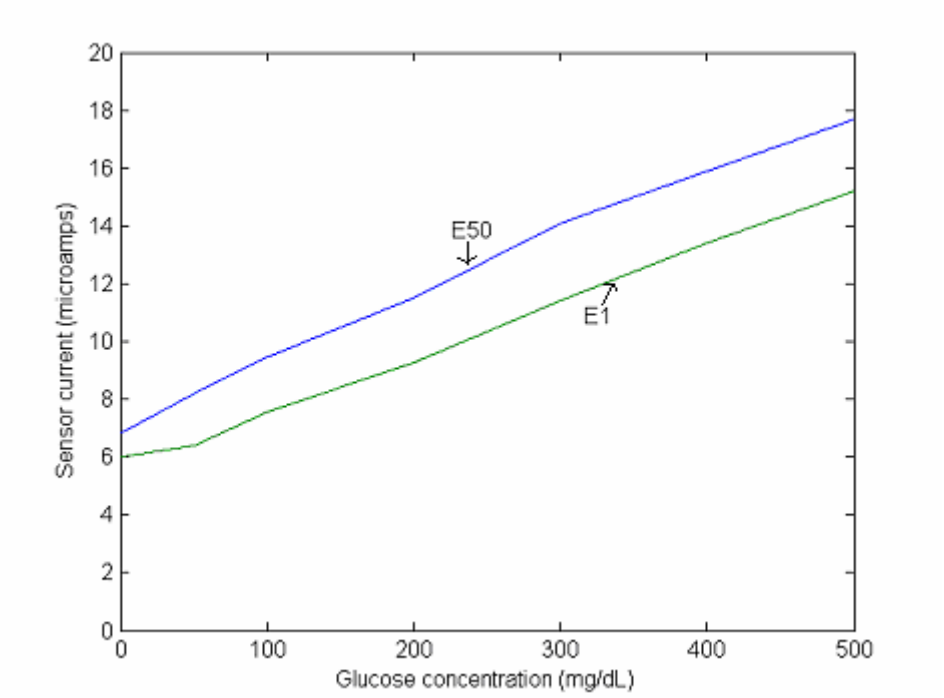

Figure 4.6 Calibration curve for sensor number 50 and 1 are shown obtained from performing glucose test using known glucose concentration solution.

The current for sensor 50 obtained from the in vivo experiment was 13 μA that corresponds to a glucose concentration of 280 mg/dL from the calibration curve. The blood glucose concentration obtained from the ACCU-CHEK^{TM} system was 490 mg/dL that results in a percentage error of 42.81%. Similarly the current for sensor 1 obtained from the in vivo experiment was 10.26 μA that corresponds to a glucose concentration of 280 mg/dL from the calibration curve. The blood glucose concentration obtained from the ACCU-CHEK^{TM} system was 490 mg/dL that results in a percentage error of 42.81%.

4.4 Controlled feedback results for 2 x 2 arrays

As discussed in section 3.7, the goal of the feedback control loop is to regulate the glucose concentration level between 70-170 mg/dL. An uncontrolled glucose concentration signal shown in Figure 4.7 by ++ was used which was higher than the maximum allowable limit of 170 mg/dL. This is the uncontrolled glucose concentration signal that has to be regulated within the two levels marked as 70 and 170 mg/dL shown by horizontal lines in Figure 4.7. Algorithms based on assumptions stated in section 3.7 were developed and simulated on MATLAB®. The code used to provide a feedback from the glucose sensor to the insulin delivery system is presented in the Appendix B. The PID algorithm is fragmented using different cases explained in Section 3.7 to track the error and limit the glucose concentration signal between the required levels. The signal marked as the controlled glucose signal in Figure 4.7 is obtained as an output of the controller, which lies well within the required level of 70-170 mg/dL of glucose concentration.

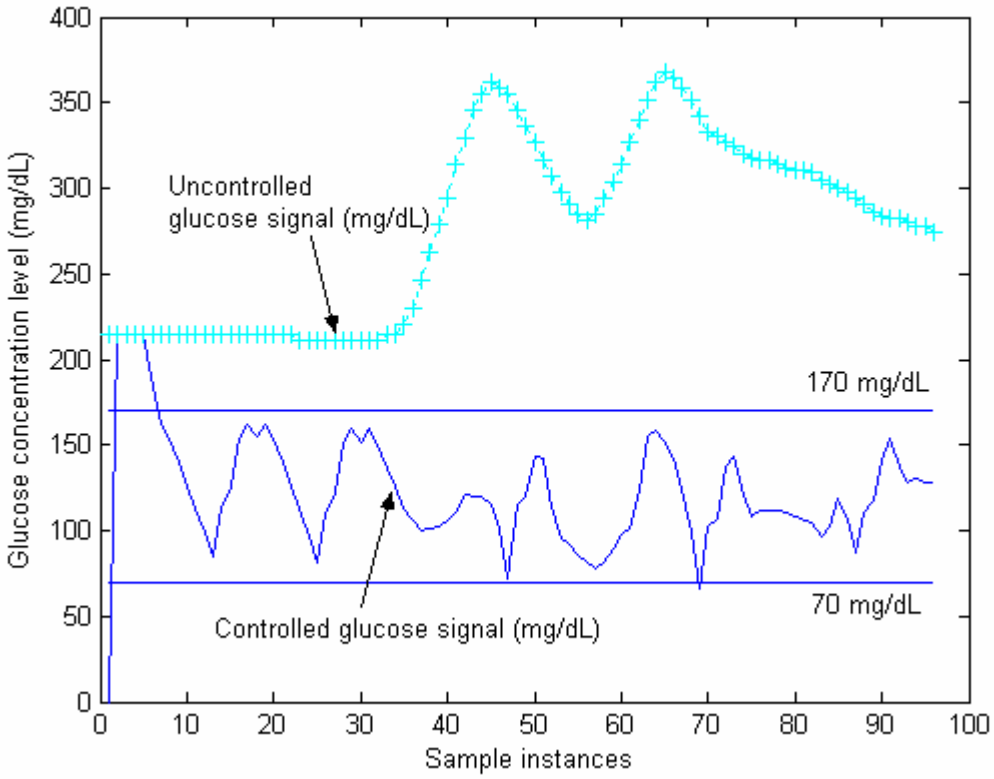

Figure 4.7 The figure demonstrates the simulation result for controlling the glucose level using a 2 x 2 array. The cyan colored waveform displays the original glucose signal and the dark blue colored waveform displays the glucose signal after the feedback control. The controlled glucose level is shown lying within the limits of 70-170 mg/dL.

As shown above in Figure 4.7, glucose concentration was measured at a sampling interval of 15 minutes. During the time duration of 100 samples, each of 15 minutes, glucose concentration level is checked and insulin level is updated. The code has a switch variable, which assumes the value of 1 or 0 corresponding to switch ON or OFF respectively. The software control will translate this on-off sequence to a hardware panel that can be used to power the insulin delivery system used. This powering on and off of the insulin delivery system will control the time and amount of ultrasound exposure on the skin and regulate the glucose concentration in the blood within the desired level. It is also observed that the

controlled glucose concentration occasionally goes beyond the maximum permissible limit, which in this case was producing an error of around 5%.

Chapter 5
Conclusions

Noninvasive insulin delivery and glucose sensor systems in conjunction with a proportional integral derivative (PID) feedback controller can be used to develop a “smart” diabetes management system, which will enable continuous glucose monitoring and deliver insulin into the body thus preventing hypoglycemic and hyperglycemic states.

In the process of achieving the above goal, the importance of introducing the π-type impedance matching network in the experimental setup was also realized. From the results obtained, it can be concluded that the transducer output voltage increases by 3 times when the π-type impedance matching network is introduced between the amplifier output and the transducer input terminals. This in turn increases the ultrasound intensity produced. Animal experiments conducted on hyperglycemic rabbits using the above impedance matching network does demonstrate that the glucose level reduced by 208.1 mg/dL for 60 minutes of ultrasound exposure with an ultrasound intensity of 100 mW/cm^2 using the cymbal array.

The same system was used in conjunction with an enzyme based glucose biosensor for continuous glucose monitoring in hyperglycemic rats. Comparing the results obtained from the glucose biosensor and the ACCU-CHEK^{TM} blood glucose monitoring system, the usability of noninvasive techniques for blood glucose monitoring has been demonstrated.

Finally the simulation model based on a PID algorithm was developed to integrate the noninvasive insulin delivery and glucose sensor systems to maintain the glucose concentration level between 70-170 mg/dL. The model was successful in stabilizing the glucose concentration level within the specified range with an error of ± 5%.

Because of time constraint, the controller experiments were not done in real time animal experiments. In future, several data will have to be collected to measure the effect of the insulin on the glucose concentration level. Many factors including body weight, physiological condition, etc. will have to be considered for accurate design.

REFERENCES

[1] Emiliano Maione, K. Kirk Shung, Richard J. Meyer, Jr., Jack W. Hughes, Robert Newnham, and Nadine. B. Smith, "Transducer Design for a portable Ultrasound Enhanced Transdermal Drug-Delivery System," *IEEE transactions on ultrasonics, ferroelectrics, and frequency control*, vol.49, no.10, pp. 1430-1436, 2002.

[2] J. Jaremko and O. Rorstad, "Advances towards the implantable artificial pancreas for treatment of diabetes," *Diabetes care*, vol. 21, no. 3, 1998.

[3] N. B. Smith, S. Lee and K. K. Shung, "Ultrasound mediated transdermal in vivo transport of insulin with low profile cymbal arrays," *Ultrasound in Medicine & Biology*, vol. 29, no. 8, pp. 1205-1210,2003.

[4] American Diabetes Association (2003). http://www.diabetes.org/home.jsp

[5] E. Max and R. Harold, *Diabetes mellitus: theory and practice*, 3rd ed. Garden City, NY: Medical Examination Pub. Co., 1983.

[6] C. R. Kahn," Conquering diabetes," *NIH Publication* vol. 99,no.4398, 1999.

[7] K. K. Shung, *Principles of medical imaging*. San Diego, CA: Academic Press, 1992.

[8] A. D. Pierce, *Acoustics: an introduction to its physical principles and applications*. Woodbury, NY: Acoustical Society of America, 1989.

[9] J. A. Zagzebski, *Essentials of ultrasound physics*. St. Louis: Mosby, 1996, pp. 41-48.

[10] T. Ikedo, *Fundamentals of piezoelectricity*. Oxford, NY: Oxford University Press, 1996.

[11] J. G. Webster and J. W. Clark, *Medical instrumentation: application and design*. NY: Wiley, 1998, pp.129-137.

[12] P. Suetens, *Fundamentals of medical imaging*. N.Y.: Cambridge University Press, 2002.

[13] C. E. Brennen, *Cavitation and Bubble Dynamics*. N.Y.: Oxford University Press, 1995.

[14] S. Mitragotri, D. Blankschtein R. Langer," Transdermal drug delivery using low-frequency sonophoresis," *Pharmaceutical Research*, vol. 13, no.3, 1996,pp.411-420.

[15] J. Zhang, W. J. Hughes, R. J. Meyer Jr., K. Uchino and R. E. Newnham, "Cymbal array: a broad sound projector," *Ultrasonics*, vol.37, no. 8, 2000, pp.523-529.

[16] J. Zhang, "Miniaturized flextensional transducers and arrays," Ph.D. dissertation, The Pennsylvania State University, University Park, PA, 2000.

[17] G. Matthaei, *Microwave Filters, Impedance-Matching Networks, and Coupling Structures*. Norwood, MA: McGraw-Hill, 1980.

[18] Y.S. Zhu and W. K. Chen, *Computer-Aided Design of Communication Networks*. NY: Cambridge University Press, 1999.

[19] S. P. J. Higson, S. M. Reddy and P. M. Vadgama, "Enzyme and other biosensors: Evolution of a technology", *Engineering Science and Education Journal*, Feb 1994, pp.41-48.

[20] E. Wilkins and P. Atanasov," Glucose monitoring: state of the art and future possibilities," *Medical Engineering Physics*, vol.18, no.4, 196, pp.273-288.

[21] K. Ogata, *Modern control engineering*. Upper Saddle River, NJ: Prentice Hall, 2002.

[22] R. Dorf, *Modern control systems*. Upper Saddle River, NJ: Prentice Hall, 2005.

[23] P. R. Shepherd and B. B. Kahn," Mechanisms of disease: Glucose transporters and insulin action-implications for insulin resistance and diabetes mellitus**."** *New England Journal of Medicine*, pp.677-684, 1999.

[24] T. Hershey, N. Bhargava, M. Sadler, N. H. White and S. Craft, "Conventional versus intensive diabetes therapy in children with type 1 diabetes," *Diabetes Care*, vol. 22, no. 8,pp. 1318-1324, 1999.

[25] J. S. Naylor, A. S. Hodel, B. Morton and Darren Schumacher, “Automatic control issues in the development of an artificial pancreas”, *American control conference*, vol. 1, pp. 23-27, 1995.

[26] C. A. Keele and E. Neil, *Samson Wrights Applied Physiology*. NY: Oxford University Press, 1962.

[27] R. A. De Fronzo, E. Ferrannini, H. Keen and P. Zimmet, *International Textbook of Diabetes Mellitus*, 3rd ed. NY: Wiley, 2004.

[28] *Ferrite cores technical information User Manual*. Magnetics, 1949.

[29] J. Harkness and D. J. Wagner,” *The Biology and Medicine of Rabbits and Rodents*,” 4th ed. Baltimore, MD: Williams and Willkins, 1995.

Perspectives on Transdermal Ultrasound Mediated Drug Delivery

Please send correspondence to:
Nadine Barrie Smith, Ph.D.
Department of Bioengineering
The Pennsylvania State University
21 Hallowell Building
University Park, PA. USA16802
Tel: 814-865-8087 Fax: 814-863-0490
nbs@engr.psu.edu

Keywords: ultrasound, drug delivery, cavitation, intensity, transdermal, review

Abstract

Use of needles for multiple injection of drugs, such as insulin for diabetes, can be painful. As a result, prescribed drug noncompliance can results in severe medical complications. Several noninvasive methods exist for transdermal drug delivery. These include chemical mediation using liposomes and chemical enhancers or physical mechanisms such as microneedles, iontophoresis, electroporation, and ultrasound. Ultrasound enhanced transdermal drug delivery offers advantages over traditional drug delivery methods which are often invasive and painful. Recent studies have shown that ultrasound mediated transdermal drug delivery. A broad review of the transdermal ultrasound drug delivery literature has shown that this technology offers promising potential for noninvasive drug administration. From a clinical perspective, currently few drugs, proteins or peptides have been successfully administered transdermally because of the low skin permeability to these relatively large molecules however much work is underway to change this. The proposed mechanism of ultrasound has been suggested to be the result of cavitation which is discussed along with the bioeffects from therapeutic ultrasound. For low frequencies, potential transducers which can be used for drug delivery are discussed along with cautions regarding the ultrasound safety versus efficacy

Introduction

Several methods exist for increasing transdermal drug delivery such as chemical mediation using liposomes or chemical enhancers, and physical mechanisms such as iontophoresis, lasers, electroporation, microneedles and ultrasound (also called sonophoresis or phonophoresis) (Prausnitz 1997; Prausnitz 1999; Montorsi et al. 2000; Wang et al. 2005; Nanda et al. 2006). Among these methods exist numerous studies which have shown that ultrasound mediated transdermal drug delivery offers promising potential for noninvasive drug administration. However the ultrasound drug delivery research literature also broad and does not just refer to transdermal applications. There is a large body of work focusing on the specifically delivery to internal organs, tissues or gene delivery is not covered herein. Additionally for transdermal work, the reader is also directed to several well written articles for further reading and additional viewpoints on this topic (Mitragotri and Kost 2004; Pitt et al. 2004; Brown et al. 2006).

Passive drug delivery across the stratum corneum can be transported with molecules that have a weight less than 500 Da (Brown et al. 2006). In general the stratum corneum, which varies in thickness (≈ 10-20 μm) depending on the body location, forms the barrier to drug diffusion. This low permeability is attributed to the outermost skin layer that consists of a compact and organized structure of cells named keratinocites surrounded by lipid bilayers. Ultrasound enhanced transdermal drug delivery offers advantages over traditional injection drug delivery methods which are invasive and painful. Currently few drugs, proteins or peptides have been successfully administered transdermally for clinical applications because of the low skin permeability to these relatively large molecules. However from a research viewpoint, the list of compounds which have been shown to transdermally cross skin via ultrasound is ever increasing. One hypothesis indicates that once the drug has traversed the stratum corneum, the next layer is easier to cross and subsequently the drug can reach the capillary vessels to be absorbed (Mitragotri et al. 1995b).

Background on Ultrasound Delivery and Biological Effects

One of the earliest reports of the interaction between ultrasound and biological tissue can be traced back to the 1920's with the post-World War I experiments of Professor Paul Langévin (Graff 1981). Much of his work centered on the development of pulse-echo sonar for submarine detection but with the observation of bubble formation in the water and the killing of fish from the sound beam. Specific biological changes such as searing of skin, rupturing of red blood cells and lethal effects on mammals were observed by Wood and Loomis with 200-500 kHz high intensity ultrasound (Wood and Loomis 1927).

In contrast to ultrasound used for diagnostic imaging, therapeutic ultrasound can be described as a controlled sound waves intended for biological interaction for a curative benefit. Some of the first clinically significant application of this technology was developed by Francis and William Fry in the 1950's (Fry et al. 1954; Fry 1954). Their work was applied to the development of ultrasound devices for noninvasive surgical treatment of neurological disorders including Parkinson disease. Results included both reversible and irreversible biological effects. Other early clinical applications at this same

time include the treatment of arthritis using ultrasound with hydrocortisone to relieve pain (Fellinger and Schmid 1954).

Thus it is suitable to divide therapeutic ultrasound into two categories that use 'low' intensities and 'high' intensities (> 5 W/cm^2) though this boundary is not precise (ter Haar 1999). High intensity focused ultrasound (HIFU) is an attractive means of noninvasively coagulating deep tissues with external sources. Current clinical applications of ultrasound include transducer and array designs for the treatment of prostate cancer (Gelet et al. 2004; Saleh and Smith 2004), liver tumors (Li et al. 2004; Gignoux et al. 2003), breast cancer (Jenne et al. 2003; Wu et al. 2004), bladder tumors (Wang et al. 2003; Madersbacher and Marberger 2003) and uterine fibroids (Chan et al. 2002; Tempany et al. 2003). Low intensity ultrasound has been shown to mediate the transport of drug across the skin and is clinically used in physical therapy to accelerate or stimulate a normal biological response through deep heating.

Many recently reviews have shown that ultrasound mediated transdermal drug delivery offers promising potential for noninvasive drug administration (Tachibana and Tachibana 2001; Pitt et al. 2004; Mitragotri 2005). The working principle of sonophoresis, although not completely understood, has been suggested to be the result of cavitation (Mitragotri et al. 1995b; Mitragotri et al. 1997) although thermal effects can not be entirely discounted. Low frequency ultrasound is capable of generating microbubbles in the water and tissue. These bubbles allow water channels to be produced within the lipid bilayers. The resulting disorder created in the stratum corneum facilitates the crossing of a hydrophilic drug or molecule.

Table 1 attempts to presents an overview of the transdermal ultrasound mediated drug delivery literature from the past several years with some commentary on notable contributions. Though not complete, the table lists the delivered compound or drug, its respective molecular weight (Daltons) and the experimental sample (animal) preparation including whether the experiment was performed under *in vivo* or *in vitro* conditions. Of major interest is the ability to reduce the research to clinical practice and therefore the reported ultrasound frequency and device is listed. For the table, ultrasound devices can be classified into different categories. The commercially made devices include sonicators (≈ 20 kHz), ultrasound heating devices intended for therapy (>1 MHz) and pre-fabricated transducers. Very few of the ultrasound devices listed are specifically designed for drug delivery and originally, like the sonicator, have a different intended purpose.

With sonophoresis, many previous investigators have found enhanced transdermal drug delivery over various frequency ranges using commercial sonicators or therapeutic devices. For example, a 14-fold increase of corticosterone transport has been shown using a 1 MHz therapeutic product used for the treatment of chronic and acute pain (Sonopuls® 463, Sugarland, TX) operating at 1.4 W/cm^2 for 24 hours (Johnson et al. 1996). Significant transdermal transport of model drugs such as mannitol and inulin (plant starch) have been seen using a 20 kHz commercial sonicator (VCX400, Sonics and Materials, Newtown, CT) (Levy et al. 1989). Previous work with high frequency ultrasound (≈1 MHz and at 1-3 W/cm^2) to enhance transdermal drug delivery have produced interesting results and were found to vary from drug to drug (Bommannan et al. 1992a; Bommannan et al. 1992b; Mitragotri et al. 1997). Pulsed ultrasound at 1 MHz has been used to increase transdermal absorption of indomethacin from an ointment in rats (Asano et al. 1997). Also, the combination of chemical enhancers and therapeutic

ultrasound (1 MHz, 1.4 W/cm^2, continuous wave (CW) on transdermal drug transport have been investigated with success (Johnson et al. 1996).

Noteworthy differences between high (1-3 MHz) and low (≈20 kHz) frequency ultrasound appears to be that low frequency ultrasound enhances transdermal drug transport 1000 times greater than high frequency ultrasound (Mitragotri et al. 1996). The working hypothesis for the physical mechanism is that low-frequency ultrasound enhances transdermal transport through aqueous channels in the *stratum corneum* generated by cavitation induced bilayer disordering. However, the mechanism of the enhancement using ultrasound is far from being fully understood (Pitt et al. 2004). Some researchers have concluded that at 168 kHz using CW ultrasound and at 1.9* x 10^5 Pa induced a new structural state and generated defects in human stratum corneum specimens. They suggest that the dimensions of the defects (20 μm) were large enough to allow the transdermal passage of high molecular weight drug molecules that normally elude the unenhanced transdermal drug delivery (Wu et al. 1998).

Past research has demonstrated the possibility to deliver and control therapeutic doses of proteins such as interferon gamma and erythropoeitin across human skin using ultrasound (Mitragotri et al. 1995a). Other researchers have investigated the *in vitro* penetration and the *in vivo* transport of flufenamic acid in skin with ultrasound (Hippius et al. 1998). In the flufenamic acid study, ultrasound exposure was from 5-30 minutes with intensities up to 1.5 W/cm^2. Although there was a pronounced effect of ultrasound on the transmembrane absorption of the drug, there was also a rise of temperature up to 4.5^{o}C. Ultrasound at 1 MHz has also been used to enhance the transdermal absorption of indomethacin studied in rats using intensities from 0.25 - 1 W/cm^2. The researchers reported no significant skin temperature rise and no notable damage to the skin however damage was noted as the intensity and the time of application of ultrasound increased beyond 1 W/cm^2 (Miyazaki et al. 1992).

Other researchers have reported noticeable skin damage from ultrasound transdermal drug delivery experiments (Wu et al. 1998). One group has examined the morphological changes induced with *in vitro* hairless mouse skin and human skin after ultrasound exposure for a transdermal drug delivery systems. The skins were immersed in a commercial ultrasound water tank at 48 kHz and an intensity of 0.5 W/cm^2. Skins were compared to control skins under a scanning electron microscope and found cells of the stratum corneum of the mouse skin surface were almost completely removed. Also in the mouse skin, large craterlike pores with a diameter of 100 microns were formed sporadically in some of the skin samples. However in human skin, the surface of skin exposed to ultrasound showed only slight removal of keratinocytes around the hair follicles. The researchers suggested that the removal of the stratum corneum and other alterations in hairless mouse and human skin may explain the enhancement of transdermal drug penetration (Yamashita et al. 1997).

Convenient noninvasive methods for transdermal delivery of insulin or similar procedures for glucose sensing has particular public interest due to the increasing problem of diabetes. In the United State alone, approximately 16 million people suffer from diabetes mellitus. From a human and economic perspective, it is one of the most costly diseases (Congressionally Established Diabetes Research Working Group 1999; The Whitaker Foundation 2004). Management of diabetes often requires painful repetitive blood glucose tests and insulin injections up to three-four times each day.

Between injections, blood sugar levels can fluctuate and remain out of balance until the next test or injection, increasing the risk of tissue or organ damage.

Specifically for insulin (Table 1), the amount of research for noninvasive insulin delivery is increasing every year. Over a frequency range of 20-105 kHz, enhanced transport in the presence of ultrasound has been shown in both *in vitro* and *in vivo* experiments. Many early experiments were performed using either an ultrasound sonicator, ultrasonic bath or commercial transducer. For example investigators have demonstrated effective *in vivo* transport of insulin at 48 kHz using an ultrasonic bath (Tachibana and Tachibana 1991) and 105 kHz (Tachibana 1992) using a commercially obtained transducer. The major drawback so far in exploiting ultrasound for noninvasive drug delivery is the large size and poor mobility of the ultrasound device. Commercial sonicators are large, heavy, table-top devices specifically designed for lysis of cells, catalyzing reactions, creating emulsions or cleaning,. There does exist a few commercial ultrasound devices specifically designed for ultrasound drug delivery such as the SonoPrep® made by the Sontra Medical Corporation, (Cambridge MA) which is a large ultrasound device that consists of a power control unit and a hand-held applicator.

Although diabetics have an aversion to injecting insulin they probably hate the more frequent finger-stick for blood glucose samples even more. A number of different techniques for monitoring blood glucose using non- or minimally invasive methods are under investigation including near-infrared spectroscopy, implantable glucose sensors, reverse sonophoresis, reverse iontophoresis and interstitial fluid sampling devices (Kost 2002). The latter three techniques extract glucose transdermally and measure glucose in interstitial fluid. Dermal interstitial fluid glucose concentration is highly correlated with the plasma glucose concentration and capillary blood glucose concentration. Thus, transdermal extraction of interstitial fluid offers a noninvasive method of obtaining a sample for blood glucose measurements (Cantrell et al. 2000; Kost 2002). Previous results has demonstrated positive results in the use of ultrasound to facilitate the noninvasive extraction of interstitial skin fluids (ISF) for blood glucose monitoring through an electrolytic reaction with glucose sensitive enzymes (Kost et al. 2000).

Mechanism of Ultrasound

In so much as ultrasound is known to increase transdermal protein delivery (Tachibana 1992; Mitragotri et al. 1995a) the mechanisms of this enhanced transport have not been fully characterized (Pitt et al. 2004). Bioeffects from ultrasound include thermal or mechanical (cavitation) mechanism (AIUM 2000). One effect of cavitating ultrasound is its ability increase permeability of the outer skin layer (stratum corneum), which is thought to be a primary barrier to protein diffusion. Cavitation describes the rapid expansion and collapse of gaseous bubbles in response to an alternating pressure field. Cavitation types can be broken into two non-exclusive categories (Flynn 1982). The first is stable cavitation where the cavity oscillates about its equilibrium radius in response to relatively low acoustic pressures. The second is transient cavitation (also known as inertial cavitation) where by the equilibrium size varies greatly in response within very few acoustic cycles. During transient cavitation, the rapid, violent collapse of bubbles is associated with high acoustic pressures and temperatures on the order of 1000-2000 K (Apfel 1981; Apfel 1981). Transient cavities are generated in response to high

acoustic pressures and/or lower frequencies. The violent hydrodynamic forces (Fig. 2) due to a collapsing bubble can cause severe damage within biological media and free radicals can be produced by this violent phenomena (Edmonds and Sancier 1983; Mason and Lorimer 1988).

There exists several definitions for the threshold for transient cavitation in terms of such physical parameters as acoustic pressure, frequency or bubble radius. For diagnostic ultrasound, one (of many) definitions of the cavitation onset is the peak rarefractional pressure divided by the square root of the frequency (Apfel and Holland 1991). From previous research, the measured cavitation pressure amplitude in dog thigh muscle *in vivo* was found to depend linearly on frequency with a slope of 5.3 MPa/MHz (Hynynen 1990). Compared to the kilohertz range, ultrasound in the megahertz range also produces cavitation although much higher pressures are required to exceed the cavitation threshold. Beyond the threshold, cavitation has been shown to disrupt cells and damage tissue (Dalecki et al. 1996; Miller et al. 1996). Mechanical bioeffects in tissues with gas bodies include lung hemorrhage in mice, rats, monkeys and pigs (AIUM 2000). Cavitation has also been shown with diagnostic ultrasound levels (Apfel 1986; Roy et al. 1990) which has motivated the introduction of the mechanical index to identify a threshold pressure for the onset of inertial cavitation (AIUM-NEMA 1996). Even in the absence of well-defined gas bodies, there exists non-thermal bioeffects due to ultrasound that are known to occur in the absence of excessive heating or evidence of cavitation bubbles. In this situation, the mechanism is in the form of radiation force or torque or acoustic streaming (Beyer 1997).

The dynamics of acoustic cavitation in liquid alone differs considerably than cavitation at liquid-solid interfaces. Ultimately acoustic bubble dynamics are quite complex and beyond this overview (Apfel 1981; Leighton 1994; Hamilton and Blackstock 1998). Determining the threshold and energy from a cavitation event is difficult under the best conditions. Researchers in ultrasound try to follow three experimental rules with respect to cavitation: understand the liquid including impurities, understand the sound field and know when something happens (Apfel 1981). The first rule refers to the cavitation threshold while the second rule relates to accurate measurements of the acoustic field. The third relates to observable cavitation events or secondary related information. Rule two deals with a commentary regarding information which could have been included in Table 1 but was intentionally omitted. Though many of the papers listed in Table 1 report an ultrasound intensity, drawback is that much of the literature gives a value but does not specify details of the exposimetry such as spatial (average, peak) or temporal (average, peak) values. For reporting the determination of an acoustic field, it is essential to supply enough information, such as calibrated hydrophones, dissolved gas concentration, anechoic conditions, etc., so that that intensity experiments can be repeated by others. Therefore accurate and precise evaluation of acoustic fields should follow exposimetry and dosimetry procedures previously recognized in the ultrasound literature (Schafer et al. 1990; Lewin and Ziskin 1992; AIUM-NEMA 1996; Lewin et al. 2003). Without such information, it is impossible to compare the intensity of enhanced transport between many of the drug delivery publications or determine potential bioeffects.

Future of Transdermal Drug Delivery

Use of transdermal drug delivery techniques has the most practical clinical application to medications which need to be injected multiple times either daily or weekly. Though infrequent, other injectable drug avoidance situations could include when needles do not want to be used with infants, children and pets or under harsh conditions (battlefield or first responder) where needles are not feasible. As seen in Table 1, many previously researchers who have successfully used acoustic energy for drug delivery have used commercial sonicators or off-the-shelf transducers. These large industrial devices are impractical for a feasible and transportable drug delivery device. Much of the previous ultrasound transdermal dry delivery research has focused on low frequencies primarily because commercial sonicators were designed to only operate at one frequency. To bring this research to clinical practice will require more research into the optimal frequency and intensity for each particular drug. As with the diagnostic ultrasound imaging, drug delivery using ultrasound requires a delicate balance between safety and efficacy and requires careful scientific study.

Other recent reviews on drug delivery state similar views expressed here including that "small-sized low-frequency transducers need to be developed so that patients can wear them" (Pitt et al. 2004). Although there are several possible low frequency transducer designs that can be used in a drug delivery application, such as the low frequency flextensional resonators (Stansfield 1990), tonpilz transducers (Wilson 1988), or "thickness"-type resonators (Shung et al. 1992), the "cymbal" transducer design is a good choice for a portable device. This Class V flextensional transducer has a thickness of less than 2 mm, weighs less than 3 grams, resonates between 1 and 100 kHz depending on geometry, and has a large scale manufacturing cost of less than $5.00/unit (Newnham et al. 1991; Newnham et al. 1994; Dogan et al. 1997) Newnham, 1998 44 /id}(Tressler et al. 1998). With the low profile cymbal design, high frequency radial motions of the ceramic translates into low frequency displacement motions through the cap covered cavity. If the diameter of the ceramic is increased (i.e. a larger single element), then the frequency of the transducer decreases towards a lower range. Also if the diameter increased, the capsule depth of the flextensional design needs to increase thereby increasing the thickness and slightly increasing the profile. Cymbals can be arranged into multi-element array designs (Fig. 3) since this can increase the effective aperture of ultrasound area with respect to skin area and some research indicates that the delivery dose increases with ultrasound exposure area (Smith et al. 2003). Interestingly the cymbal design originates from underwater research for Navel applications and current research is underway to incorporate existing battery technology in the miniaturization of portable power for both insulin delivery and glucose sensing {Lee, 2004 160 /id}{Lee, 2005 161 /id}.

In general the future for noninvasive drug delivery is encouraging. Exploiting transdermal ultrasound drug delivery beyond the feasibility stage will require the cooperation of medical doctors and engineers so that the technology a become a clinical device. As with diagnostic ultrasound, the bioeffects and safety of each device needs to be carefully monitored since it will not matter how much of any drug can be transported if the skin is burned, damaged or the procedure is painful.

Acknowledgements
This work was supported by the Department of Defense Technologies for Metabolic Monitoring Award Number W81XWH-05-1-0617.

Figure Legends

Fig. 1
With transient cavitation the bubble dynamics have two basics stages comprising of the initial formations of the cavity followed by the growth and asymmetric violent collapse. The photo shows the jet produced by the collapse of a cavitation bubble at a liquid-solid interface. [Photo courtesy of Dr. Lawrence Crum at the University of Washington]

Fig. 2
The future of practical noninvasive drug delivery may be in the use of novel transducers or ceramics for producing ultrasound. One example is the cymbal transducer made of piezoelectric material PZT-4 operated at a frequency of 20 kHz. The light weight, low-profile array was constructed using for cymbal transducers which were connected in parallel, and encased in URALITE® polymer. The dimensions of the array were 37 x 37 x 2 mm^3 and is compared in size to a US quarter; it weighed less than 22g.

Figure 1.

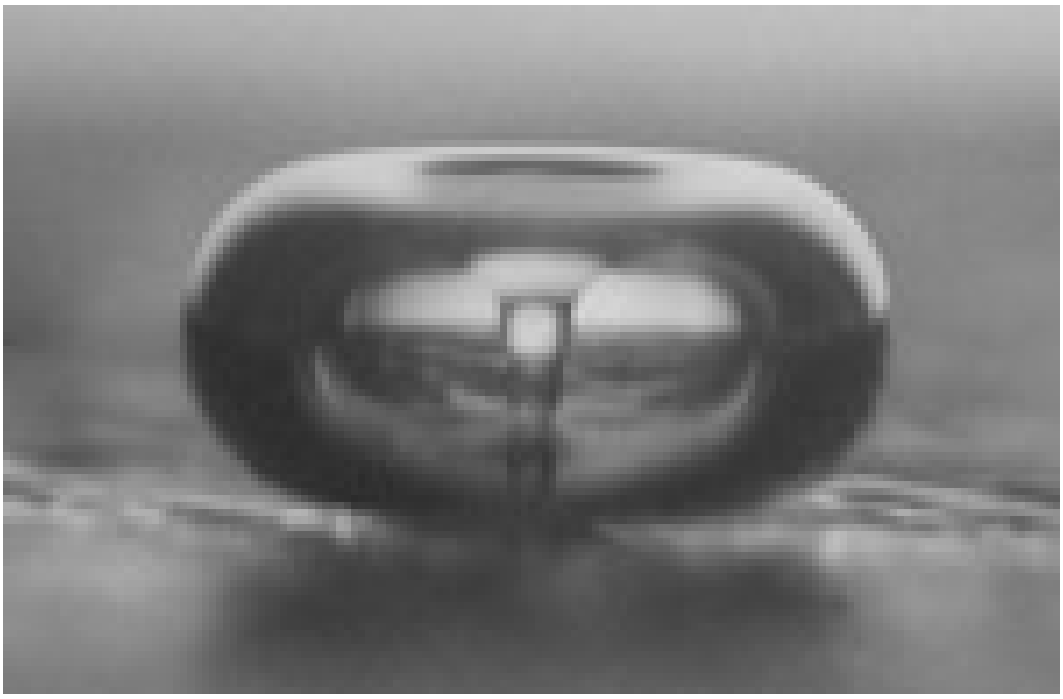

Figure 2.

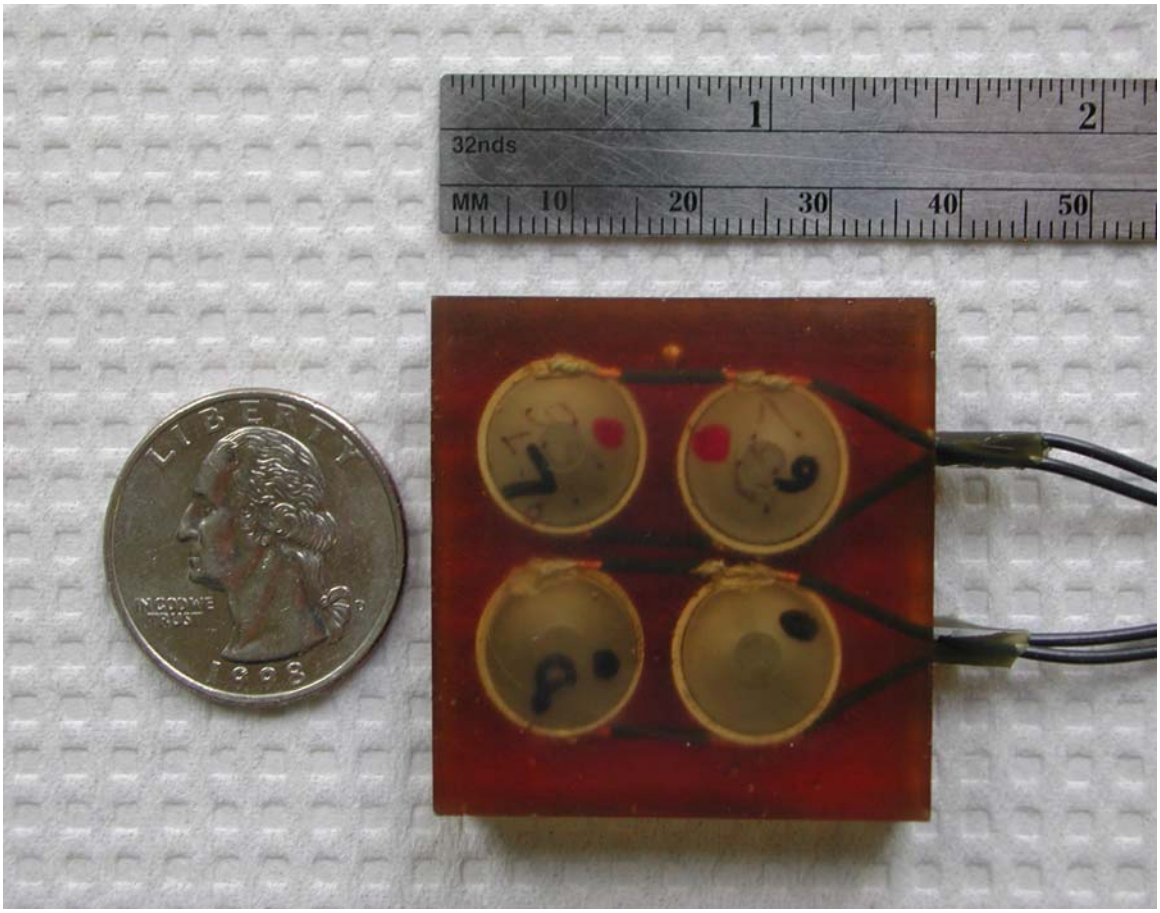

Table 1. A list of transdermally delivered drugs and compounds using ultrasound devices.

Compound	M.W	Preparation	Frequency	Device	Investigator
Aldosterone	832	in vitro human	20 kHz	Sonicator[1]	(Johnson et al. 1996)
Benzene	78	in vitro human	1 – 3 MHz	Therapeutic[5]	(Mitragotri et al. 1995b)
Bicarbonate	136	in vivo rat	20 kHz	Sonicator[1]	(Mitragotri et al. 2000b)
Butanol	74	in vitro human	1 – 3 MHz	Therapeutic [5]	(Mitragotri et al. 1995b)
Butanol	74	in vitro human	20 kHz	Sonicator[1]	(Johnson et al. 1996)
Caffeine	194	in vitro human	1 – 3 MHz	Therapeutic[5]	(Mitragotri et al. 1995b)
Caffeine	194	in vitro human	20 kHz	+++	(Boucaud et al. 2001)
Caffeine	194	in vitro rat	20 kHz	+++	(Boucaud et al. 2001)
Calcein	623	in vitro rat	41, 158, 445 kHz	US transducer[13]	(Mutoh et al. 2003)
Calcein	623	in vitro cell membrane	20, 57, 76, 93 kHz	US transducer[17]	(Sundaram et al. 2003)
Calcein	623	in vitro porcine	20 kHz	US transducer[21]	(varez-Roman et al. 2003)
Calcein	623	in vitro pig	20 kHz	Sonicator[1]	(Kushner et al. 2004)
Calcein	623	in vitro rat	41 kHz	US transducer[9]	(Morimoto et al. 2005)
Calcium	40	in vivo rat	20 kHz	Sonicator[1]	(Mitragotri et al. 2000b)
Corticosterone	346	in vitro human	1 MHz	Therapeutic US[2]	(Johnson et al. 1996)
Corticosterone	346	in vitro human	1 – 3 MHz	Therapeutic US[5]	(Mitragotri et al. 1995b)
Corticosterone	346	in vitro human	20 kHz	Sonicator[1]	(Johnson et al. 1996)
Dexamethasone	392	in vitro human	1 MHz	Therapeutic US[2]	(Johnson et al. 1996)
Dexamethason	392	in vivo human	1 MHz	US transducer[10]	(Darrow et al. 1999)
Dextran^{++}	2000	in vivo rat	20 kHz	Sonicator[1]	(Mitragotri et al. 2000b)
Dextran	70000	in vitro pig	58 kHz	US transducer[17]	(Tezel et al. 2003)
Diclofenac	296	in vivo human	1 MHz	Therapeutic	(Rosim et al. 2005)
Diclofenac	296	in vivo rat	1 MHz	Sonicator[12]	(Hsieh 2006)
Erythropoeitin	48000	in vitro human,	20 kHz	Sonicator[1]	(Mitragotri et al. 1995a)
Estradiol	272	in vitro human	1 MHz	Therapeutic US[2]	(Johnson et al. 1996)
Estradiol	272	in vitro human	1 – 3 MHz	Therapeutic US[5]	(Mitragotri et al. 1995b)
Estradiol	272	in vitro human	20 kHz	Sonicator[1]	(Mitragotri et al. 1996)
FD-4*	4400	in vitro rat	41 kHz	US transducer[9]	(Morimoto et al. 2005)
FD-40*	38000	in vitro rat	41 kHz	US transducer[9]	(Morimoto et al. 2005)
Fentanyl	336	in vitro human	20 kHz	$^{+++}$	(Boucaud et al. 2001)
Fentanyl	336	in vitro rat	20 kHz	$^{+++}$	(Boucaud et al. 2001)
FITC ****	51000	in vitro human	20 kHz	Sonifier[19]	(Weimann and Wu 2002)
FITC****	2500	in vitro human	20 kHz	Sonifier[19]	(Weimann and Wu 2002)
Fluorescein	389	in vitro human	20 kHz	Sonicator[14]	(Cancel et al. 2004)
Fluorescein probes nile red	535	in vitro porcine	20 kHz	US transducer[21]	(varez-Roman et al. 2003)
Glucose	182	in vivo rat	20 kHz	Sonicator[1]	(Mitragotri et al. 2000b)
Glucose	182	in vitro human	20 kHz	Sonicator[1]	(Kost et al. 1996)
Glucose	182	in vitro porcine	10 MHz	US transducer[20]	(Merino et al. 2003)

Glucose	182	in vitro porcine	20 kHz	Sonicator[21]	(Merino et al. 2003)
Glucose	182	in vivo rat	20 kHz	cymbal TDR	(Lee et al. 2005)
Hyaluronan	1000	in vivo rabbit	1 MHz	Therapeutic	(Park et al. 2005)
Hydrocortisone	362	in vivo rat	1 MHz	Therapeutic	(Koeke et al. 2005)
Ibuprofen	206	in vivo human	1 MHz	UStransducer[23]	(Kozanoglu et al. 2003)
Insulin	5807	in vitro human, in vivo rat	20 kHz	Sonicator[1]	(Mitragotri et al. 1995a)
Insulin	5807	in vivo rat	20 kHz	Sonicator[1]	(Boucaud et al. 2000)
Insulin	5807	in vivo rat	48 kHz	LAG-26[4]	(Tachibana and Tachibana
Insulin	5807	in vivo rabbit	105 kHz	LAG-26[4]	(Tachibana 1992)
Insulin	5807	in vivo rabbit	105 kHz	UStransducer[9]	(Tachibana 1992)
Insulin	5807	in vitro human	20 kHz	Sonicator[6]	(Zhang et al. 1996)
Insulin	5807	in vivo rat	20 kHz	Sonicator[1]	(Boucaud et al. 2002)
Insulin	5807	in vitro human	20 kHz	cymbal TDR	(Smith et al. 2003)
Insulin	5807	in vivo rat	20 kHz	cymbal TDR	(Lee et al. 2004a)
Insulin	5807	in vivo rabbit	20 kHz	cymbal TDR	(Lee et al. 2004b)
Inulin	5000	in vivo rat	20 kHz	Sonicator[1]	(Mitragotri and Kost 2000)
Inulin	5000	in vitro pig	58 kHz	US transducer[17]	(Tezel et al. 2003)
ketoprofen	254	in vivo human	1 MHz	Sonicator[22]	(Cagnie et al. 2003)
ketorolac-tromethamine	376	in vitro rat	1 MHz	Sonicator[7]	(Tiwari et al. 2004)
Lanthanum droxide	189	in vivo guinea pigs	2, 10, 16 MHz	Panametrics[3]	(Bommannan et al. 1992a)
Lidocaine	234	in vitro human	1 MHz	Therapeutic[2]	(Johnson et al. 1996)
Linoleic acid	280	in vitro human	1 MHz	Therapeutic[2]	(Johnson et al. 1996)
Luteinizing hormone	1311	in vitro pig	58 kHz	US transducer[17]	(Tezel et al. 2003)
Mannitol	183	in vivo rat	20 kHz	Sonicator[1]	(Mitragotri and Kost 2000)
Mannitol	183	in vitro pig	20 kHz	Sonicator[1]	(Mitragotri et al. 2000c)
Mannitol	183	in vivo rat	20 kHz	Sonicator[1]	(Mitragotri and Kost 2000)
Mannitol	183	in vitro pig, in vitro	20 kHz	US transducer[1]	(Tang et al. 2001)
Mannitol	183	in vitro pig, in vivo	20 kHz	US transducer[1]	(Tang et al. 2002)
Mannitol	183	in vitro pig	20 kHz	Sonicator[1]	(Terahara et al. 2002)
Mannitol	182	in vitro pig	58 kHz	US transducer[17]	(Tezel et al. 2003)
Mannitol	183	in vitro porcine	10 MHz	US transducer[20]	(Merino et al. 2003)
Mannitol	183	in vitro porcine	20 kHz	Sonicator[21]	(Merino et al. 2003)
Methylpredni-solone/ cyclosporine	374	in vivo human	25 kHz	Sonicator[7]	(Santoianni et al. 2004)
Oligonucleotides	+++	in vitro pig	20 kHz	Sonicator[1]	(Tezel et al. 2004)
Progesterone	274	in vitro human	1 – 3 MHz	Therapeutic[5]	(Mitragotri et al. 1995b)
Salicylic acid	138	in vitro human	20 kHz	Sonicator[1]	(Johnson et al. 1996)
sodium lauryl sulfate	288	in vitro pig	19.6, 36.9, 58.9, 76.6, 93.4 kHz	US transducer[17]	(Tezel et al. 2001)

sodium lauryl sulfate	288	in vitro pig	20 kHz	US transducer[11]	(Tezel and Mitragotri 2003)
sodium lauryl sulfate	288	in vitro porcine	20 kHz	Sonicator[11]	(Paliwal et al. 2006)
Sucrose	342	in vitro human	20 kHz	Sonicator[1]	(Johnson et al. 1996)
Sucrose	342	in vitro human, pig	20 kHz	US transducer[1]	(Tang et al. 2001)
Testosterone	288	in vitro human	1 MHz	Therapeutic[2]	(Johnson et al. 1996)
Tetanus Toxoid (TTx vaccine)	150000	in vivo mice	20 kHz	600W Sonicator[11]	(Tezel et al. 2005)
Triamcinolone-Acetonide	434	in vitro mice	1, 3 MHz	US transducer[9]	(Yang et al. 2006)
Urea	60	in vivo rat	20 kHz	Sonicator[1]	(Mitragotri et al. 2000a)
vasopressin	1056	in vitro human	20 kHz	Sonicator[6]	(Zhang et al. 1996)
Water	18	in vitro human	20 kHz	Sonicator[1]	(Johnson et al. 1996)

Legend
US = ultrasound
Therapeutic = commercially made ultrasound device for heating therapy
TDR = transducer
1. VCX 400, Sonics and Materials Inc., Newtown, CT
2. Sonopuls 463, Henley International
3. Precision Acoustic Devices and Panametrics
4. Leader Electronics Corp., Japan
5. Sonopuls 474, Henley International
6. W-385, Heat Systems Ultrasonics, Inc.
7. Brand not indicated
8. Cole Palmer Instrument Co, Chicago, IL
9. Transducer company not indicated
10. Omnisound 3000, Accelerated Care Plus-Physio Technology Inc., Topeka, KS.
11. Sonics & Materials, Newtown, CT
12. ITO Co, 1-23-15, Hakusan, Bunkyo-ku, Tokyu, Japan
13. Dai-ichi High Frequency, Tokyo, Japan
14. Model XL2020, Misonix Inc., Farmingdale, NY
15. Pro Seven 977 to 2000 model, Quark Productos Médicos, Brazil
16. Noblelife™, Duplogen, Suwon, Korea
17. Piezo Systems, Cambridge, MA
18. Transducers made in-house
19. Model S-110, Branson Instruments Inc., Standford, CT
20. Sofranel, Zurich, Switzerland
21. VCX 400, Sonics and Materials Inc., Danbury, CT
22. Sonoplus 590, Enraf-Nonius BV, AV Delft, the Netherlands

23. Peterson®250 Ultrasound Equipment Petaş, Turkey
[+++] details not indicated
* FITC-labeled dextrans
*** PBS solution was prepared using Milli-Q® water and a phosphate concentration of 0.01 M and NaCl concentration of 0.137 M.
[****] Fluorescein Isothiocyanate (FITC)
Note: Apologies are offered for any missing information.

Reference List

AIUM. Mechanical bioeffects from diagnostic ultrasound: AIUM consensus statements. Journal of Ultrasound in Medicine 2000; 19:68-168.

AIUM-NEMA. Standard for real-time display of thermal and mechanical acoustic output indices on diagnostic ultrasound equipment. Laurel, MD: American Institute of Ultrasound in Medicine National Electrical Manufacturers Association. 1996.

Apfel RE. Acoustic Cavitation. In: Edmonds PD, ed. Methods of experimental physics. New York: Academic Press. 1981.

Apfel RE. Possibility of microcavitation from diagnostic ultrasound. IEEE Trans Ultrason Ferroelectr Freq Contr 1986; UFFC-33:139-142.

Apfel RE, Holland CK. Gauging the likelihood of cavitation from short-pulse, low duty cycle diagnostic ultrasound. Ultrasound Med Biol 1991; 17:179-185.

Asano J, Suisha F, Takada M, Kawasaki N, Miyazaki S. Effect of pulsed output ultrasound on the transdermal absorption of indomethacin from an ointment in rats. Biol Pharm Bull 1997 Mar; 20:288-291.

Beyer RT. Nonlinear Acoustics. Sewickley, PA: Acoustical Society of America Publications. 1997.

Bommannan D, Menon GK, Okuyama H, Elias PM, Guy RH. Sonophoresis. II. Examination of the mechanism(s) of ultrasound- enhanced transdermal drug delivery. Pharm Res 1992 Auga; 9:1043-1047.

Bommannan D, Okuyama H, Stauffer P, Guy RH. Sonophoresis. I. The use of high-frequency ultrasound to enhance transdermal drug delivery. Pharm Res 1992 Aprb; 9:559-564.

Boucaud A, Garrigue MA, Machet L, Vaillant L, Patat F. Effect of sonication parameters on transdermal delivery of insulin to hairless rats. J Control Release 2002 May 17; 81:113-119.

Boucaud A, Machet L, Arbeille B, Machet MC, Sournac M, Mavon A, Patat F, Vaillant L. In vitro study of low-frequency ultrasound-enhanced transdermal transport of fentanyl and caffeine across human and hairless rat skin. Int J Pharm 2001 Oct 9; 228:69-77.

Boucaud A, Tessier L, Machet L, Vaillant L, and Patat F. Transdermal delivery of insulin using low frequency ultrasound. *In*

Brown MB, Martin GP, Jones SA, Akomeah FK. Dermal and transdermal drug delivery systems: current and future prospects. Drug Deliv 2006 May; 13:175-187.

Cagnie B, Vinck E, Rimbaut S, Vanderstraeten G. Phonophoresis versus topical application of ketoprofen: comparison between tissue and plasma levels. Phys Ther 2003 Aug; 83:707-712.

Cancel LM, Tarbell JM, Ben-Jebria A. Fluorescein permeability and electrical resistance of human skin during low frequency ultrasound application. J Pharm Pharmacol 2004 Sep; 56:1109-1118.

Cantrell JT, McArthur MJ, Pishko MV. Transdermal extraction of interstitial fluid by low-frequency ultrasound quantified with 3H2O as a tracer molecule. J Pharm Sci 2000 Sep; 89:1170-1179.

Chan AH, Fujimoto VY, Moore DE, Martin RW, Vaezy S. An image-guided high intensity focused ultrasound device for uterine fibroids treatment. Med Phys 2002 Nov; 29:2611-2620.

Congressionally Established Diabetes Research Working Group. 1999. Conquering Diabetes: A Strategic Plan for the 21th Century. NIH Publication No. 99-4398.

Dalecki D, Raeman CH, Child SZ, Carstensen EL. A test for cavitation as a mechanism for intestinal hemorrhage in mice exposed to a piezoelectric lithotripter. Ultrasound Med Biol 1996; 22:493-496.

Darrow H, Schulthies S, Draper D, Ricard M, Measom GJ. Serum Dexamethasone Levels After Decadron Phonophoresis. J Athl Train 1999 Oct; 34:338-341.

Dogan A, Uchino K, Newnham RE. Composite piezoelectric transducer with truncated conical endcaps "cymbal". IEEE Trans Ultrason , Ferroelect , Freq Contr 1997; 44:597-605.

Edmonds PD, Sancier KM. Evidence for free radical production by ultrasonic cavitation in biological media. Ultrasound Med Biol 1983; 9:635-639.

Fellinger K, Schmid J. Klinik an Therapie des Chronischen (transl. Clinical experience/practise about the therapy of the chronic (illness). Gelenkreumatismus (transl. Articular Rheumatism) 1954;549-552.

Flynn HG. Generation of transient cavities in liquids by microsecond pulses of ultrasound. J Acoust Soc Amer 1982; 72:1926-1932.

Fry WJ. Intense ultrasound; a new tool for neurological research. J Ment Sci 1954 Jan; 100:85-96.

Fry WJ, Mosberg W, Barnard JW, Fry FJ. Production of focal destructive lesions in the central nervous system with ultrasound. Journal of Neurosurgery 1954; 11:471-478.

Gelet A, Chapelon JY, Poissonnier L, Bouvier R, Rouviere O, Curiel L, Janier M, Vallancien G. Local recurrence of prostate cancer after external beam radiotherapy: early experience of salvage therapy using high-intensity focused ultrasonography. Urology 2004 Apr; 63:625-629.

Gignoux BM, Scoazec JY, Curiel L, Beziat C, Chapelon JY. [High intensity focused ultrasonic destruction of hepatic parenchyma]. Ann Chir 2003 Feb; 128:18-25.

Graff KF. A History of Ultrasonics. In: Mason WP, Thurston RN, eds. Physical Acoustics. New York: Academic Press. 1981.

Hamilton M, Blackstock D. Nonlinear acoustics. San Diego, CA: Academic Press. 1998.

Hippius M, Uhlemann C, Smolenski U, Schreiber U, Reissig S, Hoffmann A. In vitro investigations of drug release and penetration--enhancing effect of ultrasound on transmembrane transport of flufenamic acid. Int J Clin Pharmacol Ther 1998 Feb; 36:107-111.

Hsieh YL. Effects of ultrasound and diclofenac phonophoresis on inflammatory pain relief: suppression of inducible nitric oxide synthase in arthritic rats. Phys Ther 2006 Jan; 86:39-49.

Hynynen KH. The threshold for thermally significant cavitation in dog's thigh muscle *in vivo*. Ultrasound Med Biol 1990; 17:157--169.

Jenne JW, Divkovic G, Rastert R, Debus J, Huber PE. [Focused ultrasound surgery. Basics, current status, and new trends]. Radiologe 2003 Oct; 43:805-812.

Johnson ME, Mitragotri S, Patel A, Blankschtein D, Langer R. Synergistic effects of chemical enhancers and therapeutic ultrasound on transdermal drug delivery. J Pharm Sci 1996 Jul; 85:670-679.

Koeke PU, Parizotto NA, Carrinho PM, Salate AC. Comparative study of the efficacy of the topical application of hydrocortisone, therapeutic ultrasound and phonophoresis on the tissue repair process in rat tendons. Ultrasound Med Biol 2005 Mar; 31:345-350.

Kost J. Ultrasound-assisted insulin delivery and noninvasive glucose sensing. Diabetes Technol Ther 2002; 4:489-497.

Kost J, Mitragotri S, Gabbay RA, Pishko M, Langer R. Transdermal monitoring of glucose and other analytes using ultrasound. Nat Med 2000 Mar; 6:347-350.

Kost J, Pliquett U, Mitragotri S, Yamamoto A, Langer R, Weaver J. Synergistic effect of electric field and ultrasound on transdermal transport. Pharm Res 1996 Apr; 13:633-638.

Kozanoglu E, Basaran S, Guzel R, Guler-Uysal F. Short term efficacy of ibuprofen phonophoresis versus continuous ultrasound therapy in knee osteoarthritis. Swiss Med Wkly 2003 Jun 14; 133:333-338.

Kushner J, Blankschtein D, Langer R. Experimental demonstration of the existence of highly permeable localized transport regions in low-frequency sonophoresis. J Pharm Sci 2004 Nov; 93:2733-2745.

Lee S, Nayak V, Dodds J, Pishko M, Smith NB. Ultrasonic mediated glucose measurements *in vivo* using the cymbal array. Ultrasound Med Biol 2005; 31:971-977.

Lee S, Newnham RE, Smith NB. Short Ultrasound Exposure Times for Noninvasive Insulin Delivery in Rats using the Light Weight Cymbal Array. IEEE Transactions on Ultrasonics, Ferroelectrics and Frequency Control 2004a; 51:176-180.

Lee S, Snyder B, Newnham RE, Smith NB. Noninvasive ultrasonic transdermal insulin delivery in rabbits using the light-weight cymbal array. Diabetes Technol Ther 2004 Decb; 6:808-815.

Leighton T. Acoustic Bubble. San Diego, CA: Academic Press. 1994.

Levy D, Kost J, Meshulam Y, Langer R. Effect of ultrasound on transdermal drug delivery to rats and guinea pigs. J Clin Invest 1989 Jun; 83:2074-2078.

Lewin P, Ziskin M. Ultrasonic Exposimetry . Boca Raton, FL: CRC Press. 1992.

Lewin PA, Barrie-Smith N, Ide M, Hynynen K, Macdonald M. Interlaboratory acoustic power measurement. J Ultrasound Med 2003 Feb; 22:207-213.

Li CX, Xu GL, Jiang ZY, Li JJ, Luo GY, Shan HB, Zhang R, Li Y. Analysis of clinical effect of high-intensity focused ultrasound on liver cancer. World J Gastroenterol 2004 Aug 1; 10:2201-2204.

Madersbacher S, Marberger M. High-energy shockwaves and extracorporeal high-intensity focused ultrasound. J Endourol 2003 Oct; 17:667-672.

Mason TJ, Lorimer JP. Sonochemistry: Theory, Applications and Uses of Ultrasound in Chemistry. West Sussex, U.K.: Ellis Horwood Limited. 1988.

Merino G, Kalia YN, gado-Charro MB, Potts RO, Guy RH. Frequency and thermal effects on the enhancement of transdermal transport by sonophoresis. J Control Release 2003 Feb 14; 88:85-94.

Miller MW, Miller DL, Brayman AA. A review of in vitro bioeffects of intertial ultrasonic cavitation from a mechanistic perspective. Ultrasound Med Biol 1996;22:1131-1154.

Mitragotri S. Healing sound: the use of ultrasound in drug delivery and other therapeutic applications. Nat Rev Drug Discov 2005 Mar; 4:255-260.

Mitragotri S, Blankschtein D, Langer R. Ultrasound-mediated transdermal protein delivery. Science 1995a; 269:850-853.

Mitragotri S, Blankschtein D, Langer R. Transdermal drug delivery using low-frequency sonophoresis. Pharm Res 1996; 13:411-420.

Mitragotri S, Blankschtein D, Langer R. An explanation for the variation of the sonophoretic transdermal transport enhancement from drug to drug. J Pharm Sci 1997 Oct; 86:1190-1192.

Mitragotri S, Coleman M, Kost J, Langer R. Analysis of ultrasonically extracted interstitial fluid as a predictor of blood glucose levels. J Appl Physiol 2000 Sepa; 89:961-966.

Mitragotri S, Coleman M, Kost J, Langer R. Transdermal extraction of analytes using low-frequency ultrasound. Pharm Res 2000b; 17:466-470.

Mitragotri S, Edwards DA, Blankschtein D, Langer R. A mechanistic study of ultrasonically-enhanced transdermal drug delivery. J Pharm Sci 1995 Junb; 84:697-706.

Mitragotri S, Farrell J, Tang T, Terahara T, Kost J, Langer R. Determination of the threshold energy dose for ultrasound-induced transdermal drug transport. Journal of Controlled Release 2000c; 63:41-52.

Mitragotri S, Kost J. Low-frequency sonophoresis: a noninvasive method of drug delivery and diagnostics. Biotechnol Prog 2000; 16:488-492.

Mitragotri S, Kost J. Low-frequency sonophoresis: a review. Adv Drug Deliv Rev 2004 Mar 27; 56:589-601.

Miyazaki S, Mizuoka H, Kohata Y, Takada M. External control of drug release and penetration. VI. Enhancing effect of ultrasound on the transdermal absorption of

indomethacin from an ointment in rats. Chem Pharm Bull (Tokyo) 1992 Oct; 40:2826-2830.

Montorsi F, Salonia A, Guazzoni G, Barbieri L, Colombo R, Brausi M, Scattoni V, Rigatti P, Pizzini G. Transdermal electromotive multi-drug administration for Peyronie's disease: preliminary results. J Androl 2000 Jan; 21:85-90.

Morimoto Y, Mutoh M, Ueda H, Fang L, Hirayama K, Atobe M, Kobayashi D. Elucidation of the transport pathway in hairless rat skin enhanced by low-frequency sonophoresis based on the solute-water transport relationship and confocal microscopy. J Control Release 2005 Apr 18; 103:587-597.

Mutoh M, Ueda H, Nakamura Y, Hirayama K, Atobe M, Kobayashi D, Morimoto Y. Characterization of transdermal solute transport induced by low-frequency ultrasound in the hairless rat skin. J Control Release 2003 Sep 19; 92:137-146.

Nanda A, Nanda S, Ghilzai NM. Current developments using emerging transdermal technologies in physical enhancement methods. Curr Drug Deliv 2006 Jul; 3:233-242.

Newnham RE, Xu QC, Yoshikawa S, inventors. 1991 Mar 12. Transformed stress direction acoustic transducer. 4,999,819.

Newnham RE, Xu QC, Yoshikawa S, inventors. 1994 Jan 4. Metal-electroactive ceramic composite actuators. 5,276,657.

Paliwal S, Menon GK, Mitragotri S. Low-frequency sonophoresis: ultrastructural basis for stratum corneum permeability assessed using quantum dots. J Invest Dermatol 2006 May; 126:1095-1101.

Park SR, Jang KW, Park SH, Cho HS, Jin CZ, Choi MJ, Chung SI, Min BH. The effect of sonication on simulated osteoarthritis. Part I: effects of 1 MHz ultrasound on uptake of hyaluronan into the rabbit synovium. Ultrasound Med Biol 2005 Nov; 31:1551-1558.

Pitt WG, Husseini GA, Staples BJ. Ultrasonic drug delivery--a general review. Expert Opin Drug Deliv 2004 Nov; 1:37-56.

Prausnitz MR. Reversible skin permeabilization for transdermal delivery of macromolecules. Crit Rev Ther Drug Carrier Syst 1997; 14:455-483.

Prausnitz MR. A practical assessment of transdermal drug delivery by skin electroporation. Adv Drug Deliv Rev 1999; 35:61-76.

Rosim GC, Barbieri CH, Lancas FM, Mazzer N. Diclofenac phonophoresis in human volunteers. Ultrasound Med Biol 2005 Mar; 31:337-343.

Roy RA, Madanshetty SI, Apfel RE. An acoustic backscattering technique for the detection of cavitation produced by microsecond pulses of ultrasound. J Acoust Soc Amer 1990; 87:2451-2458.

Saleh KY, Smith NB. Two-dimensional ultrasound phased array design for tissue ablation for treatment of benign prostatic hyperplasia. Int J Hyperthermia 2004 Feb; 20:7-31.

Santoianni P, Nino M, Calabro G. Intradermal drug delivery by low-frequency sonophoresis (25 kHz). Dermatol Online J 2004; 10:24.

Schafer M, Kyaynak T, and Lewin P. Design of a minature in vivo shock wave hydrophone. *In* , 10 December 90 A.D.

Shung KK, Smith MB, Tsui B. Principles of medical imaging. San Diego: Academic Press. 1992.

Smith NB, Lee S, Maione E, Roy RB, McElligott S, Shung KK. Ultrasound mediated transdermal transport of insulin through in vitro human skin using novel transducer designs. Ultrasound Med Biol 2003; 29:311-317.

Stansfield D. Underwater electroacoustic transducers. Bath, UK: Bath University Press. 1990.

Sundaram J, Mellein BR, Mitragotri S. An experimental and theoretical analysis of ultrasound-induced permeabilization of cell membranes. Biophys J 2003 May; 84:3087-3101.

Tachibana K. Transdermal delivery of insulin to alloxan-diabetic rabbits by ultrasound exposure. Pharm Res 1992 Jul; 9:952-954.

Tachibana K, Tachibana S. Transdermal delivery of insulin by ultrasonic vibration. J Pharm Pharmacol 1991 Apr; 43:270-271.

Tachibana K, Tachibana S. The use of ultrasound for drug delivery. Echocardiography 2001 May; 18:323-328.

Tang H, Blankschtein D, Langer R. Effects of low-frequency ultrasound on the transdermal permeation of mannitol: comparative studies with in vivo and in vitro skin. J Pharm Sci 2002 Aug; 91:1776-1794.

Tang H, Mitragotri S, Blankschtein D, Langer R. Theoretical description of transdermal transport of hydrophilic permeants: application to low-frequency sonophoresis. J Pharm Sci 2001 May; 90:545-568.

Tempany CM, Stewart EA, McDannold N, Quade BJ, Jolesz FA, Hynynen K. MR imaging-guided focused ultrasound surgery of uterine leiomyomas: a feasibility study. Radiology 2003 Mar; 226:897-905.

ter Haar G. Review: Therapeutic ultrasound. European Journal of Ultrasound 1999;9:3-9.

Terahara T, Mitragotri S, Kost J, Langer R. Dependence of low-frequency sonophoresis on ultrasound parameters; distance of the horn and intensity. Int J Pharm 2002 Mar 20; 235:35-42.

Tezel A, Mitragotri S. Interactions of inertial cavitation bubbles with stratum corneum lipid bilayers during low-frequency sonophoresis. Biophys J 2003 Dec; 85:3502-3512.

Tezel A, Paliwal S, Shen Z, Mitragotri S. Low-frequency ultrasound as a transcutaneous immunization adjuvant. Vaccine 2005 May 31; 23:3800-3807.

Tezel A, Sens A, Mitragotri S. Description of transdermal transport of hydrophilic solutes during low-frequency sonophoresis based on a modified porous pathway model. J Pharm Sci 2003 Feb; 92:381-393.

Tezel A, Sens A, Tuchscherer J, Mitragotri S. Frequency dependence of sonophoresis. Pharm Res 2001 Dec; 18:1694-1700.

The Whitaker Foundation. Biomedical Engineering and the Fight Against Diabetes, 2003 Annual Report. Arlington, VA: The Whitaker Foundation. 2004.

Tiwari SB, Pai RM, Udupa N. Influence of ultrasound on the percutaneous absorption of ketorolac tromethamine in vitro across rat skin. Drug Deliv 2004 Jan; 11:47-51.

Tressler JF, Cao W, Uchino K, Newnham RE. Finite element analysis of the cymbal-type flextensional transducer. IEEE Trans Ultrason , Ferroelect , Freq Contr 1998; 45:1363-1369.

varez-Roman R, Merino G, Kalia YN, Naik A, Guy RH. Skin permeability enhancement by low frequency sonophoresis: lipid extraction and transport pathways. J Pharm Sci 2003 Jun; 92:1138-1146.

Wang GM, Yang YF, Sun LA, Xu ZB, Xu YQ. [An experimental study on high intensity focused ultrasound combined with mitomycin treatment of bladder tumor]. Zhonghua Wai Ke Za Zhi 2003 Dec; 41:897-900.

Wang Y, Thakur R, Fan Q, Michniak B. Transdermal iontophoresis: combination strategies to improve transdermal iontophoretic drug delivery. Eur J Pharm Biopharm 2005 Jul; 60:179-191.

Weimann LJ, Wu J. Transdermal delivery of poly-l-lysine by sonomacroporation. Ultrasound Med Biol 2002 Sep; 28:1173-1180.

Wilson OB. An introduction to the theory and design of sonar transducers. Los Altos, CA: Peninsula Publishing. 1988.

Wood RW, Loomis AL. The physical and biological effects of high frequency sound waves with great intensity. Phil Mag 1927;4:417-436.

Wu F, Wang ZB, Chen WZ, Wang W, Gui Y, Zhang M, Zheng G, Zhou Y, Xu G, Li M, and others. Extracorporeal high intensity focused ultrasound ablation in the treatment of 1038 patients with solid carcinomas in China: an overview. Ultrason Sonochem 2004 May; 11:149-154.

Wu J, Chappelow J, Yang J, Weimann L. Defects generated in human stratum corneum specimens by ultrasound. Ultrasound Med Biol 1998 Jun; 24:705-710.

Yamashita N, Tachibana K, Ogawa K, Tsujita N, Tomita A. Scanning electron microscopic evaluation of the skin surface after ultrasound exposure. Anat Rec 1997 Apr; 247:455-461.

Yang JH, Kim DK, Yun MY, Kim TY, Shin SC. Transdermal delivery system of triamcinolone acetonide from a gel using phonophoresis. Arch Pharm Res 2006 May; 29:412-417.

Zhang I, Shung KK, Edwards DA. Hydrogels with enhanced mass transfer for transdermal drug delivery. J Pharm Sci 1996 Dec; 85:1312-1316.